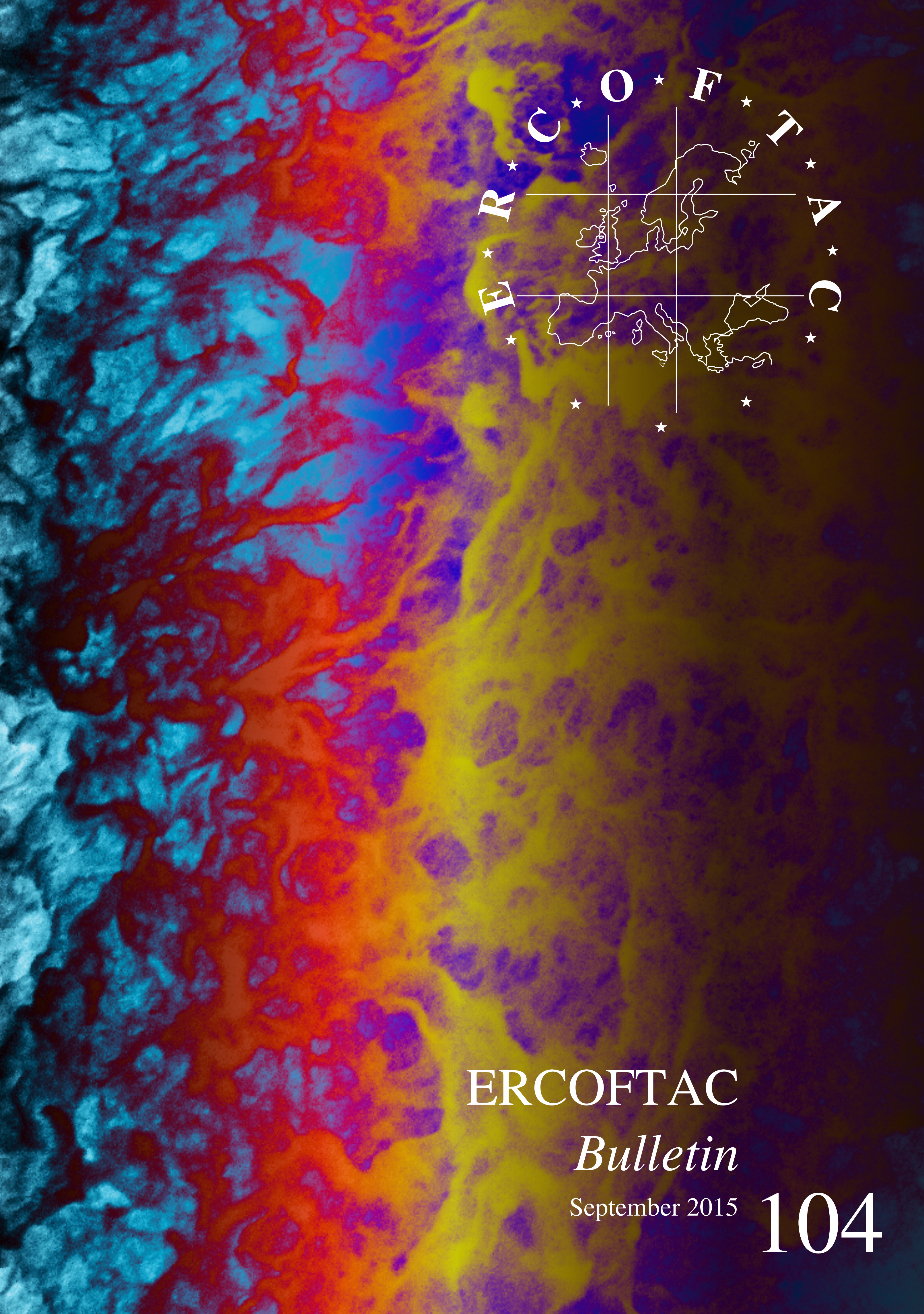

ERCOFTAC

Bulletin

September 2015

104

European Research Community on Flow, Turbulence and Combustion

ERCOFTAC is a leading European association of research, education and industry groups in the technology of flow, turbulence and combustion. The main objectives of *ERCOFTAC* are: To promote joint efforts of European research institutes and industries with the aim of **exchanging technical and scientific information**; to promote **Pilot Centres** for collaboration, stimulation and application of research across Europe; to stimulate, through the creation of **Special Interest Groups**, wellcoordinated European-wide research efforts on specific topics; to stimulate the creation of advanced training activities; and to be influential on funding agencies, governments, the European Commission and the European Parliament.

www.ercoftac.org

ERCOFTAC Bulletin 104, September 2015

TABLE OF CONTENTS

SUBMISSIONS

ERCOFTAC Bulletin
Institute of Thermal Machinery
Częstochowa University of Technology
Al. Armii Krajowej 21
42-201 Częstochowa
Poland
Tel: +48 343 250 507
Fax: +48 343 250 507
Email: ercoftac@imc.pcz.czest.pl

HOSTED, PRINTED & DISTRIBUTED BY

CZĘSTOCHOWA UNIVERSITY OF TECHNOLOGY

NEXT *ERCOFTAC* EVENTS

ERCOFTAC Autumn Festival
October 15th 2015
Vinci, Firenze, Italy

ERCOFTAC Committee Meetings
October 16th 2015
Vinci, Firenze, Italy

The ERCOFTAC Best Practice Guidelines for Industrial Computational Fluid Dynamics

The Best Practice Guidelines (BPG) were commissioned by ERCOFTAC following an extensive consultation with European industry which revealed an urgent demand for such a document. The first edition was completed in January 2000 and constitutes generic advice on how to carry out quality CFD calculations. The BPG therefore address mesh design; construction of numerical boundary conditions where problem data is uncertain; mesh and model sensitivity checks; distinction between numerical and turbulence model inadequacy; preliminary information regarding the limitations of turbulence models etc. The aim is to encourage a common best practice by virtue of which separate analyses of the same problem, using the same model physics, should produce consistent results. Input and advice was sought from a wide cross-section of CFD specialists, eminent academics, end-users and, (particularly important) the leading commercial code vendors established in Europe. Thus, the final document can be considered to represent the consensus view of the European CFD community.

Inevitably, the Guidelines cannot cover every aspect of CFD in detail. They are intended to offer roughly those 20% of the most important general rules of advice that cover roughly 80% of the problems likely to be encountered. As such, they constitute essential information for the novice user and provide a basis for quality management and regulation of safety submissions which rely on CFD. Experience has also shown that they can often provide useful advice for the more experienced user. The technical content is limited to single-phase, compressible and incompressible, steady and unsteady, turbulent and laminar flow with and without heat transfer. Versions which are customised to other aspects of CFD (the remaining 20% of problems) are planned for the future.

The seven principle chapters of the document address numerical, convergence and round-off errors; turbulence modelling; application uncertainties; user errors; code errors; validation and sensitivity tests for CFD models and finally examples of the BPG applied in practice. In the first six of these, each of the different sources of error and uncertainty are examined and discussed, including references to important books, articles and reviews. Following the discussion sections, short simple bullet-point statements of advice are listed which provide clear guidance and are easily understandable without elaborate mathematics. As an illustrative example, an extract dealing with the use of turbulent wall functions is given below:

- Check that the correct form of the wall function is being used to take into account the wall roughness. An equivalent roughness height and a modified multiplier in the law of the wall must be used.
- Check the upper limit on $y+$. In the case of moderate Reynolds number, where the boundary layer only extends to $y+$ of 300 to 500, there is no chance of accurately resolving the boundary layer if the first integration point is placed at a location with the value of $y+$ of 100.
- Check the lower limit of $y+$. In the commonly used applications of wall functions, the meshing should be arranged so that the values of $y+$ at all the wall-adjacent integration points is only slightly above the recommended lower limit given by the code developers, typically between 20 and 30 (the form usually assumed for the wall functions is not valid much below these values). This procedure offers the best chances to resolve the turbulent portion of the boundary layer. It should be noted that this criterion is impossible to satisfy close to separation or reattachment zones unless $y+$ is based upon $y*$.
- Exercise care when calculating the flow using different schemes or different codes with wall functions on the same mesh. Cell centred schemes have their integration points at different locations in a mesh cell than cell vertex schemes. Thus the $y+$ value associated with a wall-adjacent cell differs according to which scheme is being used on the mesh.
- Check the resolution of the boundary layer. If boundary layer effects are important, it is recommended that the resolution of the boundary layer is checked after the computation. This can be achieved by a plot of the ratio between the turbulent to the molecular viscosity, which is high inside the boundary layer. Adequate boundary layer resolution requires at least 8-10 points in the layer.

All such statements of advice are gathered together at the end of the document to provide a 'Best Practice Checklist'. The examples chapter provides detailed expositions of eight test cases each one calculated by a code vendor (viz FLUENT, AEA Technology, Computational Dynamics, NUMECA) or code developer (viz Electricité de France, CEA, British Energy) and each of which highlights one or more specific points of advice arising in the BPG. These test cases range from natural convection in a cavity through to flow in a low speed centrifugal compressor and in an internal combustion engine valve.

Copies of the Best Practice Guidelines can be acquired from:

ERCOFTAC (CADO)
PO Box 53877
London, SE27 7BR
United Kingdom
Tel: +44 203 602 8984
Email: magdalena.jakubczak@ercoftac.org

The price per copy (not including postage) is:

ERCOFTAC members	
First copy	*Free*
Subsequent copies	75 Euros
Students	75 Euros
Non-ERCOFTAC academics	140 Euros
Non-ERCOFTAC industrial	230 Euros
EU/Non EU postage fee	10/17 Euros

Introduction to Special Theme: Multiphase Flow

O. M. H. Rodriguez
PC-Brazil Coordinator

The main goal of this ERCOFTAC Bulletin Theme Issue is to deliver a brief overview of some research activities in development in Brazil on Multiphase Flow and Fluid Mechanics. One of the contributions reports an experimental work on pipe flow of mixtures of heavy oil and water, flow pattern characterization, flow patterns maps and interfacial wave properties of wavy stratified flow, a flow pattern observed in directional wells in the offshore production scenario. Other paper deals with the linear and weakly nonlinear stability analysis of sand ripples in liquids. Curves of marginal stability predicted by the linear analysis are compared with data and the theory is also applied to pressure-driven gas-liquid stratified flow. A work describes recent developments of optical measurement methods in fluid mechanics, including applications in two-phase flows (LIF for annular flow, bubble characterization and liquid velocity in intermittent flow), 3-D velocity measurements (digital holographic and tomographic PIV for flow measurements) and cardiovascular flow measurements. In another experimental work a study of the transient behavior of drag reduction by polymer additives in pipe flow is presented, a problem that also interests the upstream oil industry. The process of energy dissipation due to the coil-stretching of a polymer in a region near the wall explains the drag increase at the very start of the tests and the maximum drag reduction possible is shown to be a function of polymer concentration, molecular weight and molecule conformation. The last three papers are devoted to fluid mechanics. In one of them the phenomena of the flow around cylinders, a classical problem that has direct influence in project development of shell and tube heat exchangers, particularly as regards the behavior of vortex shedding and fluid-structure interaction, is experimentally investigated. Interesting correlations for the prediction of the Strouhal number as a function of the blockage ratio are proposed. In other paper the authors go further and study of the wake behind groups of cylinders in an aerodynamic channel with considerations on the effect of blockage ratio on the phenomenon of bistability on two or more cylinders. Interesting flow visualizations of the phenomenon are accomplished in a water channel. Finally, a contribution on tensorial decompositions to explore limitations of RANS modeling due to the Boussinesq approximation. The authors argue that a non-persistence-of-straining tensor orthogonal to the mean-rate-of-strain tensor is able to explore tensorial subspaces not reached by the mean-rate-of-strain tensor. Two benchmarks are employed (DNS - square duct and LES - Backward Facing Step) in order to evaluate the proposed approach.

As a final remark, I would like to register that a sign that Brazil has a flourishing multiphase-Flow community is the organization in March of this year of the 3^{rd} Brazilian Multiphase-Flow Journeys (JEM 2015) and 4^{th} Brazilian Meeting on Boiling, Condensation and Multiphase Flow (EBECEM 2015), events that congregated more than 100 participants.

Viscous Oil-Water Pipe Flows: Flow Patterns, Pressure Gradient and Interfacial Wave Properties

M.S. de Castro
Faculty of Mechanical Engineering,
University of Campinas, Campinas, Brazil
mcastro@fem.unicamp.br

Abstract

Despite recent discoveries of light oil in the Brazil's presalt layer, about 25% of its' reserves will still consist of viscous oil. It is known that the commercial codes used for light oil are not suitable for viscous oils presenting a large discrepancy between the experimental data and predictions. In this work, experimental data on flow pattern characterization and pressure gradient in horizontal viscous oil-water flows and a compilation of previous works from the author and coworkers on properties of the interfacial wave of the wavy stratified flow pattern, both experimental data acquired at the experimental facility of the LETeF (Thermal and Fluids Engineering Laboratory) of the Engineering School of Sao Carlos of the University of Sao Paulo in Brazil, are presented. The experimental data are being used to improve the two-phase flows models, e.g. the one dimensional two-fluid model.

1 Introduction

Liquid-liquid flows are present in a wide range of industrial processes; however, studies on such flows are not as common as those on gas-liquid flows. The interest in liquid-liquid flows has recently increased mainly due to the petroleum industry, where oil and water are often transported together for long distances.

Pressure drop, heat transfer, corrosions and structural vibration are a few examples of topics that depend on the geometrical configuration or flow patterns of the immiscible phases. An experimental work on liquid-liquid flows where a flow loop was presented and visual classification of the flow patterns was done can be seen in the article of Trallero, Sarica and Brill [1]. In that paper data for horizontal flow were presented including characterization of stratified and semi-stratified flows, dispersions and emulsions for oils of low viscosity, however, the authors did not differ the wavy stratified flow from stratified with mixture at the interface. A more detailed oil-water horizontal flow pattern classification, dividing the observed flow patterns of Trallero, Sarica and Brill [1] into several sub-patterns was given by Elseth [2]. Elseth [2] presented a more detailed oil-water horizontal flow pattern classification, dividing Trallero's patterns into several sub-patterns. That author observed the liquid- liquid wavy stratified flow pattern. The work of Trallero, Sarica and Brill [1] was continued by Alkaya, Jayawarderna and Brill [3], but now introducing the effects of pipe inclination and the wavy stratified flow pattern was reported. All the quoted authors have dealt with relatively low viscosity oils. On the other hand, Bannwart et al. [4] studied a very viscous oil-water flow and reported the stratified, core annular, oil-plug flow and flow of drops of oil in water flow patterns. Interfacial waves were spotted, but details on wave's geometrical properties were not given.The oil-plug flow was also observed by Oddie et al. [5]. Oil-water flow maps are not as common as those of gas-liquid flows, and the transition boundaries have a stronger dependence on the oil viscosity. Examples of oil-water flow maps can be seen in Bannwart et al. [4], Trallero [6] and Rodriguez and Oliemans [7].

The stratified flow pattern is present in directional oil wells and pipelines and is characterized by the heavier and lighter phases at the bottom and top part of the pipe, respectively, divided by an interface. The interface in stratified flow can be smooth or wavy. The wavy structure was studied in gas-liquid flow by Bontozoglou and Hanratty [8] and Bontozoglou [9]. One of the findings is that the two-phase friction factor of wavy stratified flow can be about fifty times as high as the friction factor of smooth stratified flow. Li, Guo and Chen [10] studied the gas-liquid stratified flow pattern and showed that the interfacial waves have significant influence on heat transfer and pressure drop.

Although it seems clear that interfacial wave properties are important for the complete understanding of wavy stratified flow, that information is quite scanty. Some data are presented in the paper of Al-Wahaibi and Angeli [11], but it lacks in details. Barral and Angeli [12] using a double-wire probe presented some data on the interface characteristics of the liquid-liquid stratified flow, but they used a low viscous oil and they were, mostly, interested in the transition from this flow pattern to the dual continuous flows. More detailed data of the interfacial wave of the stratified flow were present by Rodriguez and Baldani [13] which used experimental data on the interfacial wave properties to improve the one-dimensional two-fluid model for predicting holdup and pressure drop. Rodriguez and Castro [14] used the idea of an average wave number and wave velocity to include the interfacial-tension force terms in the prediction of the transition boundary of the stratified flow pattern; they find good agreement with data from literature. Castro and Rodriguez [15] using viscous oil and water as working fluids and a high speed camera presented the interfacial wave properties such as aspect ratio and velocity as functions of dimensionless parameters of the flow, they also presented the mean wave shape for many cases of viscous oil-water stratified flow pattern.

The goal of this work is to present the observed viscous oil-water flow patterns and some data on interfacial wave properties of the wavy stratified flow pattern. In Sections 2 the experimental setup and procedure are presented. In section 3 the observed flow patterns and a graph of the pressure drop are presented. The compilation of previous works of the author on interfacial wave properties is presented in Section 4. Finally, the conclusions are drawn in section 5.

2 Experimental Setup and Procedure

2.1 Experimental Facility

The hydrophilic-oilphobic glass test line of $26mm$ i.d. and $12m$ length of the multiphase flow loop of the Thermal-Fluids Engineering Laboratory, Sao Carlos School of Engineering, University of Sao Paulo, was used to produce different oil-water flow patterns. A by-pass line allows the quick-closing-valves technique to measure in-situ volumetric fraction of water and oil. Water and oil were kept in polyethylene tanks. Positive displacement pumps, both remotely controlled by their respective variable-frequency drivers, pump the phases to the multiphase test line. Before entering the multiphase test line the phases are mixed in the multiphase mixer. Positive displacement and vortex flow meters were used to measure the volumetric flow of each fluid and, consequently, the superficial velocities. A thermocouple measures the temperature of the oil before it enters the test line. After the test line the fluids entered a liquid-gas separator tank, after this, the mixture of water and oil enters, by gravity, the coalescent-plates liquid-liquid separator. Finally, water and oil return by gravity to their tanks.

The test section has seven transparent boxes used to film the flow, in order to correct any remaining distortion of light due to lens and parallax effects, the boxes were filled with water.

The first box is placed at $1.3m$ from the beginning of the test line; the others are placed $1.5m$ apart of each other. The fluids used were tap water and an oil with density of $854kg/m^3$ and viscosity of $329mPa.s$ at $20°C$. The viscosity was measured with a rheometer $Brokfield^{TM}$ model $LVDV-III+$ with rotor $SC4-18$. The oil-water interfacial tension was of $0.045N/m$. The oil-water contact angle with the borosilicate glass was 29° (hydrophilic-oilphobic). The interfacial tension and contact angle were measured with an optical tensiometer of KSV^{TM} model CAM 200. The test line has eight pressure taps used to measure pressure drop. The first pressure tap is placed at the entrance of the section, and the others $1.5m$ apart each other. A schematic view of the flow loop is presented in Fig. 1. Details related to the holdup measurement technique and flow loop can be seen in Rodriguez et al. [16].

2.2 Experimental Procedure

The flow was filmed using a high speed video camera (i-SPEED 3 OLYMPUS^{TM}) to acquire flow-pattern data. The camera was installed on a pedestal and two xenon lamps were used to illuminate the flow. After reaching steady state the flow was recorded at various frame rates, depending on the flow pattern. Stratified, stratified with mixture at the interface were filmed at 100 frames/second, drops and core-annular flow at 200

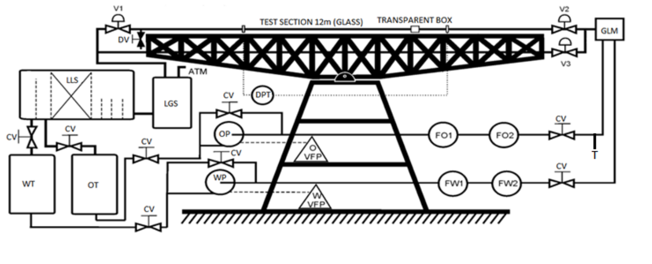

Figure 1: Schematic view of the inclinable multiphase flow loop used in this work (Rodriguez and Baldani [13])

frames/second and dispersion of oil in water at 1000 frames/second. The transparent box used was at 5.8 m from the inlet of the test section. Data on pressure drop were acquired via a LabView^{TM} based program at a rate of 5 kHz. The pressure taps were placed at 3 m apart of each other, for oil superficial velocities up to 0.28 m/s and at 1.5 m from each other for higher oil superficial velocities. The experiments on the spatial transition of the stratified flow were done filming the flow at different points of the test section. Castro and Rodriguez [15] presented the experimental procedure for the same experimental facility to acquire data on the interfacial wave properties. Movies of the flow were taken at 100 frames/second at the transparent box installed at 4.3m from the entrance. Then, on a homemade LabVIEW-based program the frames were binarized, the waves on the interface are recognized and the amplitude and wavelength are measured. The wave velocity is measured via cross-correlation between the frames.

3 Flow Patterns

Data on flow patterns in horizontal heavy oil-water flow were acquired. Seven different flow patterns were seen, and the classification is based on the work of literature [3] and [4]. This classification is based on visual observation and pressure drop data. The observed flow patterns are: smooth stratified (ST); wavy stratified (SW); stratified with mixture at the interface (SW&MI); drops of oil (G) (two sub patterns were placed together in this classification: diluted and dense stratified drops); oil plug flow (P); dispersion of oil in water and water layer (Do/w&w); and core-annular flow pattern (A). The superficial velocity (Uws) of water varied from 0.02 m/s to 3 m/s and the oil superficial velocity (Uos) varied from 0.02 to 1 m/s in these experiments.

3.1 Flow Patterns - Example of Visual Observation

By visual observation the flow patterns can be divided into the seven flow patterns presented. Each flow pattern has its own characteristics; here for example an image of the wavy stratified flow pattern is shown (Fig. 2). The characteristics of this flow pattern is oil and water flowing as separated layers with a wavy interface between them where waves are visible and no dispersion at the interface is observed.

3.2 Flow Patterns - Pressure Gradient

With the change of flow pattern several variations were observed in pressure gradient data; this was used to confirm the classification given by the visual observation.

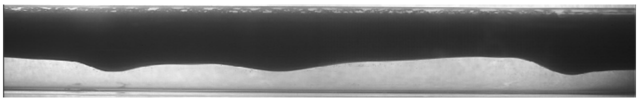

Figure 2: Wavy stratified flow (SW) ($Uws = 0.1m/s, Uos = 0.04m/s$)

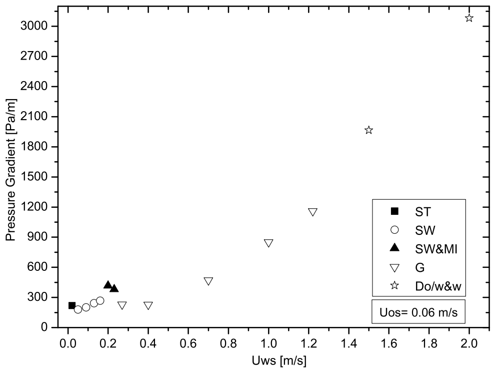

Figure 3: Experimental pressure drop variation for low oil superficial velocities ($0.02m/s \leq Uos \leq 0.08m/s$)

The graph of Fig. 3 present the pressure gradient variation as the water superficial velocity increases for constant oil superficial velocities, accordingly to Rodriguez and Oliemans [7], Rodriguez and Baldani [13] and Mandhane, Gregory and Aziz [17].

For low oil superficial velocities ($0.02m/s \leq Uos \leq 0.08m/s$), three distinct trends are observed as the surface velocity of the water increases. Initially the pressure gradient increases with increasing the water superficial velocity up to a local maximum, then it decreases and finally increases again. These changes in the pressure gradient trend are due to the change in the flow pattern. Thus, in Fig. 3, initially stratified patterns are observed (ST, SW) until Uws = 0.2 m/s then the SW & MI flow pattern is observed, and there is the transition to the drops flow pattern (G) and finally dispersion of oil in water flow pattern (Do / w & w). The core-annular flow pattern (A) is not present.

In the other regions the same differences in trends are observed as the flow pattern changes, it is the case of Fig.4. Figure 4 shows the variation of the pressure gradient with water superficial velocity for high oil superficial velocities (0.7 to 1 m/s). In this region two different trends are observed in the pressure gradient, with increasing the water superficial velocity. One related to the core-annular flow (A) with water superficial velocities between 0.2 and 1.5 m/s, and other to the dispersion of oil in water with water flow pattern (Do/w&w). The change in the derivative of the pressure gradient values is related to the flow pattern change from core-annular flow (A) to dispersed flow (Do/w&w).

3.3 Flow Maps

The experimental flow pattern map obtained in this work for heavy oil-water flow is presented in Fig. 5; it was made by visual observation and confirmed by the pressure gradient method. A flow pattern map predicted by the model of Trallero [6] can be seen in Fig. 6 for comparison purposes, using the same pipe diameter, pipe inclination, and fluids properties of this work (figure 5).

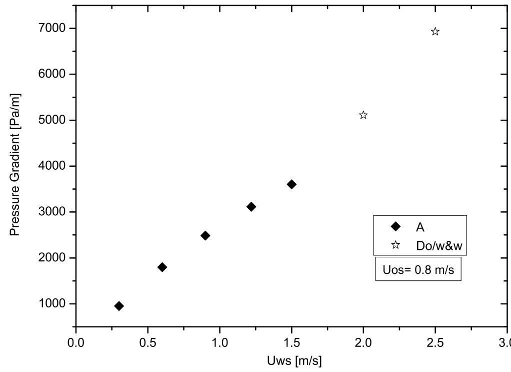

Figure 4: Experimental pressure drop variation for high oil superficial velocities ($Uos = 0,8m/s$)

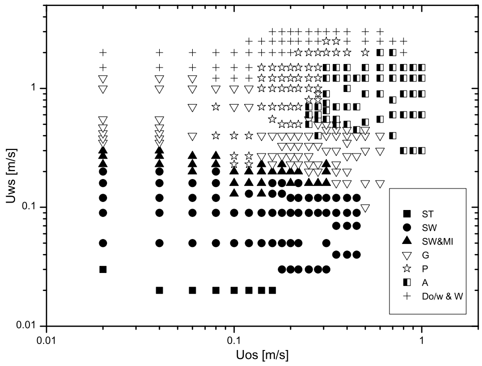

Figure 5: Experimental flow pattern map from visual observation and pressure gradient variation

The symbols used in both flow maps are the same for the same flow patterns, to facilitate the comparison.

The flow maps are, essentially, in complete disagreement (Figs. 5 and 6). It should be pointed out that Trallero [6] used light oil-water flow data to adjust his model. The region where stratified flow should occur is much smaller than the one observed in the experiments. The model does not predict the existence of core-annular flow, drops and oil-plug flow. On the other hand, it predicts emulsion of oil in water and emulsion of water in oil in regions where core-annular flow was experimentally observed. The authors believe that in light oil-water flow it is relatively easy for the turbulent dominant phase to break the continuous phase attached to the top pipe wall into drops; this phenomenon is quite harder to occur in heavy oil-water flow due to the oil viscosity, and so on the maintenance of a laminar flow of the oil phase for a wider range of superficial velocities.

4 Interfacial Wave Properties

In this section a compilation of previous works from the author and coworkers on properties of the interfacial wave of the wavy stratified flow pattern, both experimental data acquired at the experimental facility of the LETeF (Thermal and Fluids Engineering Laboratory) of the Engineering School of Sao Carlos of the University of Sao Paulo in Brazil, are presented. Firstly, Castro et

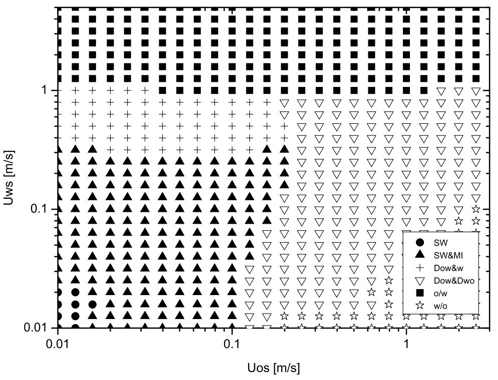

Figure 6: Flow pattern map predicted by Trallero's model [6]

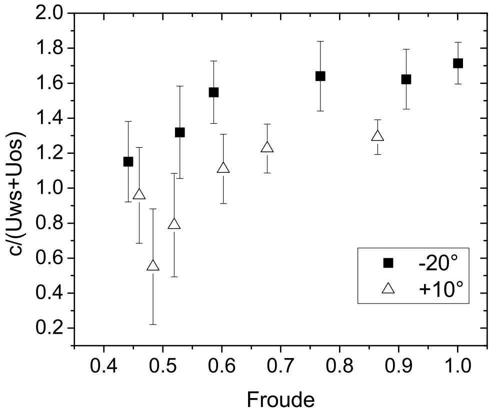

Figure 8: Normalized wave celerity as a function of the Froude number (Castro et al. [18])

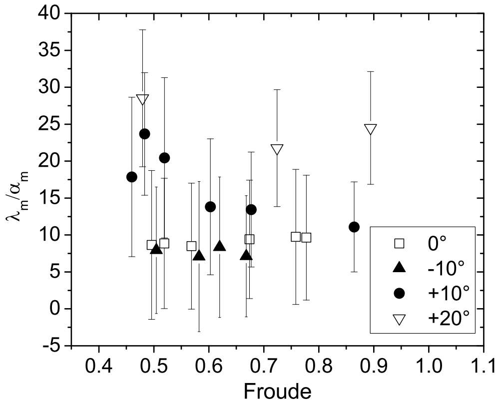

Figure 7: Interfacial wave aspect ratio as a function of Froude number (Castro et al. [18])

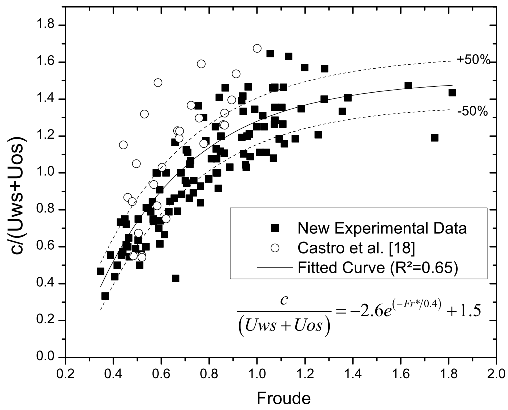

Figure 9: Wave aspect ratio as a function of Weber number (Castro and Rodriguez, [15])

al. [18] present the first data in the literature for interfacial wave properties for viscous oil-water wavy stratified flow pattern. The aspect ratio (ratio between the wavelength (λ_m) and wave amplitude (α_m)) and the wave celerity (c) normalized by the mixture velocity were presented as a function of a modified two-phase Froude number (Eq. 1):

$$Froude = \frac{V_w - V_o}{\sqrt{g(cos\Theta)y_{car}}} \tag{1}$$

where $V_w - V_o$ is the relative velocity, Θ is the inclination angle from horizontal, ϵ_w the water in-situ volumetric fraction, g the gravitational acceleration and y_{car} is a characteristic length defined by the water holdup times the pipe's internal diameter divided by four. One can see in Figures 7 and 8 present, respectively, the wave aspect ratio and normalized wave velocity both properties as a function of the modified Froude number. Recently, Castro and Rodriguez [18] presented new experimental data on the interfacial wave of the same flow of Castro et al. [18], and compared the data with others from literature (Castro et al. [18], and Barral and Angeli, [12]). The authors proposed that the wave aspect ratio is better correlated by a modified Webber number (Eq. 2):

$$Weber = \frac{\Delta\rho(V_w - V_o)^2 y_{car}}{\sigma} \tag{2}$$

where σ is the interfacial tension, $\Delta zrho$ is the difference between densities and y_{car} is the same of Eq. (1).

In figure 9 the wave aspect ratio is presented as a function of the modified Weber number, and a correlation is proposed for the experimental data, presented inside the figure.

The experimental data of the interfacial wave velocity is better correlated by the modified Froude number as presented in Castro et al. [18], and another correlation was found for the normalized wave velocity with the Froude number (Fig. 10).

5 Conclusions

Although there is increasing interest in liquid-liquid flows due to the oil industry, works on viscous oil are still scanty. So, a classification of flow patterns for this kind of flow is still not well defined, and even there is no definition of flow patterns that would be observed. This work propose that in the observed region of viscous oil flows there are seven different flow patterns, which are: smooth stratified, wavy stratified, stratified with mixture at the interface, drops, oil plug flow, core-annular flow and dispersion of oil in water. Each observed flow pattern had their different characteristics analysed throughout the text. It was shown that the change or transition

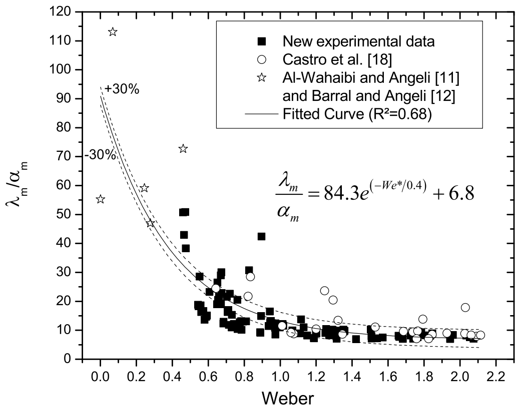

Figure 10: Normalized wave speed as a function of the Froude number (Castro and Rodriguez, [15])

between flow patterns is responsible for changes in the behaviour of the trends observed in the pressure gradient. Also, it was presented that the models used for predicting flow maps for light oil-water flows are not suitable for viscous oil-water flows.

Finally, a compilation of works on the properties of the interfacial wave of the viscous oil-water wavy stratified flow pattern is presented. Two articles were analysed, Castro et al. [18], the first work to present such wave properties, and Castro and Rodriguez [15], which offers new correlations for the wave aspect ratio and normalized wave velocity as a function of modified Weber and Froude numbers, respectively.

References

[1] Trallero, J.L.; Sarica, C. and Brill, J.P., A study of oil/water flow patterns in horizontal pipes, SPE Production and Facilities, Vol. 12, n. 3, pp. 165-172, 1997.

[2] Elseth, G., An experimental study of oil-water flow in horizontal pipes, Ph.D thesis. Porsgrunn: Norwegian University of Science and Technology, 270p, 2001.

[3] Alkaya, B.; Jayawarderna, S.S. and Brill, J.P., Oil-water flow patterns in slightly inclined pipes, Energy for the New Millenium, Vol. 14, n. 17, pp. 1-8, 2000.

[4] Bannwart, A. C.; Rodriguez, O. M. H.; De Carvalho, C. H. M.; Wang I. S.; Obregon Vara, R. M., Flow Patterns in Heavy Crude Oil-water Flow, Journal of Energy Resources Technology-Transactions of the ASME, Vol. 126, pp. 184-189, 2004.

[5] Oddie, G; Shi, H.; Durlofsky, L.J.; Aziz, K.; Pfeffer, B. and Holmes, J.A., Experimental study of two and three phase flows in large diameter inclined pipes, International Journal Multiphase Flow, Vol. 29, n. 4, pp. 527-558, 2003.

[6] Trallero, J. L., Oil-Water Flow Patterns in Horizontal Pipes, PhD thesis, The University of Tulsa, Tulsa, Oklahoma, USA, 1995

[7] Rodriguez, O.M.H. and Oliemans, R.V.A, Experimental study on oil-water flow in horizontal and slightly inclined pipes, International Journal Multiphase Flow, Vol. 32, n. 3, pp.323-343, 2006.

[8] Bontozoglou, V. and Hanratty, T.J., Wave height estimation in stratified gas-liquid flows. AiChe Journal, Vol. 35, n. 8, pp.1346-1350, 1989.

[9] Bontozoglou, V. Weakly nonlinear kelvin-helmholtz waves between fluids of finite depth. International Journal of Multiphase Flow, Vol. 17, n. 4, pp.509-518, 1991.

[10] Li, G.J., Guo, L., Chen, X.J. An experimental investigation on the interfacial waves in air-water two-phase flow within horizontal pipelines. Chinese Journal of Chemical Engineering, Vol. 5, n. 4, pp.316-324, 1997.

[11] Al-Wahaibi, T. and Angeli, P. Experimental study on interfacial waves in stratified horizontal oil-water flow. International Journal of Multiphase Flow, Vol. 37, n. 8, pp.930-940, 2011.

[12] Barral, A.H. and Angeli, P. Interfacial characteristics of stratified liquid-liquid flows using a conductance probe, Experiments in Fluids, Vol. 54, n. 1604, 2013.

[13] Rodriguez, O.M.H. and Baldani, L.S., Prediction of pressure gradiente and holdup in wavy stratified liquid-liquid inclined pipe flow, Journal of Petroleum Science and Engineering, Vol. 96-97, pp.140-151, 2012.

[14] Rodriguez, O.M.H. and Castro, M.S. Interfacial-tension-force model for the wavy-stratified liquid-liquid flow pattern transition, International Journal of Multiphase Flow, Vol. 58, pp. 114-126, 2014

[15] Castro, M.S. and Rodriguez, O.M.H., Interfacial waves in stratified viscous oil-water flow, Experimental Thermal and Fluid Science, Vol. 62, pp. 85-92, 2015.

[16] Rodriguez, I.H.; Yamaguti, H.K.B.; Castro, M.S.; Da Silva, M.J. and Rodriguez, O.M.H., Slip ratio in dispersed viscous oil-water pipe flow, Experimental Thermal and Fluid Science, Vol. 35, n. 1, pp. 11-19, 2011.

[17] Mandhane, J.M., Gregory, G.A. and Aziz, K., A flow pattern map for gas-liquid flow in horizontal pipes, International Journal of Multiphase Flow, Vol. 1, pp.537-553, 1974

[18] Castro, M.S., Pereira, C.C., Santos, J.N. and Rodriguez, O.M.H. Geometrical and kinematic properties of interfacial waves in stratified oil water flow in inclined pipe, Experimental Thermal and Fluid Science, Vol. 37, pp. 171-178, 2012.

Sand Ripples in Liquids

E. de M. Franklin

University of Campinas - UNICAMP, Campinas, Brazil

1 Introduction

A granular bed entrained as bed load may induce the formation of ripples and dunes [1]. Ripples are bedforms whose wavelengths scale with the grain diameter but not with the flow depth [2, 3] and are usually considered to be a result of initially two-dimensional bedforms that saturate eventually [4, 5]. On the contrary, dunes are bedforms whose wavelengths scale with both the flow field and the flow depth [2, 3] and may be considered as the result of coalescence of ripples [6, 7, 8, 9]. Ripples and dunes increase friction between the bed and fluid and are related to flooding, high pressure drops, and transients. The present article is a compilation of the referred papers [4], [5], [9], [10], [11].

2 Linear Analysis

Many linear stability analyses have been conducted in the past decades on the stability of granular beds sheared by fluids. Although this approach has been criticized in the case of aquatic dunes [8, 9], it is justified in the case of aquatic ripples given the small aspect ratio of the initial bedforms from which ripples are formed.

Franklin [4] presented a linear stability analysis of a granular bed sheared by a turbulent liquid flow, without free-surface effects. The absence of a free surface is justified in the case of ripples, as these forms do not scale with the flow depth. Franklin's analysis was based on four equations, which describe the mass conservation of granular matter, fluid flow perturbation caused by the bed shape, the transport of granular matter by a fluid flow, and the relaxation effects related to the transport of grains. Although Franklin [4] presented the main mechanisms of ripple formation, he neglected the effects of the threshold shear stress for grain displacement, the bed compactness, and the settling velocity of grains on bed stability. These effects were considered by Franklin [11].

The conservation equations used in this analysis are the mass conservation of granular matter and the momentum balance between the liquid and the grains. The mass conservation of grains in two dimensions relates the local height of the bed, h, to the local transport rate (volumetric) of grains per unit width q:

$$\frac{\partial h}{\partial t} + \frac{1}{\phi}\frac{\partial q}{\partial x} = 0, \tag{1}$$

where t is the time, x is the longitudinal direction and ϕ is the bed compactness. The momentum balance between the liquid and the grains is usually obtained by dimensional analysis, as there is no consensus about the rheology of granular matter. Semi-empirical momentum balances between the liquid and the grains were proposed in the previous decades, and the obtained expressions relate the bed-load transport rate to the shear stress caused by fluid flow on a granular bed. The expression proposed by Meyer-Peter and Müller [12], one of the most frequently used transport rate equations, is based on data from exhaustive experiments, and for this reason, it is used in the present model. The volumetric transport rate of grains per unit width q_0 for a fully developed flow [12] is given by

$$q_0 = D_1 \left(\tau_0 - \tau_{th}\right)^{3/2}, \tag{2}$$

where τ_0 is the shear stress on the granular bed caused by the fully developed flow (the unperturbed, basic state flow described next) and τ_{th} is the threshold shear stress for the incipient motion of grains [1]. D_1 is given by:

$$D_1 = \frac{8}{\rho^{3/2}\left[(S-1)\,g\right]}, \tag{3}$$

where ρ is the specific mass of the liquid, $S = \rho_p/\rho$, ρ_p is the specific mass of the grain material and g is the acceleration of gravity. According to Eq. (3), D_1 is constant for given fluid and grain types.

The basic state corresponds to a fully-developed turbulent boundary layer over a flat granular bed. For a two-dimensional boundary layer, the fluid velocity profile is given by [13]

$$u = \frac{u_*}{\kappa}\ln\left(\frac{y}{y_0}\right), \tag{4}$$

where $u(y)$ is the longitudinal component of the mean velocity, $\kappa = 0.41$ is the von Kármán constant, y is the vertical distance from the bed, y_0 is the roughness length and $u_* = \rho^{-1/2}\tau_0^{1/2}$ is the shear velocity.

In the steady state regime without spatial variations (flat bed), the fully developed fluid flow is given by Eq. (4). In this case, the fluid flow and the flow rate of grains are in equilibrium. This means that the available momentum for transporting grains as bed load is limited because part of the fluid momentum is transferred to the moving grains, which in turn transfer a part of the transferred fluid momentum to the fixed layers of the granular bed and another part to the interstitial fluid (mainly for liquids), until an equilibrium condition is reached. The equilibrium transport rate of grains is called *saturated transport rate* and is given by Eq. (2).

The origin of perturbations in this problem is the initial undulation of the granular bed. The bed undulation causes deviations from the basic state in both the fluid flow and the bed-load transport rate, thereby perturbing them. If the bed undulation is of a small aspect ratio, as expected for initial instabilities, the perturbations in the fluid flow and in the transport rate may be assumed as being small and a linear model can be used. The equations for these perturbations are presented next.

In the previous decades, many analytical works were focused on the perturbation of a turbulent boundary layer by bedforms. Among them, we cite Jackson and Hunt [14], Hunt et al. [15], and Weng et al. [16] here. Sauermann [17] and Kroy et al. [18, 19] simplified the results of Weng et al. [16] for surface stress and obtained an expression containing only the dominant physical effects of the perturbation. For a hill with local height h and a length $2L$ between the half-heights, they obtained the perturbation of the longitudinal shear stress (dimensionless):

$$\hat{\tau}_k = Ah(|k| + iBk), \tag{5}$$

where A and B are considered as constants, $k = 2\pi\lambda^{-1}$ is the longitudinal wavenumber, λ is the wavelength, and $i = \sqrt{-1}$. The shear stress on the bed surface is given as

$$\tau = \tau_0(1 + \hat{\tau}). \tag{6}$$

When the fluid flow is perturbed by the undulated bed, the bed-load transport rate varies locally. If equilibrium is assumed between the fluid flow and the bed-load transport rate, which is equivalent to neglecting the inertia of grains, then the transport rate is locally saturated and obtained by replacing τ_0 in Eq. (2) with τ (Eq. (6)). A convenient way to express this perturbed-saturated transport rate q_{sat} is:

$$\frac{q_{sat}}{q_0} = (1 + D_2\tau)^{3/2}, \tag{7}$$

where $D_2 = \tau_0 (\tau_0 - \tau_{th})^{-1}$ is a term that quantifies how far the flow is from the threshold. Fourrière et al. (2010) [8] proposed a more sophisticated expression for the perturbed-saturated transport rate, however, the form used here (Eq. (7)) is simpler while allowing to analyze threshold effects.

In the case of a spatially varying perturbed flow, a relaxation effect exists between the fluid and the grains owing to the inertia of the latter [20]. For this reason, the bed-load transport rate will lag behind the fluid flow by a certain distance, which is usually referred to as *saturation length*, L_{sat}. Andreotti et al. [20] proposed the following expression to take into account the relaxation effect:

$$\frac{\partial q}{\partial x} = \frac{q_{sat} - q}{L_{sat}}. \tag{8}$$

For the specific case of bed load under liquid flows, Charru (2006) [21] proposed that the saturation length L_{sat} is proportional to a deposition length $l_d = \frac{u_*}{U_s} d$:

$$L_{sat} = C_{sat} \frac{u_*}{U_s} d, \tag{9}$$

where U_s is the settling velocity of a single grain and C_{sat} is a constant of proportionality. The saturation length given by Eq. (9) is experimentally supported by Franklin and Charru (2011) [22].

Another parameter affecting bed stability is the local slope of the bed: the gravitational field weakens the transport of grains over positive slopes. One simple way to take into account this effect is to compute the effective shear stress perturbation by replacing B in Eq. (5) with $B_e = B - B_g/A$ so that the perturbed stress takes into consideration the grain weight and the shear between the grains, in addition to the shear caused by the fluid flow [21].

Taking into account that the initial instabilities are of a small aspect ratio, solutions h and q to Eq. (1), Eq. (6), Eq. (7), and Eq. (8) are plane waves. They can be decomposed into their normal modes as follows:

$$h(x,t) = He^{i(kx - \Omega t)} + c.c., \tag{10}$$

$$\frac{q(x,t)}{q_0} = 1 + Qe^{i(kx - \Omega t)} + c.c., \tag{11}$$

where $k \in \mathbb{R}$, $\lambda \in \mathbb{R}$, *c.c.* denotes "complex conjugate", and $H \in \mathbb{C}$ and $Q \in \mathbb{C}$ are the amplitudes. Let $\Omega \in \mathbb{C}$, $\Omega = \omega + i\sigma$, where $\omega \in \mathbb{R}$ is the angular frequency and $\sigma \in \mathbb{R}$ is the growth rate. Inserting the normal modes in Eq. (1), Eq. (6), Eq. (7), and Eq. (8), and finding the non-trivial solution gives the growth rate (Eq. (12)) and the phase velocity $c = \omega/k$ (Eq. (13)):

$$\sigma = \frac{3}{2}\frac{Aq_0D_2}{\phi}\frac{k^2(B_e - |k|L_{sat})}{1 + (kL_{sat})^2}, \tag{12}$$

$$c = \frac{3}{2}\frac{Aq_0D_2}{\phi}\frac{|k|(1 + B_eL_{sat}|k|)}{\left(1 + (kL_{sat})^2\right)^2}. \tag{13}$$

2.1 Pressure-driven Gas-Liquid Stratified Flow

A common case in industry is the presence of bed load in stratified gas-liquid flows in horizontal ducts. Franklin [10] presented a model for the estimation of some bed-load characteristics. Based on parameters easily measurable in industry, the model can predict the local bed-load flow rates and the celerity and wavelength of instabilities appearing on the granular bed.

Following Cohen and Hanratty [23], Franklin [10] integrated in the y direction the x component of the momentum equation of both the mean gas and the mean liquid flows. For the gas, the integration was from $y = H_0$ to y, where $y = H_0$ is the liquid-gas interface at the basic state, and for the liquid the integration was from the granular bed surface at the basic state $y = h_0$ to $y = H_0$. As an output, Eq. (14) is obtained, relating the shear stress on the granular bed to the pressure gradient (dp/dx) of the flow and to the position of the maximum of the velocity profile at the basic state $y = a_0$.

$$\tau_0 = (a_0 + H_0)\left(-\frac{dp}{dx}\right) \tag{14}$$

The pressure gradient can be measured by pressure transducers installed along the flow-line. If they are absent, the pressure gradient may be estimated by the Lockhart-Martinelli correlations for gas-liquid flows [24, 25]. However, these correlations have limitations and intrinsic uncertainties are introduced. Franklin [10] performed a linear stability analysis and found that, for the most unstable mode within a long-wave approximation:

$$\lambda_{max} \sim \left(-\frac{dp}{dx}\right)^{(1/2)} \tag{15}$$

$$\sigma_{max} \sim \left(-\frac{dp}{dx}\right)^{(1/2)} \tag{16}$$

$$c_{G,max} \sim \left(-\frac{dp}{dx}\right) \tag{17}$$

2.2 Comparison with Experimental Results

Next, the results of the above-presented analysis are compared with published experimental results. In particular, the reported results of three experimental studies, which addressed the formation of aquatic ripples in closed conduits and pipes, are considered here. One of the studies was of Coleman et al. [26], who experimentally studied bed instabilities in a $6\,m$ long horizontal closed conduit with a rectangular cross section

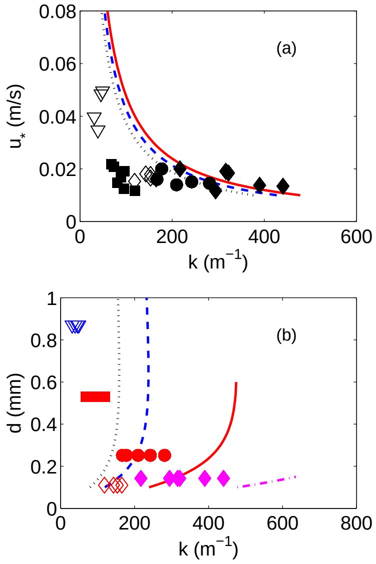

Figure 1: (a) Curves of marginal stability in terms of u_* for different values of B_g. The continuous, dashed and dotted curves correspond to $B_g = 0$, $B_g = 0.01$, and $B_g = 0.02$, respectively. (b) Curves of marginal stability in terms of d for different values of u_*, where all the parameters affected by d were also varied. The dashed-dotted, continuous, dashed, and dotted curves correspond to $u_* = 0.01\,m/s$, $u_* = 0.02\,m/s$, $u_* = 0.04\,m/s$, and $u_* = 0.06\,m/s$, respectively. The symbols correspond to experimental data and are described in the text. Figure extracted from Franklin (2015) [11]

($300\,mm$ wide by $100\,mm$ high) and employed water as the fluid medium and glass beads as the granular medium. The experiments were performed in a fully turbulent regime, with Reynolds numbers $Re = UH/\nu$ in the range $26000 < Re < 70000$ (where H is the channel height, ν is the kinematic viscosity, and U is the mean velocity of the fluid). Another study considered here is of Franklin [27], who experimentally studied initial instabilities in a $6\,m$ long horizontal closed conduit with a rectangular cross section ($120\,mm$ wide by $60\,mm$ high). The experiments were performed in a fully turbulent regime, with Reynolds numbers within the range $13000 < Re < 24000$. Finally, the study of Kuru et al. (1995) [28] is considered here. Kuru et al. (1995) [28] performed experiments on a $7m$ long, $31.1mm$ diameter horizontal pipe, and employed mixtures of water and glycerin as the fluid medium and glass beads as the granular medium.

Figure (1) shows a comparison of the curves of marginal stability obtained in this study [11] with the corresponding experimental data of Coleman et al. [26] and Franklin [27]. In this figure, the open diamonds and inverted triangles, taken from Coleman et al. [26], correspond to $d = 0.11\,mm$ and $d = 0.87\,mm$ glass spheres, respectively, under different shear velocities. The filled diamonds, circles, and squares, taken from Franklin [27], correspond to glass spheres with $d = 0.14\,mm$, $d = 0.25\,mm$, and $d = 0.53\,mm$, respectively, under different shear velocities.

Figure (1)(a) shows the curves of marginal stability in terms of u_* for different values of B_g, where the continuous, dashed, and dotted curves correspond to $B_g = 0$, $B_g = 0.01$, and $B_g = 0.02$, respectively. The model results are in agreement with experimental data, since all the measured ripples, with the exception of a few ripples with $d = 0.14mm$, lie in the predicted unstable regions. The measured ripples that are not in the unstable region are close to the marginal curves. This discrepancy may be related to experimental uncertainties, but a more probable reason pertains to some model parameters whose values are not well known. One of them is C_{sat}, whose value has not yet been measured in the aquatic case, and the other parameter is the threshold shear. In the present analysis, the Shields parameter at the bed-load threshold, i.e., $\theta_{th} = u_{*,th}/\left((S-1)gd\right)$, where $u_{*,th}$ is the corresponding shear velocity [1], was fixed at 0.04. However, there is no real consensus about this value, which may vary between 0.02 and 0.06 in the present case [29, 30, 31, 32].

Figure (1)(b) shows the curves of marginal stability in terms of d for different values of u_*, where all the parameters affected by d were varied accordingly. The dashed-dotted, continuous, dashed, and dotted curves correspond to $u_* = 0.01\,m/s$, $u_* = 0.02\,m/s$, $u_* = 0.04\,m/s$, and $u_* = 0.06\,m/s$, respectively. Considering that the open diamonds and inverted triangles correspond to $0.015\,m/s < u_* < 0.019\,m/s$ and $0.034\,m/s < u_* < 0.050\,m/s$, respectively, and that the filled diamonds, circles, and squares correspond to $0.011\,m/s < u_* < 0.020\,m/s$, $0.012\,m/s < u_* < 0.021\,m/s$, and $0.011\,m/s < u_* < 0.022\,m/s$, respectively, it can be confirmed that all the measured ripples lie in the predicted unstable regions and that the curves of marginal stability obtained in this study agree well with the published experimental data.

There is a lack of experiments in the scope of the formation of ripples in pressure-driven stratified liquid flows, even if there is a large number of industrial applications. However, the analysis can be compared with experimental data of pressure driven liquid flows carrying grains as bed load. Although the cases are different, the initial instabilities may scale in a similar manner, given that the initial bedforms have small amplitudes and are not expected to be affected by the presence of a free surface. There studies of Kuru et al. (1995) [28] and Franklin (2008) [27] are considered here. In both works, the authors measured the wavelengths of the initial bedforms appearing on the granular bed.

The results of both works are summarized in Figure (2). In order to directly compare the experimental data with the present model (Eq. (15), Eq. (16) and Eq. (17)), Figure (2) presents the dimensionless wavelength λ/d of initial ripples as a function of the square root of the dimensionless pressure gradient $(-dp/dx)^{1/2}(a_l/\rho_l)^{1/2}(1/U_s)$, where a_l is the distance from the maximum of the liquid velocity profile to the bed. Filled symbols correspond to the experimental data of Kuru et al. (1995) [28] and open symbols to the experimental data of Franklin (2008) [27]. The description of each symbol is in the legend of Figure (2). The dimensionless parameters of Figure (2) come from Eq. (14) and Eq. (9), considering that $u_* = \sqrt{\tau_0/\rho_l}$ and changing $(a_0 + H_0)$ by a_l. In this case, we find that

$$\frac{\lambda}{d} \sim \left(-\frac{dp}{dx}\right)^{1/2}\left(\frac{a_l}{\rho_l}\right)^{1/2}\frac{1}{U_s} \qquad (18)$$

If we take into account the relatively high uncertainties, often present in measurements of bed instabilities, the alignment of the experimental data in Figure (2) seems to support the results of the proposed model, that the wavelength of initial bedforms varies as $(-dp/dx)^{1/2}$, even if the experimental data were obtained for a case different from the scope of the model.

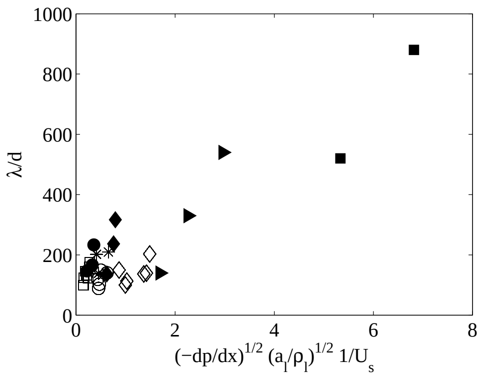

Figure 2: Dimensionless wavelength λ/d as a function of the square root of the dimensionless pressure gradient $(-dp/dx)^{1/2}(a_l/\rho_l)^{1/2}(1/U_s)$. Filled circles, lozenges, triangles and squares correspond to $d = 0.3mm$ and $\mu_l = 1cP$, $d = 0.3mm$ and $\mu_l = 2.2cP$, $d = 0.1mm$ and $\mu_l = 1cP$, and $d = 0.1mm$ and $\mu_l = 2.1cP$, respectively (experimental data of Kuru et al., 1995 [28]). Open lozenges, circles, squares and asterisks correspond to $d = 0.12mm$, $d = 0.20mm$ and $d = 0.50mm$ glass beads (in water), and to $d = 0.19mm$ zirconium beads (in water), respectively (experimental data of Franklin, 2008 [27]). Figure extracted from Franklin (2013) [10]

3 Weakly Nonlinear Analysis

In order to understand the evolution of ripples after the linear phase of the instability, i.e., in a time-scale greater than σ^{-1}, Franklin [5] presented a nonlinear stability analysis in the same scope of [4]. The approach used was the weakly nonlinear analysis [33], useful whenever a dominant mode exists. This means that the modes resonating with the dominant one will grow much faster than the others, which can be neglected. The analysis is then made on a bounded number of modes. A small modification in the analysis of [5] was proposed by Franklin [9]. Eq. (1) to Eq. (9) can be combined to give a single equation

$$\begin{aligned} &\partial_t h + B_1(h)^2 + B_2(\partial_x h)^2 \\ &+B_3 h\partial_x h + B_4 h + B_5\partial_x h - ch = 0 \qquad (19) \end{aligned}$$

where c is the celerity of the bedforms and B_1 to B_5 involve q_0, L_{sat} and some constants, so that B_1 to B_5 are only functions of u_* and d. They may then be treated as constants in an analysis of a given granular bed submitted to a given fluid flow.

In the weakly nonlinear analysis we are interested in the early stages of the nonlinear instability, when the exponential growth is no longer valid and the nonlinear terms become pertinent. In this case, it is a reasonable assumption to consider that the celerity c of bedforms is approximately the celerity of the linear phase. The linear analysis showed that the celerity of the initial instabilities is given by $c \sim q_0/Lsat$, so that $c \sim u_*(u_*d/U_s)^{-1}$. With this assumption, c may be treated as a constant in an analysis of a given granular bed submitted to a given fluid flow. The last term of Eq. (19) is then considered here as varying with h.

In this problem, the large scales are limited by periodicity and the small ones by the discrete nature of the grains; therefore, a limited number of Fourier components can be considered. These modes can be inserted in Eq. (19) and the nonlinear terms maintained. Normalizing the problem by its characteristic length (k^{-1}), and inserting the normal modes into Eq. (19), one can find the following equation

$$\begin{aligned} &\tfrac{1}{2}\sum_{n=-\infty}^{\infty}\left[\frac{dA_n}{dt} + A_n(B_4 - c) + iB_5 nA_n\right]e^{inx} \\ &+\tfrac{1}{2}\sum_{n=-\infty}^{\infty}\left[A_n^2 B_1 + B_2(inA_n)^2\right]e^{2inx} \\ &+\tfrac{1}{2}\sum_{p=-\infty}^{\infty}\sum_{q=-\infty}^{\infty}\left[B_3 A_p iqA_q\right]e^{i(q+p)x} = 0 \qquad (20) \end{aligned}$$

By inspecting Eq. (20), Franklin [5] proposed that the third term may resonate with the linear part if $q+p = n$. By keeping only the resonant terms of Eq. (20), we find

$$\frac{dA_n}{dt} = \sigma_n A_n + iB_3\sum_{p=-\infty}^{\infty}\left[pA_{p+n}A_p^*\right] \qquad (21)$$

where $\sigma_n = c - B_4 - inB_5$.

Inspecting Eq. (21), it can be seen that σ_n contains the linear part of the problem and that the nonlinearities are in the third term. If the latter is neglected, which can be done in the initial phase of the instability, we find that the solution is stable for $\sigma_n < 0$ and unstable for $\sigma_n > 0$. In this case, $c - B_4$ is the parameter controlling the threshold of the instability: given the scales of c, the basic state is stable when $u_*/L_{sat} < B_4$ and it is unstable when $u_*/L_{sat} > B_4$, and the constant B_4 may be seen as a threshold value. We retrieve the conclusion of the linear analysis of [4], that there is a cut-off wavelength that scales with both u_* and L_{sat}, the small wavelengths being stable.

Franklin [5] wrote Eq. (21) for the first three modes (for $n > 0$) and, on the onset of the instability, showed that: (i) the second and higher modes can be written as functions of the first mode; (ii) the first mode is a fundamental mode. An equation for the fundamental mode similar to the Landau Equation [33, 34] was then obtained

$$\frac{dA_1}{dt} = \sigma_1 A_1 - \kappa_L A_1 |A_1|^2 + O(A_1^5) \qquad (22)$$

where $\kappa_L = -B_3^2/\sigma_2 > 0$.

From Eq. (22), we can see that the nonlinear term will saturate the instability in a time-scale greater than σ^{-1}: after the initial exponential growth, the instability will be attenuated and eventually reach a finite value for the amplitude, maintaining the same wavelength. This corresponds to a supercritical bifurcation. This result is corroborated by some experimental works [28, 27], as discussed in [5].

Acknowledgment

The author is grateful to FAPESP (grant no. 2012/19562-6), to CNPq (grant no. 471391/2013-1) and to FAEPEX/UNICAMP (conv. 519.292, project 0201/14) for the provided financial support.

References

[1] R. A. Bagnold, *The physics of blown sand and desert dunes.* Chapman and Hall, 1941.

[2] A. J. Raudkivi, *Loose boundary hydraulics.* Pergamon Press, 1 ed., 1976.

[3] F. Engelund and J. Fredsoe, "Sediment ripples and dunes," *Ann. Rev. Fluid Mech.*, vol. 14, pp. 13–37, 1982.

[4] E. M. Franklin, "Initial instabilities of a granular bed sheared by a turbulent liquid flow: length-scale determination," *J. Braz. Soc. Mech. Sci. Eng.*, vol. 32, no. 4, pp. 460–467, 2010.

[5] E. M. Franklin, "Nonlinear instabilities on a granular bed sheared by a turbulent liquid flow," *J. Braz. Soc. Mech. Sci. Eng.*, vol. 33, pp. 265–271, 2011.

[6] A. J. Raudkivi and H. H. Witte, "Development of bed features," *J. Hydraul. Eng.*, vol. 116, pp. 1063–1079, 1990.

[7] A. J. Raudkivi, "Transition from ripples to dunes," *J. Hydraul. Eng.*, vol. 132, pp. 1316–1320, 2006.

[8] A. Fourrière, P. Claudin, and B. Andreotti, "Bedforms in a turbulent stream: formation of ripples by primary linear instabilities and of dunes by nonlinear pattern coarsening," *J. Fluid Mech.*, vol. 649, pp. 287–328, 2010.

[9] E. M. Franklin, "Linear and nonlinear instabilities of a granular bed: determination of the scales of ripples and dunes in rivers," *Appl. Math. Model.*, vol. 36, pp. 1057–1067, 2012.

[10] E. M. Franklin, "Prediction of the bed-load transport by gas-liquid stratified flows in horizontal ducts," *Appl. Math. Model.*, vol. 37, pp. 5627–5636, 2013.

[11] E. M. Franklin, "Formation of sand ripples under a turbulent liquid flow," *Appl. Math. Model.*, 2015.

[12] E. Meyer-Peter and R. Müller, "Formulas for bed-load transport," in *Proc. 2nd Meeting of International Association for Hydraulic Research*, pp. 39–64, 1948.

[13] H. Schlichting, *Boundary-layer theory.* Springer, 2000.

[14] P. S. Jackson and J. C. R. Hunt, "Turbulent wind flow over a low hill," *Quart. J. R. Met. Soc.*, vol. 101, pp. 929–955, 1975.

[15] J. C. R. Hunt, S. Leibovich, and K. J. Richards, "Turbulent shear flows over low hills," *Quart. J. R. Met. Soc.*, vol. 114, pp. 1435–1470, 1988.

[16] W. S. Weng, J. C. R. Hunt, D. J. Carruthers, A. Warren, G. F. S. Wiggs, I. Livingstone, and I. Castro, "Air flow and sand transport over sand-dunes," *Acta Mechanica*, pp. 1–21, 1991.

[17] G. Sauermann, *Modeling of wind blown sand and desert dunes.* PhD thesis, Universität Stuttgart, 2001.

[18] K. Kroy, G. Sauermann, and H. J. Herrmann, "Minimal model for aeolian sand dunes," *Phys. Rev. E*, vol. 66, no. 031302, 2002.

[19] K. Kroy, G. Sauermann, and H. J. Herrmann, "Minimal model for sand dunes," *Phys. Rev. Lett.*, vol. 88, no. 054301, 2002.

[20] B. Andreotti, P. Claudin, and S. Douady, "Selection of dune shapes and velocities. part 2: A two-dimensional model," *Eur. Phys. J. B*, vol. 28, pp. 341–352, 2002.

[21] F. Charru, "Selection of the ripple length on a granular bed sheared by a liquid flow," *Phys. Fluids*, vol. 18, no. 121508, 2006.

[22] E. M. Franklin and F. Charru, "Subaqueous barchan dunes in turbulent shear flow. Part 1. Dune motion," *J. Fluid Mech.*, vol. 675, pp. 199–222, 2011.

[23] L. S. Cohen and T. J. Hanratty, "Effect of waves at a gas-liquid interface on a turbulent air flow," *J. Fluid Mech.*, vol. 31, pp. 467–479, 1968.

[24] R. C. Martinelli and D. B. Nelson, "Prediction of pressure drop during forced-circulation boiling of water," *Trans. ASME*, vol. 70, pp. 695–702, 1948.

[25] R. W. Lockhart and R. C. Martinelli, "Proposed correlation of data for isothermal two-phase, two-component flow in pipes," *Chem. Eng. Prog.*, vol. 45, pp. 39–48, 1949.

[26] S. E. Coleman, J. J. Fedele, and M. H. Garcia, "Closed-conduit bed-form initiation and development," *J. Hydraul. Eng.*, vol. 129(12), pp. 956–965, 2003.

[27] E. M. Franklin, *Dynamique de dunes isolées dans un écoulement cisaillé.* PhD thesis, Université de Toulouse, 2008.

[28] W. C. Kuru, D. T. Leighton, and M. J. McCready, "Formation of waves on a horizontal erodible bed of particles," *Int. J. Multiphase Flow*, vol. 21, no. 6, pp. 1123–1140, 1995.

[29] P. Mantz, "Incipient transport of fine grains and flakes by fluids - extended Shields diagram," *J. Hydraul. Div.*, vol. HY6, pp. 601–615, 1977.

[30] M. S. Yalin and E. Karahan, "Inception of sediment transport," *J. Hydraul. Div.*, vol. HY11, pp. 1433–1443, 1979.

[31] R. L. Soulsby and R. J. S. Whitehouse, "Threshold of sediment motion in coastal environments," in *13th Australasian Coastal and Engineering Conference and 6th Australasian Port and Harbour Conference*, (Christchurch, New Zealand), pp. 149–154, 1997.

[32] J. M. Buffington and D. R. Montgomery, "A systematic analysis of eight decades of incipient motion studies, with special reference to gravel-bedded rivers," *Water Resour. Res.*, vol. 33, pp. 1993–2029, 1997.

[33] L. D. Landau and E. M. Lifshitz, *Fluid mechanics.* Pergamon Press, 1959.

[34] P. G. Drazin and W. R. Reid, *Hydrodynamic Stability.* Cambridge University Press, 2 ed., 2004.

Optical Methods for Fluid Mechanics Measurements: Developments and Applications

L.F.A. Azevedo and I.B. de Paula
Fluids Engineering Laboratory,
Department of Mechanical Engineering, PUC-Rio
22451-900, Rio de Janeiro, Brazil
Lfaa@puc-rio.br, Igorbra@gmail.com

Abstract

The studies conducted in the Laboratory of Fluids Engineering at PUC-Rio are described in the present report. Attention is focused on the developments of optical techniques for two-phase flow measurements and three dimensional single phase measurements.

1 Introduction

The Laboratory of Fluids Engineering at the Pontifical Catholic University of Rio de Janeiro, PUC-Rio, is dedicated to the development and application of experimental techniques for studying heat and mass transfer, and fluid mechanics problems. The work conducted along the years included experimental studies on natural convection and jet impinging heat and mass transfer, and turbulent channel flow (e.g., [1-3]). In the last decades the laboratory has focused on the study of two-phase flows, turbulent flows in pipes, and deposition of paraffins in pipes. A considerable part of the research effort involved the development and utilization of optical techniques for qualitative and quantitative fluid flow studies. The following is a description of representative work in the area of optical techniques applied to fluid flow studies

2 Two-phase Flow Experiments

2.1 Time-resolved Laser-Induced Fluorescence for Annular Two-Phase Flow Studies

In horizontal annular flow the liquid flows as a thin non-uniform film around the tube walls, while gas flows in the pipe core. The liquid film in this flow regime presents a wavy structure formed by ripples on the base film moving at low velocities and larger and faster disturbance waves. Droplets entrained in the gas flow are also part of the liquid transport.

The measurement and prediction of the time-varying, non-uniform liquid film distribution around the pipe perimeter that characterizes this class of flow has been one of the main focuses of research in the literature, together with the prediction of pressure losses along the pipe. One of the key fundamental questions related to the liquid film behavior is related to the mechanisms that maintain the film at the upper pipe wall, compensating drainage induced by gravity.

Typical liquid films in horizontal annular flow range from tens of micrometers to a few millimeters in thickness. The work conducted is part of an ongoing research project aimed at providing simultaneous, time-resolved qualitative and quantitative information on the liquid film structure in horizontal annular flows. The experimental technique implemented employs index of refraction matching techniques associated with Planar Laser-induced Fluorescence - PLIF. High frame rate cameras synchronized with high-repetition rate lasers were used to provide time-resolved, quality images of longitudinal and cross section views of the liquid film around the pipe perimeter. In the case of cross section views, two cameras were used in a stereoscopic arrangement. Calibration targets were used to dewarp the images obtained from the side viewing of the pipe cross section. Instantaneous images of the film were processed to enhance contrast and to extract the time dependent properties of the liquid film such as, film thickness, time-averaged and RMS values of film thickness, frequency power spectra, wave velocity, and histograms of liquid wave amplitude distributions.

Figure 1(a) presents a schematic view of the test section utilized in the experiments for measuring the liquid film at the lower part of the tube. Water from a pump was fed to a 15-mm-diameter FEP tube. Air and water were mixed at a tee connection located at the inlet section of the tube. A rectangular visualization box filled with water was used in order to minimize optical distortions due to the pipe wall curvature. A dual-cavity, Nd-YLF, high-repetition laser provided illumination of a longitudinal section of the tube as a planar light sheet with dimensions of 20 mm wide by 0.5-mm thick. The light sheet coming from the laser entered vertically through the bottom wall of the visualization box and passed through the FEP pipe, illuminating a longitudinal section of the air-water flow inside the pipe, as indicated in Fig. 1(b).

Images of the lower portion of the liquid film were captured using a high-frame-rate camera operating from 250 to 3000 frames per second at a pixel resolution of 512 x 512 pixels. A synchronizer was used to synchronize laser firing and image capture. A high pass optical filter with a cutoff wave length of 560 nm was installed in front of the camera lens to block the 527-nm green laser light scattered by the air-water interfaces. With the filter installed, the camera only registered the 610-nm fluorescence light emitted by the Rhodamine dissolved in the water. Pixel calibration of the images was obtained by using a target inserted into the test pipe through its exit section, after the removal of the return pipe connection.

Cross sectional views of the liquid film were obtained by an optical setup employing two high frame rate cameras mounted at an angle, as indicated in Fig. 2(a). In this case, the light sheet was rotated by 90° so as to illuminate a cross section of the pipe. The two cameras

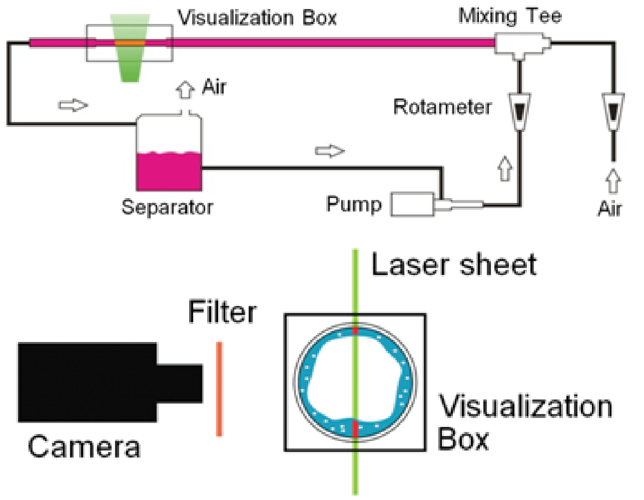

Figure 1: (a) Schematic view of the test section. (b) Optical setup for longitudinal film visualization

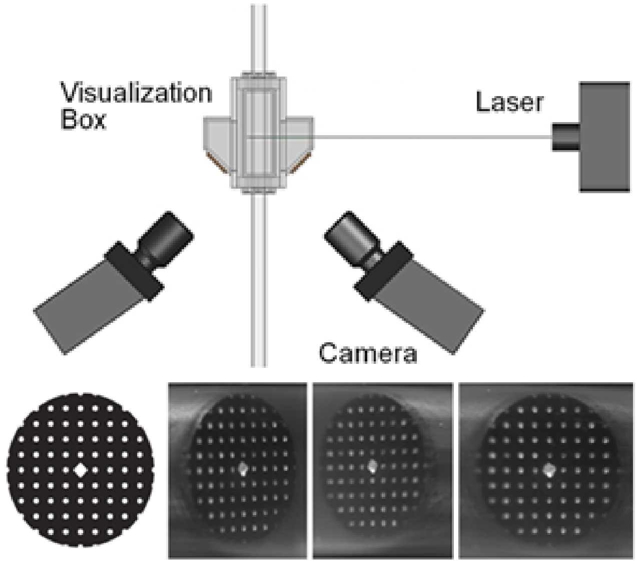

Figure 2: (a) Top view of optical setup for cross section liquid film visualization. (b) Calibration target, target as imaged by left and right cameras and after application of dewarping procedure and joining operation

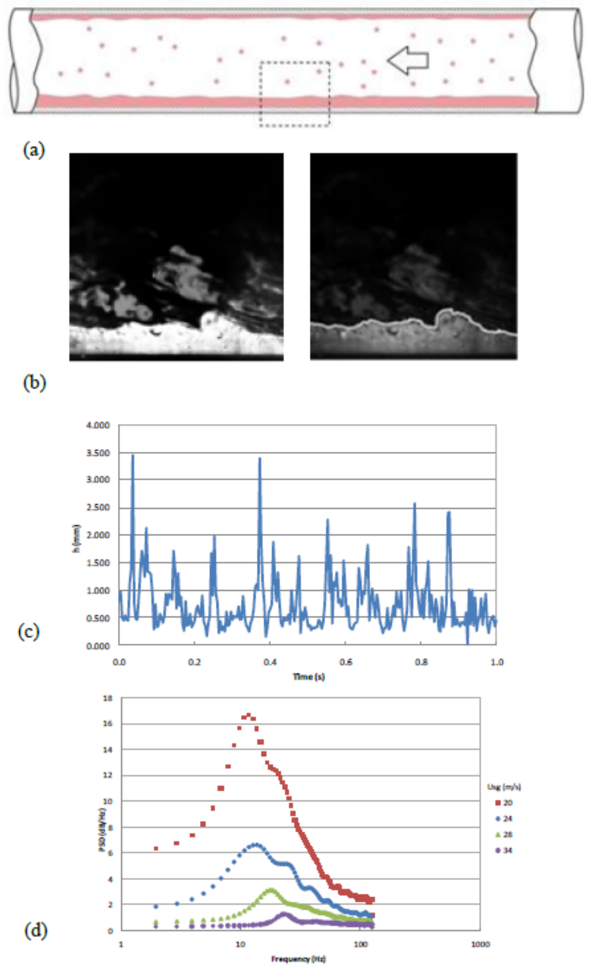

Figure 3: (a) Schematic view of the measured film location. (b) Typical raw and processed images (c) Measured instantaneous film thickness (d) Power spectra density (PSD) of thickness time records

were mounted at an angle of 45°, imaging the pipe cross section through the two 45-degree-inclined windows provided at the visualization box that surrounded the test tube. Each camera was mounted on a support that permitted that the camera body was rotated in relation to the lens axis. This setup allowed the attainment of the Scheimpflug condition. When this condition is attained, the whole image is focused, even though the camera is viewing the pipe cross section at an angle.

Image distortion due to the side camera viewing was corrected by a specially written program that used images of a cylindrical target captured by the left and right cameras. The target, is shown in Fig. 2(b).

Image processing procedures were specially developed and employed to enhance the captured images and to measure instantaneous film heights, as shown in the typical results of Figure 3. In the figure, a pictorial view of the annular flow indicates where the film images where captured. The captured images and the processed images with the film interface identified are also shown. The graphs shown in Fig. 3 are examples of the measured instantaneous film height and calculated power spectra.

Space-time maps were also obtained from the image processing procedures what allowed for useful insights into the interaction of ripple and disturbance waves, as indicated in Fig. 4. The time-resolved cross section images of the pipe produced information on the complete annular flow structure. A sequence of three typical instantaneous images showing the passage of a disturbance wave and a sample of a measured film thickness are presented in Figure 5.

This work is, in part, the result of the Master's Dissertation of P.S.C. Farias and had the collaboration of F.J.W.A. Martins, L.E.B. Sampaio, R. Serfaty, and it was published in [4].

2.2 Bubble Characterization in Horizontal Intermittent Two-Phase Flow

A study of bubble shape in intermittent two-phase flow was conducted employing a specially developed visualization technique where bubble passage triggered image capture. Quantitative information about shapes of the bubble nose and tail could be obtained by using a set of procedures for image acquisition and processing. For image acquisition, a set of photo gates was used to measure in real time the velocity and the properties of the

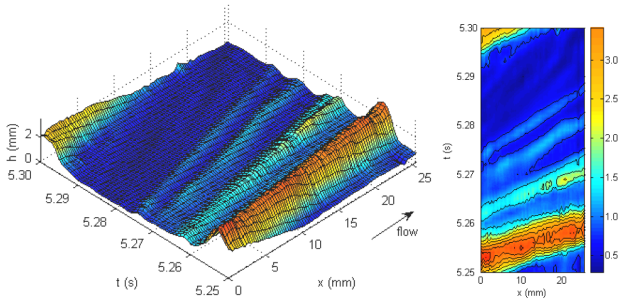

Figure 4: Space-time maps showing the evolution of the waves in the liquid film. Original images captured at $3000Hz$ with 512×512 pixel resolution

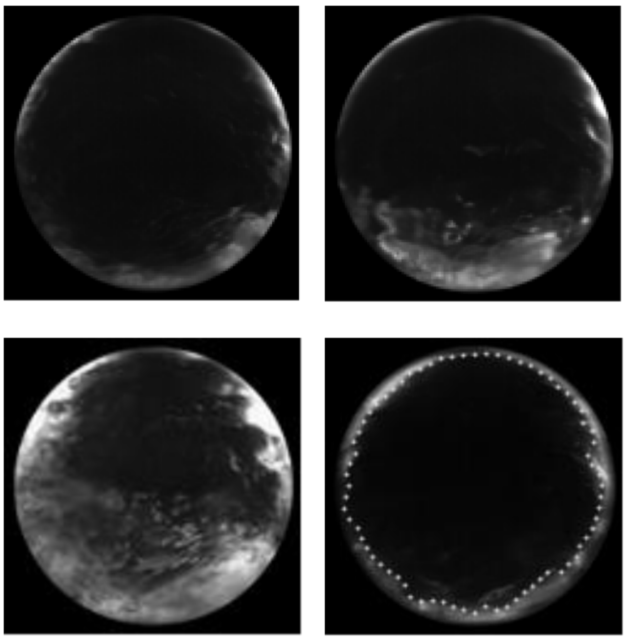

Figure 5: Instantaneous images of the cross sectional view of the passage of a disturbance wave. Original images captured at $2000Hz$ with 512×512 pixel resolution

slugs. Based on the measured velocities, an adaptive delay could be adjusted in real time to trigger image acquisition with the passage of each bubble. Thus, hundreds of images from the bubble nose and tail could be captured and ensemble averaged. The study focused on the transition from elongated bubble to slug flow regimes.

The results have shown that bubble translational velocities are dependent on the mixture Froude number, with rates close to those suggested by Woods and Hanratty [5]. This has evidenced the importance of the contribution of the drift velocity to the bubble translational velocity for low mixture velocities, as suggested in Bendiksen [6].

The radial movement of the bubble nose toward the pipe centerline as function of the mixture velocity was measured quantitatively, seemingly for the first time. The results indicated a linear dependence between bubble nose position and the mixture Froude number. Changes in the shape of the bubble tail at the transition from elongated bubble to slug flow regimes were also measured. The liquid film thicknesses were shown to scale linearly with the ratio of the superficial liquid velocity to the mixture velocity.

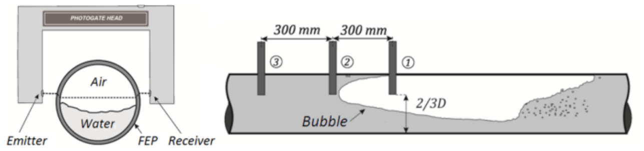

Figure 6: Triggering system for measuring bubble length, frequency and speed

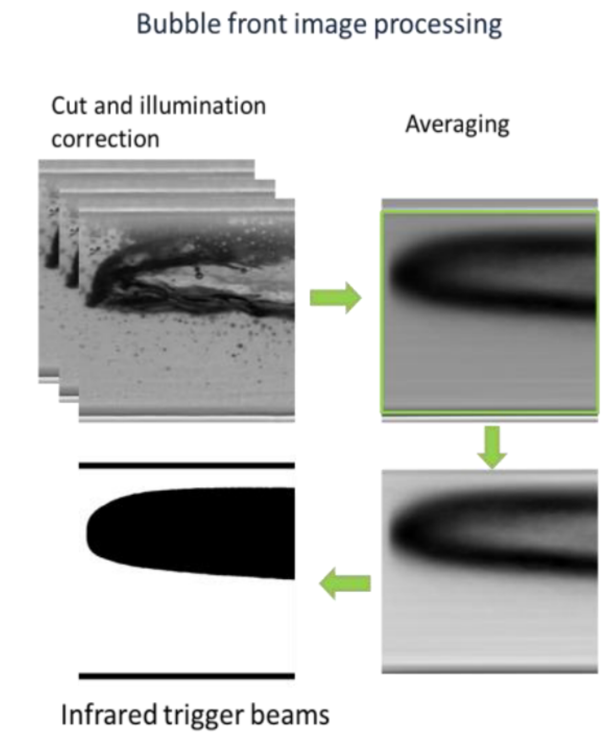

Figure 7: Image processing steps for determining the contour of the ensemble-averaged bubble nose image

Figure 6 shows the setup with the photogates for triggering the bubble nose or tail and synchronizing it with image capture. Figure 7 schematically demonstrates the image procedures steps to capture hundreds of bubble images producing the ensemble averaged bubble image. Measurements of bubble shape and nose position were performed on these ensemble averaged images with higher resolution, when compared to measurements made on instantaneous images.

Figure 8 is a representative result of the study where bubble shape and position were measured with the technique developed as function of the Froude number.

The present work was part of the Master's Dissertation of W.R. de Oliveira, with the collaboration of F.J.W.A. Martins and P.S.C. Farias. It was published in [7].

2.3 Liquid Velocity Measurements in Slug Flows

Planar particle image velocimetry - PIV was employed to measure instantaneous velocity fields in the nose and tail of gas bubbles in slug flows in horizontal and inclined pipes. To avoid reflections in the gas-liquid interface, fluorescent tracer particles were employed together with a high pass optical filter to block the green laser light scattered by the interfaces. Figure 9 displays a typical velocity field obtained at the nose and tail of a gas bubble in a horizontal slug flow. The same technique was employed

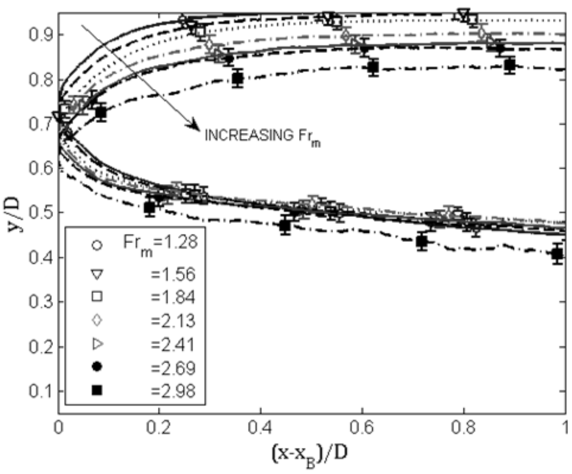

Figure 8: Measured bubble shape as a function of Froude number

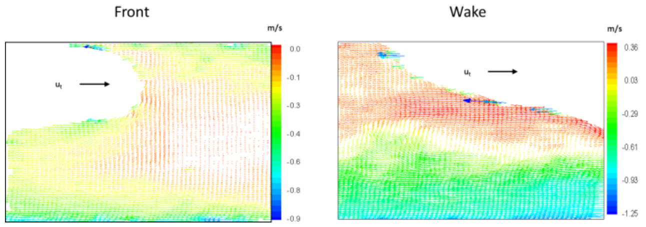

Figure 9: Instantaneous velocity fields measured by PIV with fluorescent particles at the nose and tail of a gas bubble in slug flow

to study the flow around Taylor bubbles ascending in a pipe. Figure 10 presents some representative results obtained.

This work is described in a paper published in [8].

3 Three-dimensional Velocity Measurements

This line of research conducted by the Laboratory of Fluids Engineering is dedicated to the development and application of optical techniques for measuring three dimensional instantaneous single phase flows in three dimensional regions. Two techniques are being developed as a result of a cooperation with the Laboratoire de Mécanique de Lille. These are the holographic particle image velocimetry and the tomographic particle velocimetry tecnhiques.

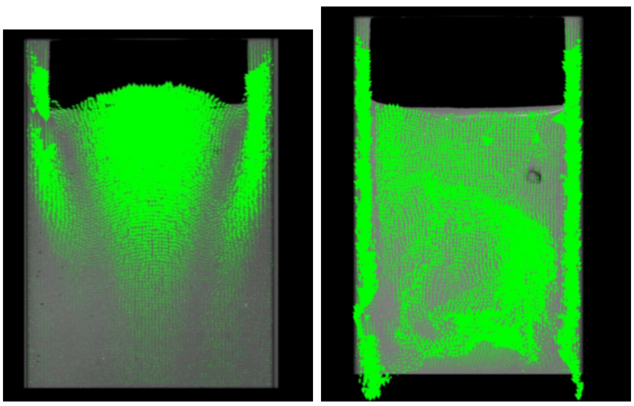

Figure 10: Instantaneous velocity field at the wake of ascending Taylor bubbles of different velocities

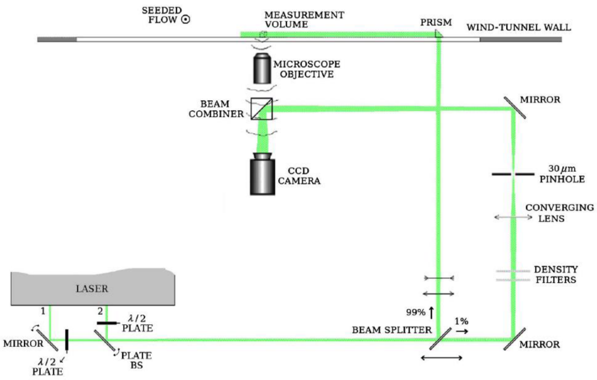

Figure 11: Dual-beam side-scattering setup with in-line holographic recording for near-wall wind tunnel flow measurements

3.1 Digital Holographic Flow Measurements

The setups for flow measurements using digital holography were developed in cooperation with the Laboratoire de Mécanique de Lille. A digital microscopic holography system for measuring micrometer particles in large scale wind tunnels was developed. The study of a $1.5mm^3$ volume near the tunnel wall was made possible by the use of a microscope objective for magnification of the objective field. Particles that are too small to be detected with standard in-line hologram are illuminated laterally, and the 90° scattered field is magnified and recombined with a reference wave for in-line recording. Analysis of the results shows that particle images reconstruct with very good axial accuracy. Preliminary tests have shown that this approach should allow measurements of fluid velocity very close to the wall in a wind tunnel flow. Figure 11 presents a sketch of the side scatter setup developed.

Standard in-line measurements are also presently been developed to be used in smaller water facilities.

This research was conducted in the Doctoral Thesis of J.K. Abrantes, as joint degree from the Université de Lille and PUC-Rio. The results have been published in [9].

3.2 Tomographic PIV for Volumetric Flow Measurements

The cooperation with the Laboratoire de Mécanique de Lille has been instrumental in allowing the development of the necessary skills in our laboratory to perform tomo-PIV measurements. To this end, a jointly advised Doctoral student, F.J.W.A. Martins, is working on the algorithms for the reconstruction of the multiple camera views. Also, an experimental setup is being assembled for performing time-resolved volumetric measurements in a $50-mm$-side square channel in turbulent flow using a 4-camera, tomo-PIV arrangement with a $30-mJ$ high repetition rate laser. A study of optimization of tomo-PIV algorithms has recently been accepted for publication in [10]. The square channel test section was designed to allow the introduction of drag reducing additives. This study will be carried out using the holo and

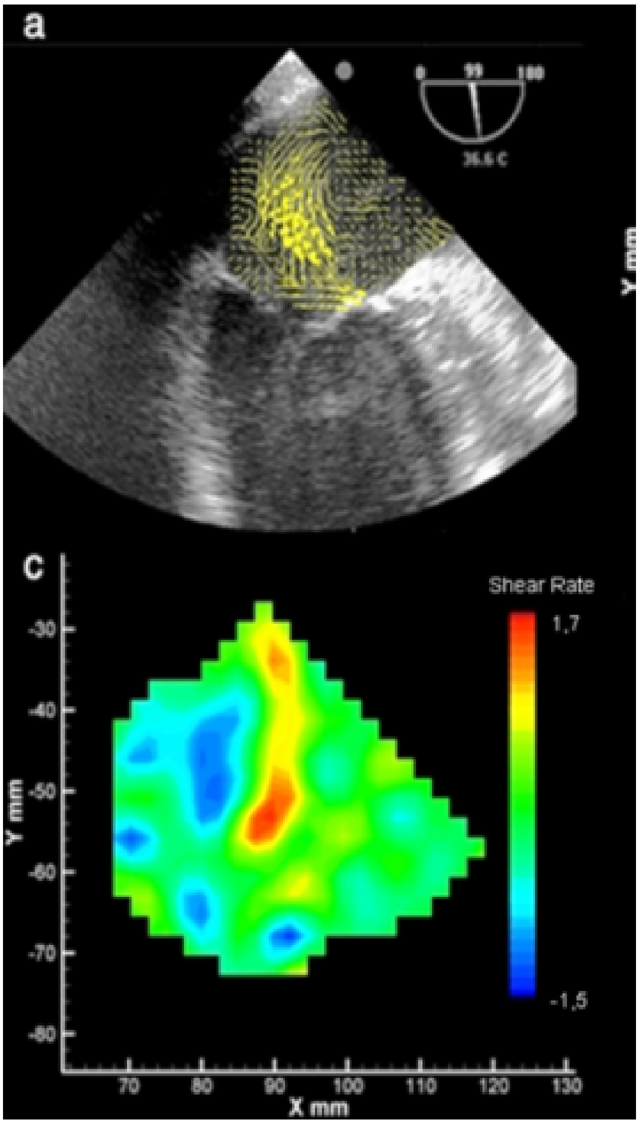

Figure 12: Velocity field and shear rate of a human heart obtained with echo-PIV technique using spontaneous contrast

tomo-PIV techniques, besides other standard flow measurement techniques

4 Cardiovascular Flow Measurements

Fluid flow measurements in arteries and heart chambers have been performed both in vivo and in vitro. In vivo measurements employed echocardiography and spontaneous contrast provided by the blood [11]. Figure 12 presents results obtained with PIV processing of the echo images of a human heart.

Presently, 3D printing techniques are being used to constructed models of the aorta artery based on tomographic images of patients. The printed models are being index-matched to fluids in order to allow three dimensional flow measurements.

References

[1] L. F. A. Azevedo, B.Webb, and M. Queiroz, "Pulsed air jet impingement heat transfer", Experimental Thermal and Fluid Science, vol. 8, no. 3 pp. 206-213, 1994.

[2] B.V.Loureiro, P.R. Souza-Mendes, and L.F.A. Azevedo, "Taylor-Couete instabilities in tangential annular flow of Newtonian and non Newtonian liquids in the presence of partial annulus obstruction", ASME Journal of Fluids Engineering, vol. 128, pp. 42-54, 2006.

[3] M.Y.Z Becerra, O.J. Romero, L.F.A. Azevedo, and M.S Carvalho, "Measuring the velocity field in film-splitting flows on Newtonian liquids", AIChE Journal, vol. 53, no. 2, pp. 281-289,2007.

[4] P.S.C. Farias, F.J.W.A. Martins, L.E.B. Sampaio, R. Serfaty and L.F.A Azevedo, "Liquid film characterization in horizontal, annular, two-phase, gas-liquid flow using time-resolved laser-induced fluorescence", Experiments in Fluids, vol. 53, pp. 633-645, 2012.

[5] B. D. Woods and T. J. Hanratty, "Relation of slug stability to sheeding rate", International Journal of Multiphase Flow, 22, pp. 809-828,1996.

[6] K.H. Bendiksen, "An experimental investigation of the motion of long bubbles in inclined tubes", International Journal of Multiphase Flow, n. 4 v.10, pp. 467-483, 1984.

[7] W.R. Oliveira, I.B. de Paula, F.J.W.A. Martins, P.S.C. Farias and L.F.A. Azevedo, "Bubble characterization in horizontal air-water intermittent flow", International Journal of Multiphase Flow, vol. 69, pp. 18-30, 2015

[8] J. N. E Carneiro, R. Fonseca Jr., A. J Ortega, R. C Chucuya, A. O Nieckele and L. F. A Azevedo, "Statistical characterization of two-phase slug flow in a horizontal pipe", Journal of the Brazilian Society of Mechanical Sciences and Engineering, 33, pp. 251-258, 2011.

[9] J.K. Abrantes, M. Stanislas, S. Coudert, L.F.A Azevedo, "Digital microscopic holography for micrometer particles in air", Applied Optics, vol. pp. A397-A409, 2013.

[10] F.J.W.A Martins, J.M. Foucaut, L.Thomas, L.F.A. Azevedo, and M. Stanislas, "Volume reconstruction optimization for tomo-PIV algorithms applied to experimental data" Meas. Sci. Technol. Vol. 26, doi:10.1088/0957-0233/26/8/085202, 2015.

[11] B.A. Azevedo, L.F.A Azevedo, R. Nunes, A.C.L. Nóbrega, "In vivo blood velocity measurements with particle image velocimetry in echocardiography using spontaneous contrast", Journal of the Brazilian Society of Mechanical Sciences and Engineering, vol. 37, pp. 559-569, 2015.

On the Transient Behaviour of the Drag Reducing Flows

E. J. Soares

LABREO, Department of Mechanical Engineering
Universidade Federal do Espirito Santo
Avenida Fernando Ferrari, 514, Goiabeiras, 29075-910 ES, Brazil

1 Introduction

Drag reduction (DR) has been widely analysed after the results reported by Toms [1] more than 60 years ago. Up to now, researchers have been successful in analysing the DR and drag reducers are used a number of applications as the transport of liquid in pipelines, fire-fighting operations, beyond others (see [2], [3], [4]).

It is very well known that many different variables play an important role on the DR efficiency, which turns the development of a new drag reducer a task very far from to be ease. Undoubtably, a careful analysis of DR must keep under the control the polymer concentration, molecular weight, temperatura and quality of the solvent, beyond another important variables as the polymer structure (linear or branched), shape (coiled or elongated), flexibility and elansticity. Many remarkable papers in which these variables are analysed can be found (see [5], [6]). Concerning the theory of DR, it is strongly recommended to start from the papers of Lumley [5] and Tabor and de Gennes [7] in which the two main basic ideas for explaining the mechanism of DR are introduced. The Lumley's idea is related to viscous effects, while Tabor and de Gennes propose an explanation based on polymeric elasticity. In fact, despite to the fact that other researches give support for each one of these two theories, none of them are generally accepted.

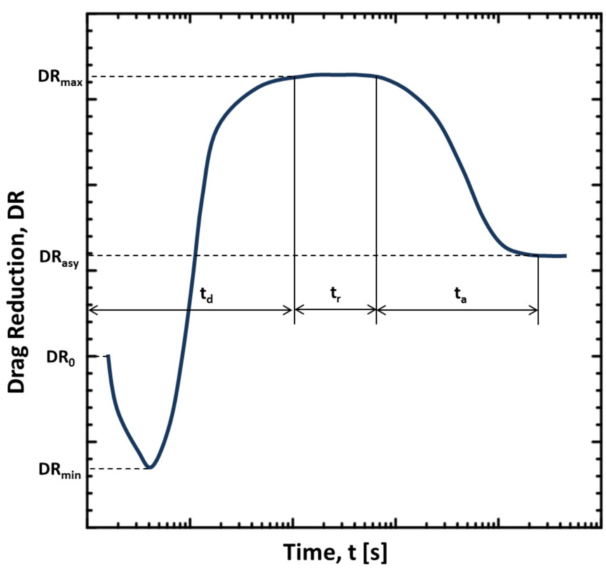

Figure 1: Sketch of the evolution over time of the polymer-induced drag reduction. Fig.1 from Pereira et al. [8]

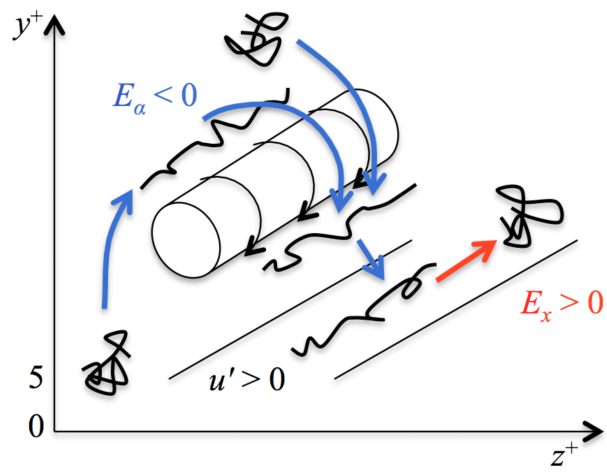

Figure 2: Sketch of the coil-stretch process in the near wall region. Fig. 5 (b) from Dubief et al. [9]

The focus of this paper is to highlight an interesting aspect of the DR which is its complex transient behaviour, sketched in Figure (1). Here the drag reduction is difined as $DR = 1 - f_p/f_0$, where f_p and f_0 is respectively the polymeric and the solvent friction factor. Such a transient behaviour is mainly concerned with two mechanisms: (a) the development of the turbulent structures after the polymer injection in a tube (non-homegeous drag reducing flow) or after the flow startup in a homogeneous drag reducing flow; (b) the polymer degradation or de-aggregation. Over time, at the very beginning of the phenomenon, when the polymer is injected in a tube or a rotating apparatus is started up, the DR exhibits negative values, before reaching its maximum efficiency at DR_{max}. It seems that the maximum efficiency is reached when a sufficient number of molecules in a coil-stretch cycle are in a state of equilibrium with the turbulent structures. The time to achieve DR_{max} is referred to here as the developing time, denoted t_d. The increasing friction factor at the beginning of the process is bacause the coiled polymers extract energy from the mean flow to start their coil-stretching process. It looks like an instantaneous increment of the local extensional viscosity after a high polymer stretching (see [10], [11]). Figure (2) (Fig. 5 (b) from [9]) shows a sketch of such a coil-stretching process in a region near a wall. After an analysis of a turbulent flow of a FENE-P fluid in a channel, the authors sketchet out a polymer cycle near the wall. The polymers, partially extended by the mean flow, is stretched by the vortexs before to coil again in a region of low turbulent intencity (see Dubief et al. [9] for details). Following t_d, we observe a constant value of DR for a period of time, which is denoted by t_r, the resistance time. Finally, after this period, DR begins to fall, reaching a minimum level after a long enough time, when the degradation process has reached its steady state and DR assumes an asymptotic value, DR_{asy}. In other words the polymer scission stops and the molecular weight distribution reaches a steady state.

In the next two sections it is shown some previous results which take into account the drag increase and the degradation. The results were obtained using a cilindrical double gap device wich is described in Pereira and Soares [12].

2 The Drag Increase at the Very Start of the Test

An aspect quite interesting of the DR is the drag increase which appears at the flow startup, which is the case of a homogenuos flow in rotating apparatus for example, or after the polymer injection in a flow through straight tubes for example. In fact, a drag increase in drag reducing flows seems, at a first view, paradoxical. Despite to this fact, it really occurs. By aid of direct numerical simulations of a FENE-P fluid, Dimitropoulos et al. [10] show DR over time when its negative values are cleary brought to light at the very start of the phenomenon. The suggested explanation, which is in aggrement with Tamano et al. [11], is related with the necessary energy which is required by the polymers to be stretched in the beggining of the coil-stretch process. Up to now, experimental data for drag increase are scarce. Tiederman et al. [13] observed the drag increase when drag-reducers were directly injected in the near wall of a turbulent channel flow of water.

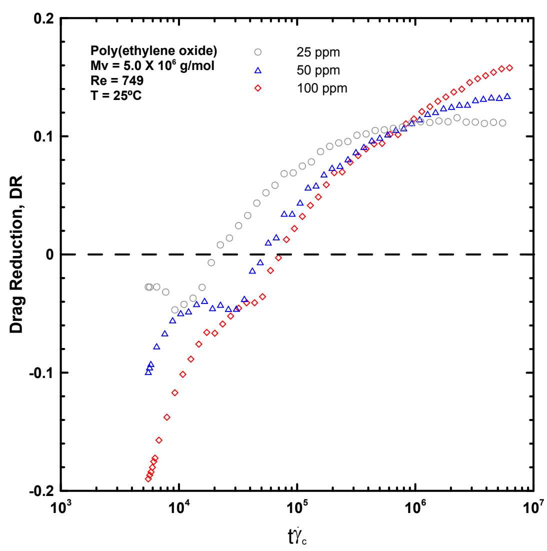

Figure 3: Effect of concentration, c, on DR as a function of the dimensionless time $t\dot{\gamma}_c$ for PEO solutions. Fig. 4 from Andrade et al. [14]

It is rather difficult to observe negative values of DR, since the phenomenon only occurs in the first few seconds of the process. In Figure (3) and Figure (4) are shown the DR over time from the very beginning of the test until the maximum of drag reduction is achieved. In other words, the tests are conducted over the developing

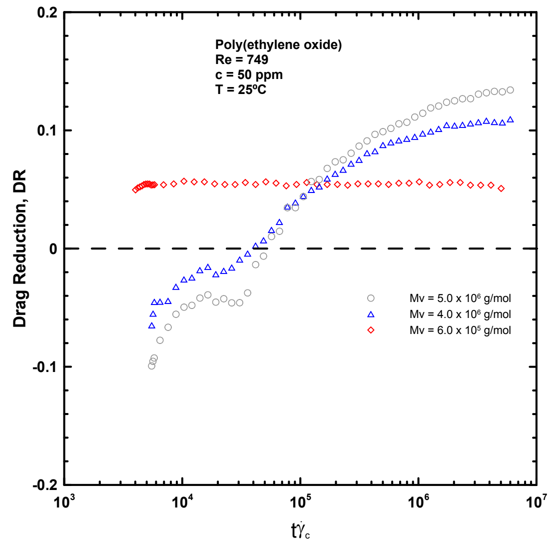

Figure 4: Effect of molecular weight, Mv, on DR as a function of the dimensionless time $t\dot{\gamma}_c$ for PEO solutions. Fig. 5 from Andrade et al. [14]

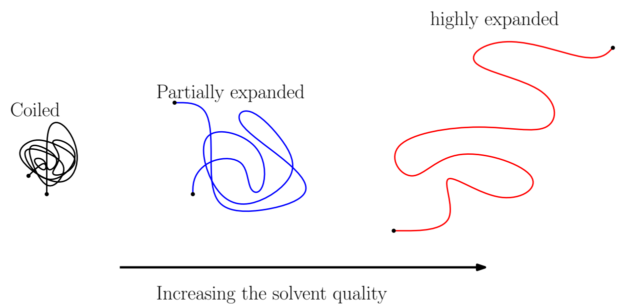

Figure 5: Linear molecule conformation

time, t_d. DR_{max} is not reached instantaneously because the turbulent structures take time to achieve their steady state after the initial disturbance caused by the polymers (for detailes see [10]). Figure (3) shows the role that the concentration plays on DR. Clearly, the solution of 100 ppm of PEO exibits the smallest value of DR (around -0.2) at the test startup, which is in a good aggrement with the idea that the polymers take energy from the mean flow to stretch, causing a drag increasing. Hence, a more concentrated solution demands more energy from the mean flow and the drag increase is more pronounced. The developing time also increases with the concentration. The level of disturbance is higher at more concentrated solutions and, consequently, the turbulent structures development time increases. As widely reported, the DR_{max} is an increasing function of the concentration. In Figure (4) the effect of the molecular weight is shown. The negative value of DR is more pronounced for polymers with large molecular weight. It is worth noting that in the PEO solution with $M_v = 6 \times 10^5$ the drag increase disapeared and the developing time was almost instantaneous. Andrade et al. [14] give some evidences that the drag increase is strongly related to the polymer conformation in the solution before the test beginning. They argue that as coiled is the molecules before the test as more energy is required to stretch them and, in consequence, the drag increase is favored. Many

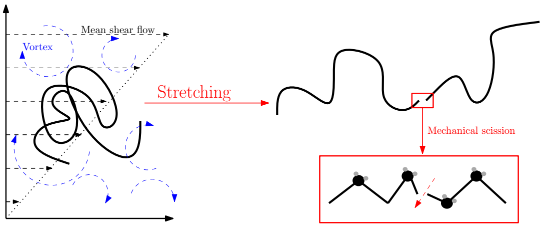

Figure 6: Enter the caption for your figure here. Create a figures directory and place all figures in that directory

other results are shown by the authors to sustain such a idea. In Figure (5) is depicted trhee different possibility for the conformation of linear polymers depending of the solvent quatity. The highly expanded configuration is the most efficient for DR applications. **Certaly, the drag increase is not a crutial problem for practical applications, since it occurs only at the first seconds of the process. However, we must pay much attention in this phenomenon to improve our knowledge on the mechanism of drag reduction. Obviously, despite to the fact that the drag increases at the test startup when the concentration and molecular weight is increased, the DR_{max} also increases. Hence, from the practical point of view, it is generally desirable to use more concentrated solutions and polymers with larger molecular weights.**

3 The Molecule Degradation

A crucial aspect of the DR which turns the development of new drag reducers a task not ease is the mechanical polymers scission by the turbulent flow. The decreasing of the drag reduction from DR_{max} to DR_{asy} sketched in Figure (1) is mainly caused by the polymer degradation. Sometimes the loss of efficiency is also caused by the molecus de-aggregation, which is a different phenomenon. The polymer mechanical scission is sketched in **??**. The polymer is initially partially stretched by the mean flow and them interact with the turbulent structures when they can be totally extended and eventually breaks down. When a great number of macro-molecules experince the scission the mean molecular weight of the solution decreases and, as a consequence, the DR efficiency goes down. The breakage process does not occurs indefinitely. In fact, after a time long enough over the action of the turbulent flow, a steady state mean molecular weight is reached and the DR reaches its final value, an asymptotic value, DR_{asy}.

In Figure (7) (from Pereira et al. [8]) in displaced the DR over time for three different linear polymers (PEO, PAM and XG) for a range of concentrations. For all kind of polymers analysed by the authors, DR is clearly an increasing function of the concentration, as widely known. It is worth noting that the solution of 100 ppm of PAM does not degrades at al for the stablished conditions. Another way to look for the same data is with respect to the relative drag reduction, defined as $DR' = DR(t)/DR_{max}$, which is depicted in Figure (8). This paremeter measures directly the loss of efficiency of DR over the time. The DR'_{asy} for the solution of 100 ppm of PEO is around 0.5 which means that such a solution loses 50% of efficiency over process. The same concentration of PAM loses nothing. Its value of DR' is a constant igual 1. What is not obvious, but It can be concluded

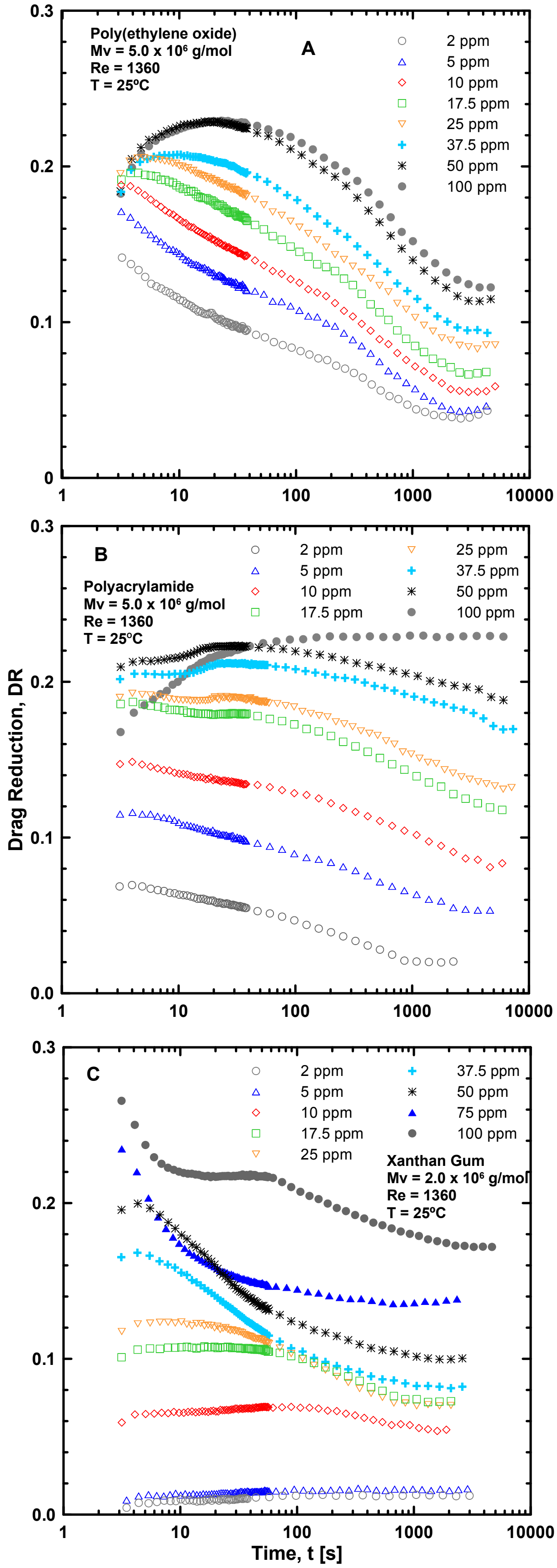

Figure 7: Effect of concentration on DR as a function of time. The measurements were carried out for PEO, PAM and XG. Fig. 9 from Pereira et al. [8]

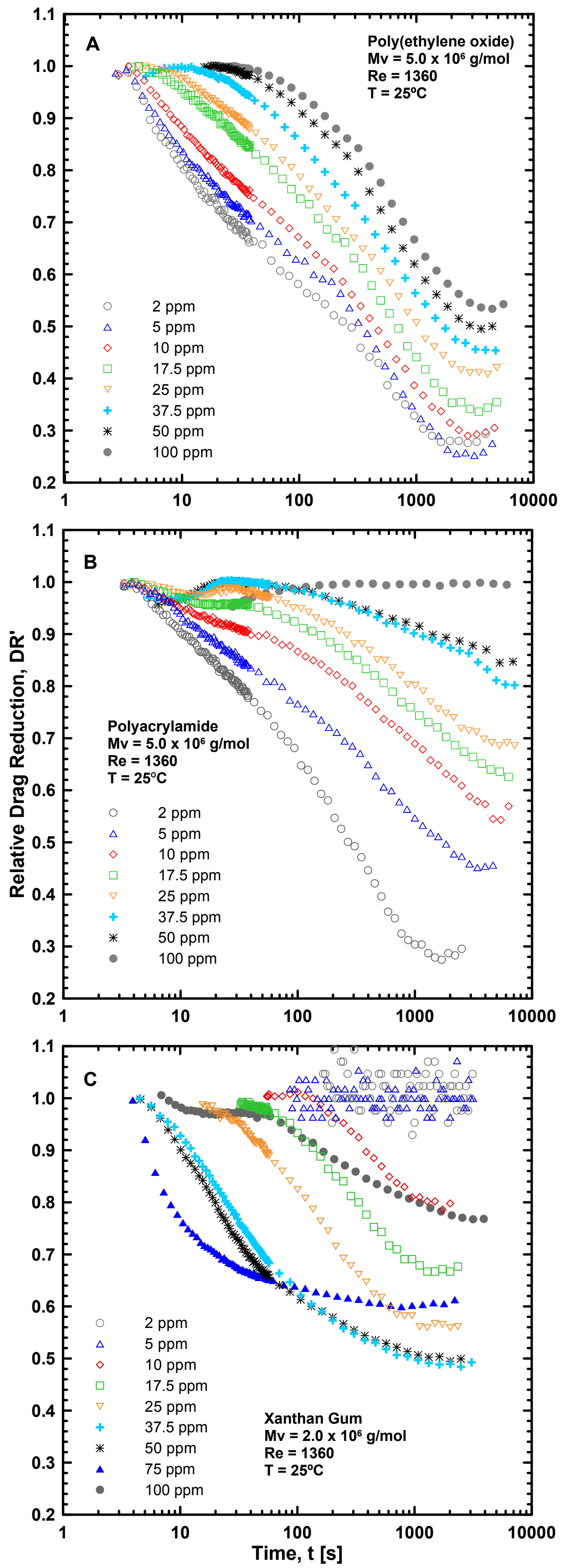

Figure 8: Effect of concentration on DR as a function of time. The measurements were carried out for PEO, PAM and XG. Fig. 16 from Pereira et al. [8]

from Figure (8) is the fact that an increasing concentration, in general, turns the solution more resistant. In others words, beyond an increase of the values of DR with increments of concentration, the degradation process is also reduced. It is not totally clear for XG which exibts a complex dependence with the concentration. A deeper discussion about this issue including analysis of other variables is in Pereira and Soresl [12], Pereira et al. [8] and in Andrade et al.[14].

Acknowledgment

This research was partially funded by grants from CNPq (Brazilian Research Council), ANP (Brazilian Petroleum Agency) and Petrobras.

References

[1] B. A. Toms, “Some observations on the flow of linear polymer solutions through straight tubes at large reynolds numbers,” *Proceedings of the International Congress of Rheology, Holland, North-Holland, Amsterdam, Section II*, pp. 135–141, 1948.

[2] E. D. Burger and L. G. Chorn, “Studies of drag reduction conducted over a broad range of pipeline conditions when flowing prudhoe bay crude oil,” *J. Rheology*, vol. 24, p. 603, 1980.

[3] H. L. Greene, R. F. Mostardi, and R. F. Nokes, “Effects of drag reducing polymers on initiation of atherosclerosis,” *Polym Engng Sci*, pp. 20–449, 1980.

[4] A. G. Fabula, “Fire-fighting benefits of polymeric friction reduction,” *Trans ASME J Basic Engng*, pp. 93–453, 1971.

[5] J. L. Lumley, “Drag reduction by additives,” *Annual Review of Fluid Mechanics*, vol. 11, pp. 367–384, 1969.

[6] P. S. Virk, “Drag reduction fundamentals,” *AIChE Journal*, vol. 21, pp. 625–656, 1975.

[7] M. Tabor and P. G. de Gennes, “A cascade theory of drag reduction,” *Europhysics Letter*, vol. 7, pp. 519–522, 1986.

[8] A. S. Pereira, R. M. Andrade, and E. J. Soares, “Drag reduction induced by flexible and rigid molecules in a turbulent flow into a rotating cylindrical double gap device: Comparison between poly (ethylene oxide), polyacrylamide, and xanthan gum,” *J. Non-Newt. Fluid Mech.*, vol. 202, pp. 72–87, 2013.

[9] Y. Dubief, C. M. White, V. E. Terrapon, E. S. G. Shaqfeh, P. Moin, and S. K. Lele, “On the coherent drag-reducing and turbulence-enhancing behaviour of polymers in wall flows,” *J. Fluid Mech*, vol. 514, pp. 271–280, 2004.

[10] C. D. Dimitropoulos, Y. Dubief, E. S. G. Shaqfeh, P. Moin, and S. K. Lele, “Direct numerical simulation of polymer-induced drag reduction in turbulent boundary layer flow,” *Physics of Fluids*, vol. 17, pp. 1–4, 2005.

[11] S. Tamano, M. Graham, and Y. Morinishi, “Streamwise variation of turbulent dynamics in boundary layer flow of drag-reducing fluid„” *J. Non-Newt. Fluid Mech.*, vol. 504, pp. 61–71, 2011.

[12] A. S. Pereira and E. J. Soares, “Polymer degradation of dilute solutions in turbulent drag reducing flows in a cylindrical double gap rheometer device,” *Journal of Non-Newtonian Fluid Mechanics*, vol. 179, pp. 9–22, 2012.

[13] W. Tiederman, T. Luchik, and D. Bogard, “Wall-layer structure and drag reduction,” *J. Fluid Mech*, vol. 156, pp. 419–437, 1985.

[14] R. M. Andrade, A. S. Pereira, and E. J. Soares, “Drag increase at the very start of drag reducing flows in a rotating cylindrical double gap device,” *Journal of Non-Newtonian Fluid Mechanics*, vol. 212, pp. 73–79, 2014.

Some Features of the Flow on Cylinders in Aerodynamic Channels and Considerations About the Effect of the Blockage Ratio Part 1: Single Cylinder

S.V. Möller[1], R.S. Silveira[1], A.V. de Paula[1], M.L.S. Indrusiak[2] and C.R. Olinto[3]

[1] *UFRGS - Universidade Federal do Rio Grande do Sul, Rua Sarmento Leite, 425, 90050-170 Porto Alegre, RS, Brazil*

[2] *UNISINOS - Universidade do Vale do Rio dos Sinos, Av. Unisinos, 950, 93022-000 - Sao Leopoldo, RS, Brazil*

[3] *FURG - Universidade Federal de Rio Grande, 96203-900 - Rio Grande, RS, Brazil*

Abstract

This paper presents experimental results from hot wire measurements in the wake of cylinders in an aerodynamic channel focusing on the vortex shedding process. Attention is given on the effect of blockage ratio on the vortex shedding. Analysis is made by means of Fourier and wavelet transforms. Results of vortex shedding show that the shedding frequency is not constant along time. A comparison with a prism indicates distinct behaviors in both cases. A correlation for Strouhal number as a blockage ratio function is presented.

1 Introduction

The phenomena of flow around cylinders are present in nature, by the effect of wind on palms and trees, and on a large group of engineering applications such as chimneys, towers, electricity transmission lines, shell and tube heat exchangers, among others. The behavior of such phenomena has direct influence in project development, particularly as regards the behavior of vortex shedding and fluid-structure interaction. In the study in laboratory conditions, one of the parameters involved in this kind of study is the blockage ratio, which influences the shedding frequency, usually presented in form of the Strouhal number, given by

$$S = \frac{f_s d}{U} \tag{1}$$

where f_s is the frequency vortex shedding, d is the cylinder diameter and U the free stream velocity, [1]. The Strouhal number is usually presented as a function of the Reynolds number, in a certain range. The Strouhal number for a smooth circular cylinder is considered constant, S = 0.21, for the flow in a subcritical regime [1].

In 1878, Čeněk (Vincenc) Strouhal published the first article relating frequency (of aeolian tones) and velocity of the flow over a bluff body [2]. Since 1908, with the works performed by H. Bénard [3] [4], studies of vortex shedding are found in the literature, with focus on the behavior of the wake of a single cylinder (e.g. [5], [6]) or groups with two or more cylinders (e.g. [7]; [8]), or even attempts to suppress or control vortex shedding (e.g. [9]). However, geometric factors associated to the aerodynamic channel or wind tunnel employed, like the blockage ratio, may have influences on the Strouhal number.

In the study of the blockage effect of the flow past a single circular cylinder in an aerodynamic channel, the blockage ratio is given by d/L, where "d" is the diameter of the cylinder and "L" the channel width. Maskell [10] proposes a method for analyzing the blockage effects of wind tunnel for bluff bodies based on the balance of momentum and the idea that the increase in the wall effects on the tunnel leads to a simple increase in the velocity of the undisturbed flow.

Works like that of [11], which involves the blockage effect on the flow around circular cylinders, with blockage ratios between 6 and 16%, demonstrate the presence of changes in pressure distribution and increase of the Strouhal number, for a range of Reynolds number between 104 and 105. Anagnostopoulos et al. [12] conducted a numerical study of the blockage effect on circular cylinders in permanent and transient flows with Re = 106 and ratios of 5%, 15% and 25%. They showed that the hydrodynamic forces on the cylinder and Strouhal number increase with the blockage ratio increasing.

A classification of blockage effects of the flow in circular cylinders was made by [13]:

d/L < 10%
: Blockage effect is small and can be ignored;

10% < d/L < 60%
: Blockage changes the flow, corrections in the measured data is necessary;

d/L > 60%
: Blockage radically alters the flow around the cylinder, and corrections in the data make no sense.

Turki et al. [14] showed a numerical study about the blockage effect in a channel with laminar flow around rectangular cylinders. The Reynolds number is between 62 and 300 and the blockage ratios are 12.5%, 16.7% and 25%. The results show the increase of Strouhal number with the blockage ratio.

Indrusiak and Möller [6] performed measurements in the wake behind a cylinder submitted to accelerating impinging flow. The results are complementary to those of [10] showing that, for blockage ratio of 16.5% and $Re \leq 2.5 \times 104$, the Strouhal numbers are strongly affected by the deviation of the flow around the cylinder and experience an increment of up to 57% at lower Reynolds numbers.

In experimental turbulence study, turbulence is considered a random phenomenon, studied by means of

Fourier spectral analysis for stationary flows, and through wavelet analysis for both stationary and non-stationary flows. Usually, random data are presented in form of discrete time series.

The purpose of this paper is to present the study of the wake behind single cylinders in an aerodynamic channel with considerations on the effect of blockage ratio on the Strouhal number.

2 Background: Fourier and Wavelet Analyses

The Fourier transform of a discrete time series representing a finite function x(t) enables the study of spectral behavior of the random phenomenon from the series given by

$$\hat{x}(f) = \frac{1}{2\pi} \sum x(t) e^{-ift} \tag{2}$$

Thus, the Fourier spectrum gives the energy distribution of the signal in the frequency domain evaluated over the entire time interval. The Fourier spectrum is defined as:

$$P_{xx}(f) = |\hat{x}(f)|^2 \tag{3}$$

which is used to determine power spectral density.

Wavelet analysis enables the treatment of transient series and is based on the idea of stretching and compressing the window of the windowed Fourier transform, according to the frequencies to be localized, allowing the definition of the scales of interest in time and frequency domains. The bases of wavelet transform are generated through dilations and translations of a single wavelet function, $\psi(t)$ with finite energy and zero average and are used for stationary and non-stationary signal analysis [15].

Let the function $\psi_{a,b}(t)$ be the wavelets basis. The continuous wavelet transform (CWT) of a function $x(t)$ is given by:

$$\tilde{X}(a,b) = \int_{-\infty}^{\infty} x(t)\psi_{a,b}(t)dt \qquad a,b \quad \in \quad \Re \tag{4}$$

The scale and position parameters a and b are related to the frequency and time of the analyzed function. The wavelet spectrum associated is the matrix of the squared wavelets coefficients, given by,

$$P_{xx}(a,b) = |\tilde{X}(a,b)|^2 \tag{5}$$

The wavelet spectrum, or spectrogram, provides the energy associated to each time and scale (or frequency), allowing the representation of the distribution of the energy of the transient signal over time-frequency domains [16].

The continuous wavelet spectrum gives a general view of the distribution of a signal over time and scale and is able to emphasize the signal singularities. The CWT is very useful to pick out some features of the signal and the discrete wavelet transform (DWT) arises like a sub sampling of the CWT with dyadic scales, with no loss of information. The DWT is given by

$$\tilde{X}(j,k) = \sum_t x(t)\psi_{j,k}(t) \qquad a,b \quad \in \quad Z \tag{6}$$

where (j,k) are the dyadic scale and position coefficients.

The number of levels of the transformations which can be calculated is limited by the length of the time series. Unlike the Fourier transform, in the wavelets transform the remaining coefficients are related to the lower frequencies, including the mean value of the signal, and cannot be disregarded. Therefore, the DWT of a series with more than 2^j elements is computed for $1 \leq j \leq J$, where J is a conveniently arbitrary choice, and the remaining information, corresponding to mean values, for a scale J is

$$\tilde{X}(J,k) = \sum_t x(t)\phi_{J,k}(t) \tag{7}$$

where $\phi(t)$ is the scaling function associated to the wavelet function. Thus, the representation of any discrete time series is given by,

$$x(t) = \sum_k \tilde{X}(J,k)\phi_{J,k}(t) + \sum_{j\leq J}\sum_k \tilde{X}(j,k)\psi_{j,k}(t) \tag{8}$$

where the first term is the approximation of the signal at the scale J, and the inner summation of the second term are details of the signal at the scales $j(1 \leq jleqJ)$.

The discrete wavelet packet transform (DWPT) is a modification of the pyramid algorithm, where the DWT is computed [17]. Each detail series is wavelet transformed in two series, with respectively lower and upper half bandwidth frequency interval. The DWPT basically is a modification of the DWT, in order to obtain the decomposition of the signal in successive intervals of equal bandwidth and is done by

$$\tilde{X}(j,m,k) = \sum_k x(t)\psi_{j,m,k}(t) \tag{9}$$

In this paper, Db20 wavelet and level $9 (J = 9)$ were used, the resulting frequency bandwidth is 2.93 Hz. A more detailed discussion of wavelet analysis is done in [6].

3 Experimental Technique

Velocity measurements were made with DANTEC StreamLine hot wire anemometer in an aerodynamic channel. The test apparatus, shown schematically in Fig. 1, is a $1370mm$ long rectangular channel, with $146mm$ height and a width of $193mm$. Air, at room temperature, is the working fluid, driven by a centrifugal blower, passed by a diffuser and a set of honeycombs and screens, before reaching the measurement location with about 1% turbulence intensity. Blower speed is controlled by a frequency inverter allowing the flow velocity in the aerodynamic channel to be varied from zero to $15m/s$. Reference velocity was measured by a Pitot tube placed after the screens. The reference velocity is approximately the free stream velocity.

In the experiment with a single cylinder, the reference velocity was 5, 10 and $15m/s$. The cylinder was positioned between 220 to $320mm$ from the end of the channel. The incidence angle of the flow on the cylinder is 90°. For the measurement of velocity and velocity fluctuations, a single hot wire probe was placed at the wake region in a downstream distance "x" variable according to the cylinder diameter studied, Fig. 1(b).

Data acquisition was performed with a 16-bit A/D-board (NATIONAL INSTRUMENTS 9215-A) with USB interface, at a sampling frequency of $3000Hz$ and a low pass filter at $1000Hz$. Measurements were performed at constant velocity. The error of the determination of the velocity fluctuations with a hot wire is between 3 and 6%. The experimental data were analyzed by statistical, spectral, wavelet tools using the MatLab© software.

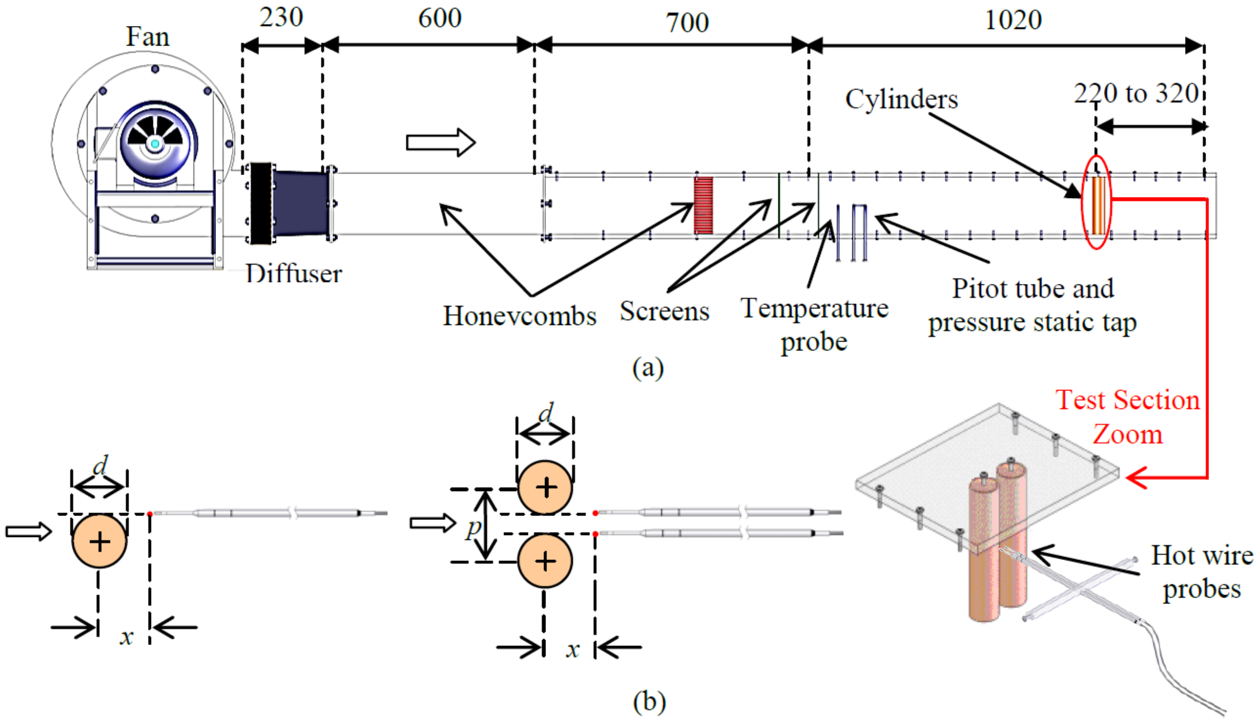

Figure 1: Schematic view of (a) the aerodynamic channel, (b) probe position

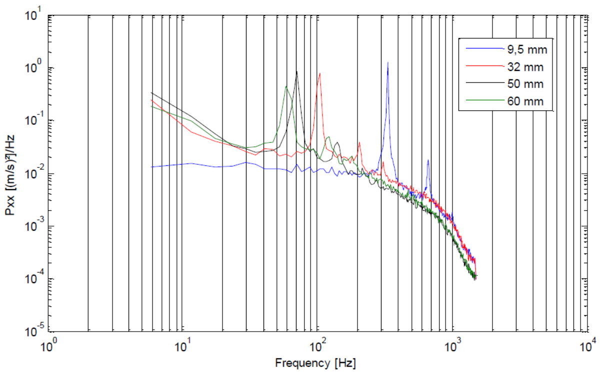

Figure 2: Fourier Spectrum for cylinder diameters of $9.5mm$, $32mm$, $50mm$ and $60mm$, with Reynolds numbers of 8910, 29941, 46637 and 55693, respectively

4 Results

Figure 2 shows the Fourier spectra for the cylinders with diameters of $9.5mm$, $32mm$, $50mm$ and $60mm$, at a free stream velocity of $15m/s$. Vortex shedding frequency are respectively $333.9Hz$, $105.5Hz$, $70.3Hz$ e $60.6Hz$, each value corresponding to a Strouhal number 0.213, 0.228, 0.242 e 0.251. It is observed in all spectra shown in Figure 2, the peak of vortex shedding frequency and, at at least its first harmonic, observed even with the increase of the blockage ratio. The presence of these harmonics is still unclear but is an inherent feature of separated flows. According to nonlinear hydrodynamic stability theory and experimental findings, higher harmonics are generated when the amplitude of the fundamental component exceeds about 4% of the mean flow [18].

Figure 3 (a), (b), (c) and (d) presents the spectrograms of the measured signals calculated using the continuous wavelet transform, which allows analyzing the behavior

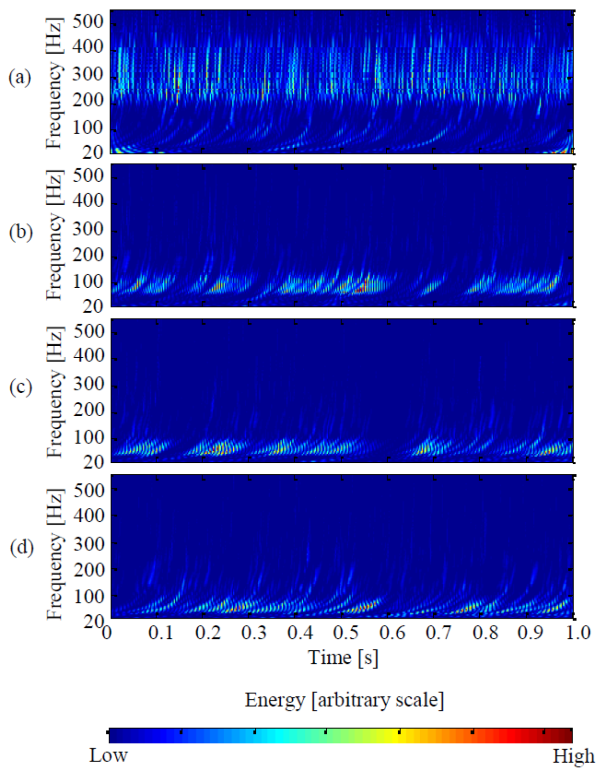

Figure 3: Spectrograms of the wake for: (a) cylinder diameter of $9.5mm$ (4.92% of blockage), (b) cylinder diameter of $32mm$ (16.58% of blockage), (c) cylinder diameter of $50mm$ (25.91% of blockage) and (d) cylinder diameter of $60mm$ (31.09% of blockage)

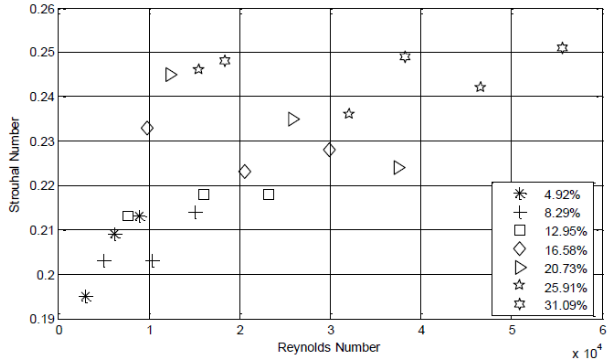

Figure 4: Strouhal number as a function of the Reynolds number for all blockage ratios studied

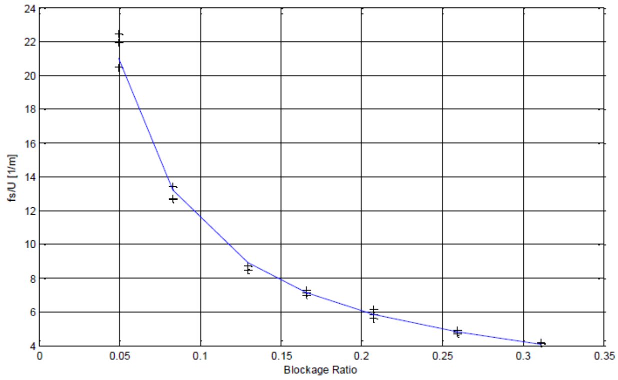

Figure 5: f_s/U ratio as a function of the blockage ratio d/L

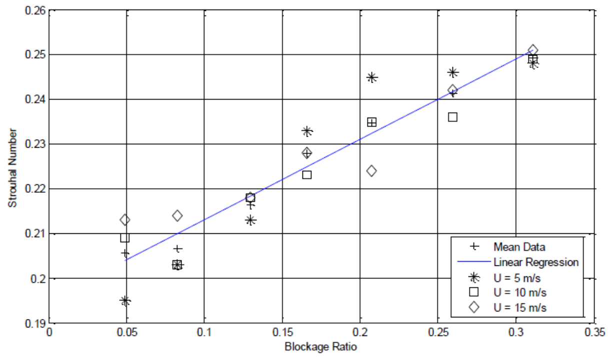

Figure 6: Strouhal number as a function of the blockage ratio for the mean velocities 5, 10 and $15m/s$

of vortex shedding frequency over time for the same conditions of the Fourier spectra of Fig. 2. The behavior of the shedding frequency with time can be observed as energy bands according with the diameter of the cylinders leading to different scales of energy and frequency.

For all observed results the shedding frequency is not constant, rather it wanders around the value of the peak frequency in spectra [6]. For the same incident velocity, as the cylinder diameter increases, the shedding frequency is reduced accompanied by the broadening of the corresponding peak. In general, the tendency of increasing the Strouhal number with the blockage ratio and the Reynolds number is observed, although, by plotting Strouhal versus Reynolds number, no apparent correlation is observed as shown in Fig. 4.

Nevertheless, a careful examination of Fig. 4 shows two different behaviors, namely, for blockage ratios up to 12.95% the results are in accordance with [19], wherein the Strouhal number decreases for low Reynolds numbers and lower blockage ratio. For larger blockage ratios the Strouhal number has a tendency of increasing as the Reynolds number is reduced. This is in accordance with the results by [6] for a 16.5% blockage ratio, where for Reynolds numbers lower than 1.8×10^4, strong increase of the Strouhal numbers at lower Reynolds numbers is observed.

However, by plotting the shedding frequency divided by the incident velocity (f_s/U) as function of the blockage ratio, Fig. 5, the experimental results for all Reynolds numbers can be represented as an exponential distribution

$$\frac{f_s}{U} = 1.448 \left(\frac{d}{L}\right)^{-0.888} \tag{10}$$

with a value of the regression coefficient $r^2 = 0.9966$.

This result indicates that, at least in the Reynolds number range investigated, the Strouhal number can be described as function of the blockage ratio. Linear regression of the data in Fig. 6 gives a linear variation of the Strouhal number (S) with the blockage ratio (d/L) according to

$$S \cong 0.179\frac{d}{L} + 0.195 \tag{11}$$

Equation 11 is an approximation that allows analyzing the behavior of the Strouhal number with the blockage ratio in the range of Reynolds numbers of this work. The regression coefficient of this fit is $r^2 = 0.9789$, providing a good accuracy with this relationship within the range of study of this paper. According to [13], blockage ratios between 10 and 60% modify the flow. This range is analyzed in this study, with the exception of cylinder diameters of 9.5 and $15mm$, corresponding to a blockage ratio lower than 10%. Therefore, the increase of blockage ratio leads to an increase of Strouhal number. A tentative explanation for this fact is the interaction between vortex formation and channel wall. The reduction in the gap size between the tube and the wall increases the velocity of flow crossing the tube and the shedding frequency.

Comparison Between a Cylinder and a Prism

Figures 7(a) and 7(b) show the Fourier spectra of the wake velocity fluctuations for the circular cylinder with $32mm$ in diameter and Reynolds number equal to 3.4×10^4, and for the rectangular prism and Reynolds number equal to 9.8×10^3, respectively. The velocities were measured in the wake downstream the bluff bodies. The Fourier spectra were smoothed using a frequency band of $1.9Hz$. In both figures, the higher peaks denote the shedding frequency.

For the rectangular prism there are other two peaks corresponding to approximately the shedding frequency harmonics of $300Hz$ and $480Hz$. These results, calculated as the previous cases, agree with the results found in the fluid mechanics literature. Figures 8(a) and 8(b) present the wavelet spectra or spectrogram of the same signals. The wake energy seems much more regular downstream the prism than the cylinder. This is in accordance with the Fourier spectra, where the energy of the wake, computed for the whole time interval, is about ten times higher for the prism than for the cylinder [20].

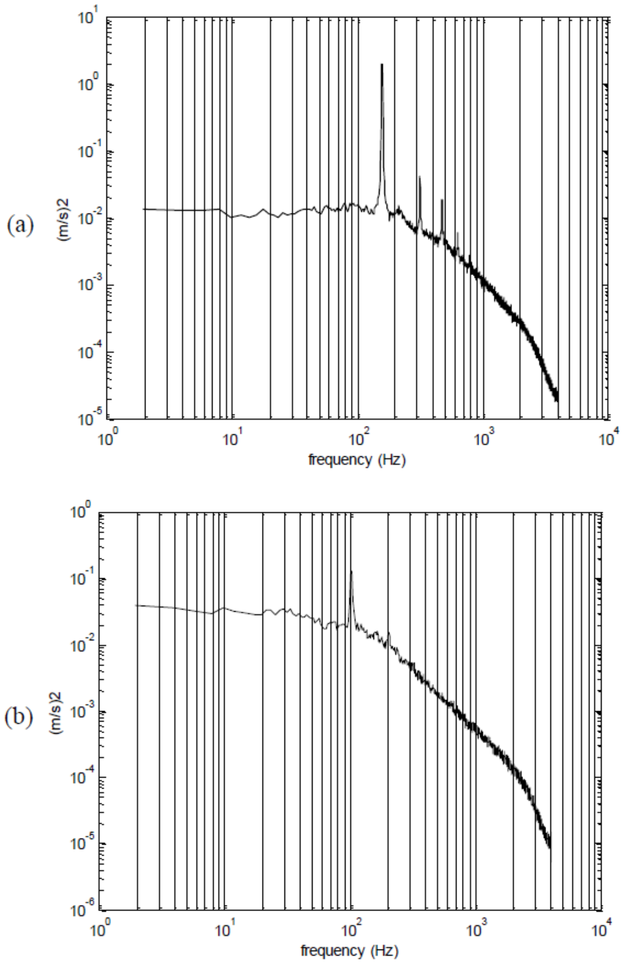

Figure 7: Fourier Spectrum for: (a) cylinder diameter $32mm$, $d/L = 0.165$; (b) prism with width $9.5mm$, $d/L = 4.97$

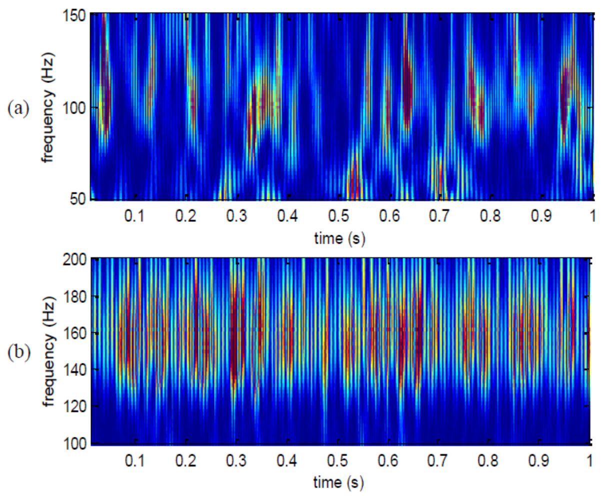

Figure 8: Wavelet spectra for: (a) cylinder diameter $32mm$, $d/L = 0.165$; (b) prism with width $9.5mm$, $d/L = 4.97$

5 Conclusions

This paper presents a study on experiments performed on a cylinder subjected to turbulent flow. The effect of blockage ratio on the Strouhal number was studied. In this work, the blockage ratio was varied through the diameter of the cylinders. Measurements of the velocity fluctuations in the aerodynamic channel were made using the hot wire anemometry technique. The experiments were performed in the subcritical regime.

It was observed an increase in the Strouhal number in the range of Reynolds number studied. High blockage ratios increased the Strouhal number, due to the increased diameter of the cylinders, causing the vortex shedding frequency to decrease. The increase in the diameter of the cylinder was such that compensated the decrease in the vortex shedding frequency and still increased the Strouhal number. An expression for the prediction of the Strouhal number as a function of the blockage ratio was proposed. In the velocity range examined, 5, 10 and $15m/s$, a decrease in the Strouhal number for low blockage ratios and high Reynolds numbers was observed, as already predicted by [19].

Acknowledgements

S.V. Möller is gratefully indebted to the CNPq - National Council for Scientific and Technological Development, Ministry for Science, Technology and Innovation, Brazil, for the continuing financial support (BPP).

References

[1] Blevins, R.D., 1990, Flow Induced Vibrations, van Nostrand-Reinhold, New York.

[2] Strouhal, V., 1878, "Über eine besondere Art der Tonerregung", Ann. Phys. und Chemie, New Series v. 5, p. 216-251.

[3] Bénard, H, 1908-a, "Formation périodique de centres de giration á l'arriére d'un obstacle en mouvement", C. R. Acad. Sci., 147, pp. 839-842.

[4] Bénard, H., 1908-b, "Etude cinématographique des ramous et des rides produits par la translation d'un obstacle", C. R. Acad. Sci., 147, pp. 970-972.

[5] Lin, C. and Hsieh, S. C., 2003, "Convection velocity of vortex structures in the near wake of a circular cylinder", Journal of Engineering Mechanics-ASCE, v. 129 pp. 1108-1118.

[6] Indrusiak, M.L.S. and Möller, S.V., 2011, "Wavelet Analysis of Unsteady Flows: Application on the Determination of the Strouhal Number of the Transient Wake Behind a Single Cylinder", Experimental Thermal Fluid Science, v. 35, pp. 319-327.

[7] de Paula, A.V and Möller, S.V., 2013, "Finite mixture model applied in the analysis of a turbulent bistable flow on two parallel circular cylinders", Nuclear Engineering and Design v. 264 pp. 203âĂŞ 213.

[8] Yang, Y., Aydin, B.T. and Ekmekci, A., 2014, "Flow Past Two Cylinders in Tandem: Vibration Effect", Journal of Fluids and Structures, v. 44, pp. 292-309

[9] Ekmekci, A. and Rockwell, D., 2010, "Effects of a Geometrical Surface Disturbance on Flow past a Circular Cylinder: A Large Scale Spanwise Wire". Journal of Fluid Mechanics, v. 665, pp. 120-157.

[10] Maskell, E.C., 1963, "A Theory of the Blockage Effects on Bluff Bodies and Stalled Wings in a Closed Wind Tunnel", Aeronautical Research Council Reports and Memoranda, no. 3400, London.

[11] West, G. S. and Apelt, C. J., 1982, "The Effect of Tunnel Blockage and Aspect Ratio on the Mean Flow Past a Circular Cylinder with Reynolds Numbers between 104 and 105", Journal of Fluid Mechanics, v.114, pp. 361-377.

[12] Anagnostopoulos, P., Iliadis, G. and Richardson, S., 1996, "Numerical Study of the Blockage Effects on Viscous Flow Past a Circular Cylinder", International Journal for Numerical Methods in Fluids, v. 22, pp.1061-1074.

[13] Zdravkovich, M. M., 2003, Flow Around Circular Cylinders, v. 1-2, Oxford University Press Inc., New York.

[14] Turki, S.; Abbassi, H., Nasrallah, S.B., 2003, "Effect of Blockage Ratio on the Flow in a Channel with a Built-in Square Cylinder", Computional Mechanics, v. 33, p. 22-29.

[15] Percival, D.B. and Walden, A.T., 2000, Wavelet Methods for Time Series Analysis, Cambridge University Press, Cambridge.

[16] Daubechies, I., 1992 Ten Lectures on Wavelets, SIAM - Society for Industrial and Applied Mathematics, Philadelphia.

[17] Mallat, S., 2009, A Wavelet Tour of Signal Processing - The Sparse Way, 3rd ed., Academic Press, Burlington.

[18] Ziada, S. & Oengören, A. 1992, "Vortex Shedding and Acoustic Resonance in an in-line Tube Bundle - Part I: Vorticity Shedding", Journal of Fluids and Structures, Vol. 6, pp. 271-292.

[19] Roshko, A., 1954, "On the Development of Turbulent Wakes from Vortex Streets", National Advisory Committee for Aeronautics, R. 1191, California Institute of Technology, Pasadena, alifornia.

[20] Olinto, C. R., Indrusiak, M. L. S., Möller, S. V., 2005, "Strouhal Number Fluctuations in a Cylinder Wake", Proceedings of COBEM 2005, 18th International Congress of Mechanical Engineering, available in `http://www.abcm.org.br/pt/wp-content/anais/cobem/2005/index.htm`

Some Features of the Flow on Cylinders in Aerodynamic Channels and Considerations About the Effect of the Blockage Ratio
Part 2: Two Cylinders Side-By-Side

S.V. Möller[1], R.S. Silveira[1], A.V. de Paula[1], M.L.S. Indrusiak[2], A. P. Ost[1]

[1] *UFRGS - Universidade Federal do Rio Grande do Sul, Rua Sarmento Leite, 425, 90050-170 Porto Alegre, RS, Brazil*

[2] *UNISINOS - Universidade do Vale do Rio dos Sinos, Av. Unisinos, 950, 93022-000 - São Leopoldo, RS, Brazil*

Abstract

This paper presents experimental results from hot wire measurements in the wake of and pairs of cylinders in an aerodynamic channel focusing on the vortex shedding process and on the bistable phenomenon of two cylinders side-by-side. Attention is given on the effect of blockage ratio on the bistability process. Analysis is made by means of Fourier and wavelet transforms. Flow visualizations in a water channel help to improve the analysis of the studied phenomena. For two cylinders side-by-side, an optimal blockage ratio was identified, where the changes of flow modes in the bistable process are enhanced, showing the influence of the wall distance in the bistable process.

1 Introduction

The phenomena of the flow around cylinders are present in nature, and on a large group of engineering applications with direct influence in project development, particularly as regards the behavior of vortex shedding and fluid-structure interaction. In the study in laboratory conditions, one of the parameters involved in this kind of study is the blockage ratio, which influences the shedding frequency, usually presented in form of the Strouhal number.

According to Sumner et al. [1], the cross steady flow through circular cylinders of same diameter (d) placed side-by-side presents a wake with different modes depending on the distance between the centers of the cylinders (p).

In intermediate spacing ratios ($1.2 \leq p/d \leq 2.2$) the flow forms two wakes behind the cylinders, a wide wake behind one cylinder and a narrow wake behind the other, Figure. 1. The presence of these wakes leads to two dominant vortex shedding frequencies: one related to the narrow wake, and other associated with the wide wake. The flow passing through the narrow gap between the tubes is deviated toward the narrow wake. In the so called bistable phenomenon, according to technical literature, the flow pattern undergoes a change that deviated intermittently, sometimes oriented toward a cylinder, sometimes in the other direction. This switching phenomenon, accompanied or not by bistability, is considered an intrinsic property of the flow and is independent of the Reynolds number being not related to misalignments between the cylinders or any other external influence.

According to Kim and Durbim [2], the transition between two asymmetric states is random, being the time scale between transitions about 10^3 times larger than the period vortex shedding, while for Peschard and Le Gal[3], the behavior is not intrinsic to the flow, but associated with disturbances in the turbulent flow at the entrance.

Guillaume and LaRue [4] define terms that describe each of the three types of bistable behavior, the **quasi-stable behavior**, where the flow does not vary with time and large-scale disturbances can cause changes in the average values of the wakes, but the new values remain the same until another major disturbance is applied; the **spontaneous flopping**, where the average flow observed over time alternate between a high value and a lower one featuring the two modes flow, even if no disturbance is applied; and the **forced flopping**, exchanges that are derived from a large disturbance applied.

Sumner et al. [1] conducted a study of flow around two and three cylinders arranged side-by-side across the flow, for pitch ratios between 1 and 6 and Reynolds number in the range between 500 and 3000. However, in the experiment for two cylinders the bistable phenomenon was not observed, this being attributed to the combined effects of the aspect and blockage ratios, the latter being 13%.

Zhou et al. [5] studied velocity and temperature fields in the wake of two cylinders placed side-by-side with p/d between 1.5 and 3.0. The results were compared with the wake of a single cylinder. The authors attributed the extreme narrowing of the gap, the fact that only one frequency, not two, be measured.

For Alam et al. [6], the flow around two circular cylinders of equal diameter, arranged side-by-side showed that the wake has different flow modes. Authors found that the flow switched spontaneously from one side to the other, but they could identify another short duration stable flow pattern. Reference [7]

Refere analyzed the flow around two cylinders placed side-by-side in cross-flow, for small pitch ratios ($1.1 \leq p/d \leq 1.2$), with a Reynolds number of 4.7×10^4. The authors identified four distinct flow modes.

In [8], Authors studied the bistable phenomenon on two cylinders arranged side-by-side in an aerodynamic channel, with $Re = 3 \times 10^4$ and blockage ratio 33%. Authors found the strong presence of bistability in measurements near to the tubes. For a larger distance, bistability was not identified.

More recently, de Paula and Möller [9] presented a finite mixture study of bistability for two cylinders placed

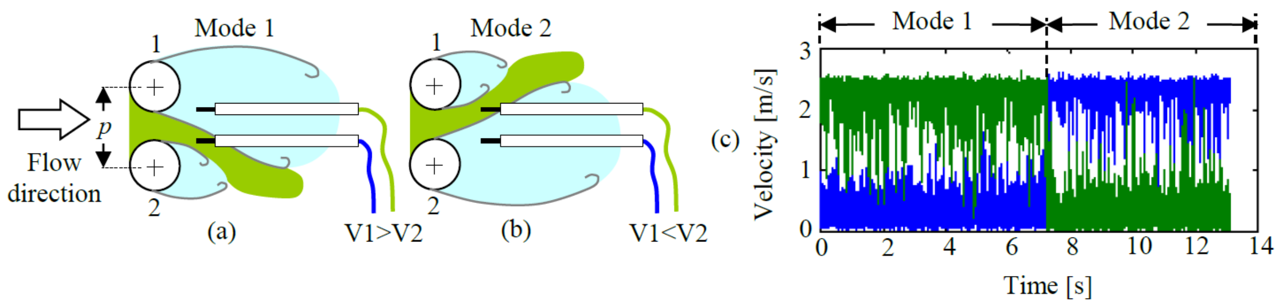

Figure 1: Bistability scheme for two cylinders placed side-by-side: (a) mode 1, (b) mode 2, and their respective characteristic hot wire anemometry signals (c)

side by side. Experimental signals from hot wires were used as input data for the determination of PDF functions. By means of a double well energy model, Authors suggest the existence of more than two flow modes, with no evident time correlation between the changes.

The purpose of this paper is to present the study of the wake behind groups of cylinders in an aerodynamic channel with considerations on the effect of blockage ratio on the phenomenon of bistability on two or more cylinders.

Background: Fourier and Wavelet Analyses

In the present work, Fourier and wavelet transforms and spectra were used in the analyses. A concise mathematical description of the transforms was presented in the first part of the present study.

2 Experimental Technique

Velocity measurements were made with DANTEC StreamLine hot wire anemometer in an aerodynamic channel. The test apparatus is the same used in the first part of the study. The cylinders were positioned between 220 to 320mm from the end of the channel. The incidence angle of the flow on the cylinders is 90°. The reference velocity was 15m/s. For the measurement of velocity and velocity fluctuations, two single hot wire probes are positioned where the distance "x" of the probes to the cylinders is variable according to diameter of the tube examined. Data acquisition was performed with a 16-bit A/D-board (NATIONAL INSTRUMENTS 9215-A) with USB interface, at a sampling frequency of 3000Hz and a low pass filter at 1000Hz. Measurements were performed at constant velocity.

The experimental data were analyzed by statistical, spectral, wavelet tools using the MatLab© software. The error of the determination of the velocity fluctuations with a hot wire is between 3 and 6%.

3 Results

The flow on two cylinders side-by-side with pitch-to-diameter ratios $p/d = 1.26$ was investigated. The chosen diameters ranging between 4.5 and 60mm. In this configuration, the blockage ratio on the channel varies between 4.66 and 62.18%, as shown in Table 1. The Reynolds number on the aerodynamic channel varies from 3.72×10^3 to 7.61×10^4. These values are based on the average velocity of undisturbed flow (characteristic velocity) and the cylinder diameter [10].

Bistable phenomenon was not identified for cylinders with diameters of 4.5, 9.1 and 15mm. For cylinders of 4.5mm in diameter, since each probe has a length of 1mm, the probe size has the magnitude of the wake, making difficult the detection of the phenomenon. For cylinder diameters of 9.1mm and 15mm it is likely that the probes measured the velocity within the same wake, or just a wide wake due to the deviation of the flow through the gap between the tubes.

The question arising is about the occurrence or not of bistability or at least of a switching process for small blockage ratios. The switching process may not be detected by the probes due to the critical positioning or if, due to the small gaps (1.17,2.27 and 3.9mm), the turbulence scale are too small to produce the phenomenon. Table 2 shows the statistical characteristics for cylinders of 4.5, 9.1 and 15mm.

The cylinders with 25, 40 and 50mm showed the presence of the bistability phenomenon, where the number of changes decreases with the increase of the diameter. Results are summarized in Fig. 2.

In Figure 3, the measured velocities after the arrangement of cylinders with 60mm, occupy different levels without any change. For this highest blockage ratio (66.18%) it indicates that, after the onset of a stable deviated flow configuration, the narrowing of the wake, due to the proximity of the channel walls on both sides may hinder the switching process between two modes.

The signal, filtered and reconstructed for low frequencies by DWT, (Figure 3), shows a sort of "attempt" to return to the mode 2. This may be due to high blockage ratio that interfered in order to limit the lateral expansion of the wake, preventing the occurrence of the switching between modes.

Results Without Blockage

Since the study of bistability with small blockage ratios using cylinders with small diameters was inconclusive, a pair of cylinders with 25.1mm diameter was mounted outside the channel with the generatrices tangent to the outlet. Upper and lower walls were extended, so that no side walls were present. Velocity results obtained with a single wire are presented in Fig. 4. Compared to the results for the same cylinder diameter (25.1mm) obtained in presence of wall and a blockage ratio of 0.338, Fig. 2(a), the bistability remains in the absence of blockage but the time between changes seems to increase.

Spectrograms

The energy distribution of velocity signals is displayed in spectrograms made from the continuous wavelet trans-

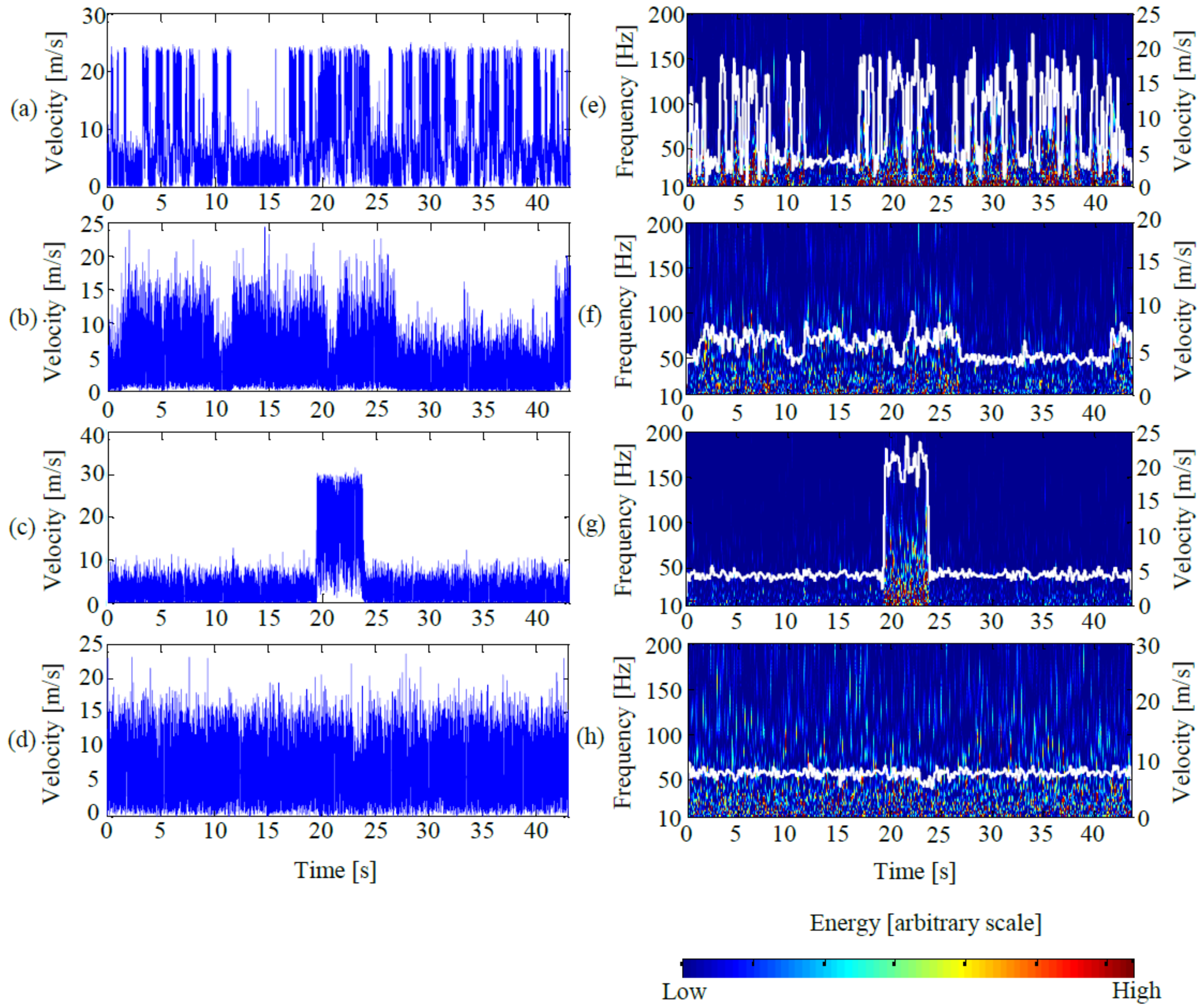

Figure 2: Velocity signals (a-d) and corresponding spectrograms (e-h) for different cylinder diameters and $p/d = 1.26$. (a, e) d = $25mm$ ($x/d = 0.338$ and $Re = 2.28 \times 10^4$). (b, f) d = $40mm$ ($x/d = 0.295$ and $Re = 3.54 \times 10^4$).(c, g) d = $50mm$ ($x/d = 0.25$ and $Re = 4.26 \times 10^4$). (d, h) d = $60mm$ ($x/d = 0.628$ and $Re = 4.81 \times 10^4$)

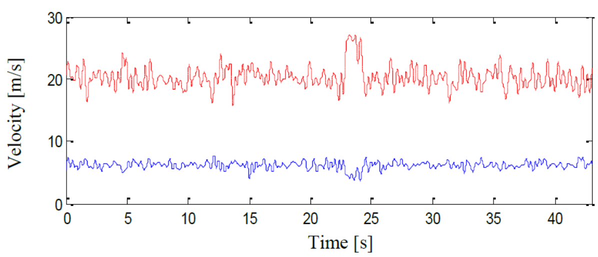

Figure 3: Reconstruction for cylinders with $60mm$ diameter and $p/d = 1.26$ (V1 blue line) (V2 red line)

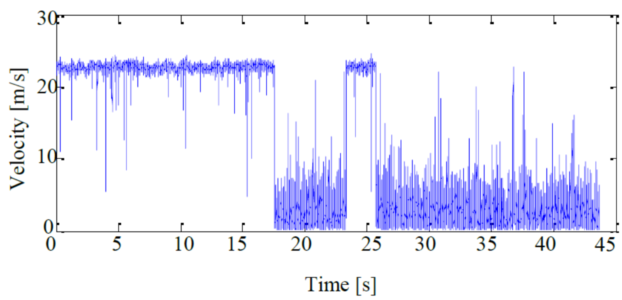

Figure 4: Axial velocity after a pair of cylinders with $25mm$ diameter and $p/d = 1.26$, mounted outside the channel

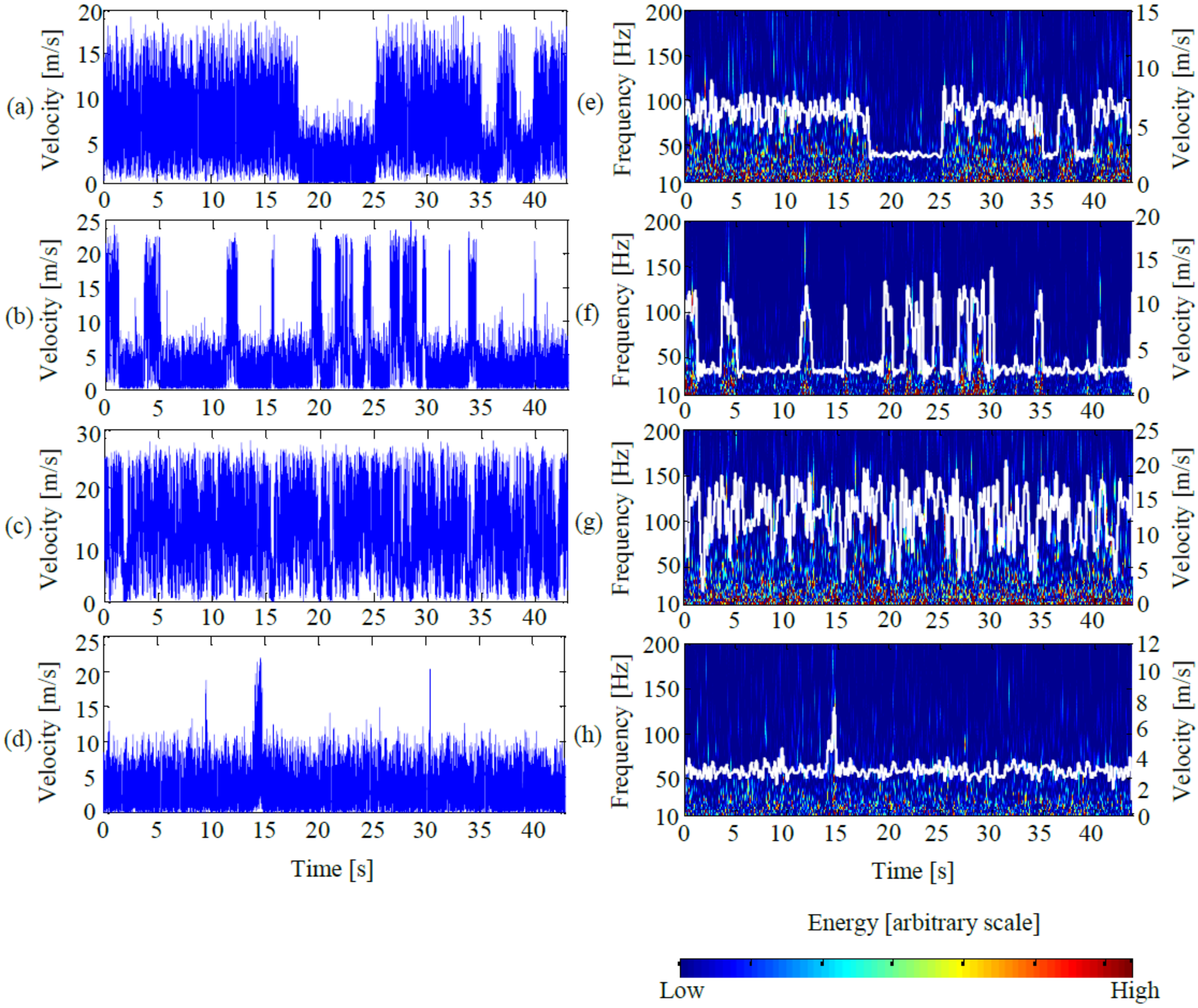

Figure 5: Velocity signals (a-d) and corresponding spectrograms (e-h) for different cylinder diameters and $p/d = 1.26$. (a, e) d = 15mm ($x/d = 0.733$ and $Re = 1.56 \times 10^4$). (b, f) d = 25mm ($x/d = 0.28$ and $Re = 2.63 \times 10^4$). (c, g) d = 40mm ($x/d = 0.15$ and $Re = 4.42 \times 10^4$). (d, h) d = 50mm ($x/d = 0.16$ and $Re = 5.82 \times 10^4$)

form, Figures 5 (e), (f), (g), (h), 5 (e), (f), (g), (h) and 7 (a), (b), (c), (d). The signals analyzed showed the mode change, characterizing the bistable phenomenon. Reconstructions of the lower frequency content of the signals processed by discrete wavelet analysis were grouped together with spectrograms.

The spectrograms presented in Figures 5 (e), (f), (g), (h) and 5 (e), (f), (g), (h) with the reconstruction of the velocity signals for cylinders where the bistable phenomenon occurs for $p/d = 1.26$ shows that regions that concentrate more energy in a wide frequency band are related to higher velocities. Consequently, lower velocities are associated with regions whose energy is lower.

Figure 6 shows the spectrograms with the reconstruction of the velocity signals V1 and V2 for cylinders with 25 (a,b) and 40mm (c,d). p/d-ratio 1.26. Results show that regions that concentrate more energy are related to higher velocities.

Some Considerations about Bistability Behavior

The observation of the spectrograms corroborates previous studies by de Paula and Möller [9] showing no evident correlation of the mode changes with time. Fig. 7 shows the reconstruction of the 2-D state space of bistable flow. By means of discrete wavelet transform, turbulence was filtered so that only the velocity changes without fluctuations other than bistability are shown. According to Takens [11], for an infinite number of points and without the presence of noise, the choice of reconstruction step of the time series is in most cases arbitrary. However, due to the finite size of the experimental time series and its contamination by external noise, reconstruction depends much in the correct choice of step reconstruction. A simple criterion used to choose the reconstruction step is when the value of the autocorrelation coefficient function drops to zero [12]. However, this time delay shown not to be adequate for the reconstruction of the time series. An alternative way to reconstruct the attractor is choosing several values of the time delay.

Flow visualizations performed in water channel with a Reynolds number of 7.5×10^3 and $p/d = 1.26$ are shown in Fig. 9, where the tubes has 60mm of diameter. Colored ink is injected inside the tubes, according to the feature to be studied.

When the attractor is not compressed around the diagonal nor covering the whole state space, it will be sufficiently unfolded. The time delay chosen in this process

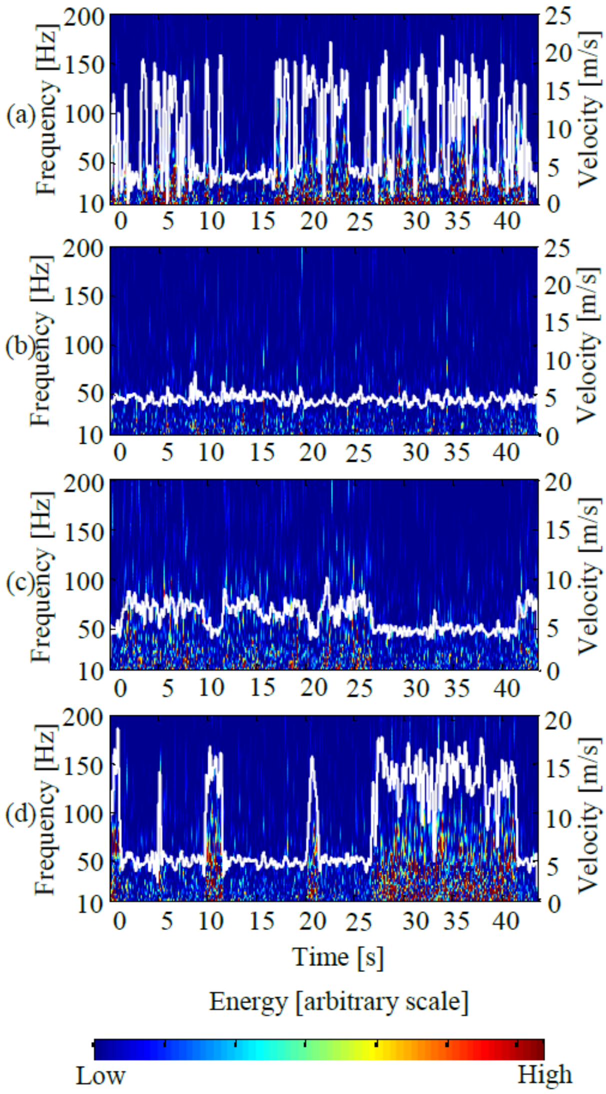

Figure 6: Spectrograms and reconstruction for signals of cylinders diameter for $p/d = 1.26$: (a) $25mm$ - probe 1, (b) $25mm$ - probe 2, (c) $40mm$ - probe 1 and (d) $40mm$ - probe 2

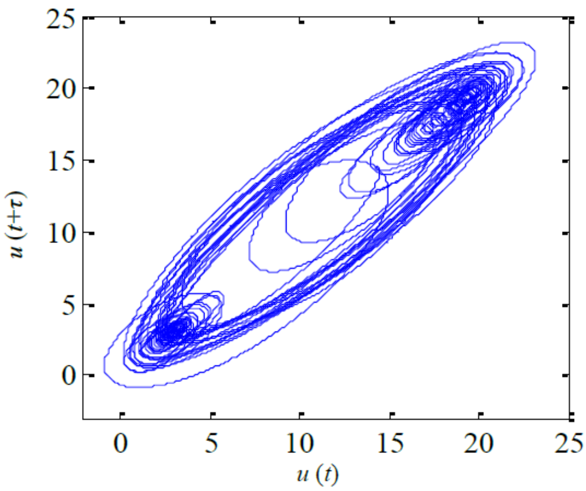

Figure 7: Reconstruction of the state space of bistable phenomenon from the time series after two side-by-side circular cylinders with $p/d = 1.26$ filtered with DWT of level $n = 9$ (frequencies from 0 to $1.9531 Hz$)

Table 1: Cylinder diameter and corresponding blockage ratio for two-cylinder arrangement

Cylinders diameters (mm)	Blockage ratio
4.5	4.66%
9.1	9.43%
15	15.54%
25	25.91%
32	33.16%
40	41.45%
50	51.81%
60	62.18%

is of 150 data points. The presence of two evident attractors, together with the fact observed in previous results that the blockage ratio, that means, boundary conditions, influence the occurrence of bistability lead to the evidence that the phenomenon studied is chaotic rather than random.

In Fig.8(a) it is observed the formation of a large wake behind one of the tubes (red ink) and a narrow wake behind the other tube (blue ink), which refers to mode 1. The transition between the two modes of the flow is observed in Fig. 8(b). After the switching of the gap flow (mode 2), the results are those in Fig. 8(c).

4 Conclusions

This paper presents a study on experiments performed on two cylinders subjected to turbulent flow. The effect of blockage ratio on bistable phenomenon, for two cylinders was studied. In this work, the blockage ratio was varied through the diameter of the cylinders. The p/d-ratio studied was 1.26. Measurements of the velocity fluctuations in the aerodynamic channel were made using the hot wire anemometry technique. The experiments were performed in the subcritical regime.

For two cylinders, the strong influence of blockage ratio on the bistable phenomenon was observed. Smaller cylinders, whose blockage ratios are less than 15% did not present the bistable phenomenon leading to the conclusion that it may not occur without the influence of the wall. Another reason of not detecting the bistability may be due to the small diameters of the cylinders: in this case, the wake may have not enough energy to produce the bistable process or the bistability has scale comparable to the length of the wire ($1.1mm$).

Arrangements with larger blockage ratios not only presented the phenomenon of bistability, but it also seems to decrease, with the increase of the blockage, with the gradual decrease in the number of changes.

The extreme case, the cylinder of larger diameter, $60mm$, has the highest blockage ratio studied. The proximity with the walls may hinder the occurrence of the phenomenon, confirming that as the blockage ratio is increased, the occurrence of the bistable phenomenon is reduced, as observed in the measurements with cylinders of diameters of 40 and $50mm$.

In fact, the blockage ratio, d/L, has to be the main measure of flow, since it can cause changes in flow and phenomena that involve, in particular, bistability.

Since the Reynolds number was determined by the velocity value, which was kept constant in each experiment its influence was not studied in this experimental work. The influence of the effect of blockage ratio, therefore, becomes more crucial on the bistability.

Table 2: Statistical characteristics of the velocity in the cylinders arrangement with $p/d = 1.26$

Cylinder diameter (mm)	Mean velocity (m/s)		Standard deviation (m/s)	Skewness	Kurtosis
4.5	V1	1.49	1.04	1.09	4.32
	V2	4.45	2.82	0.96	3.32
9.1	V1	1.88	1.37	0.99	3.91
	V2	5.66	3.28	0.88	3.09
15	V1	1.86	1.36	1.06	4.18
	V2	10.73	4.95	0.03	2.04

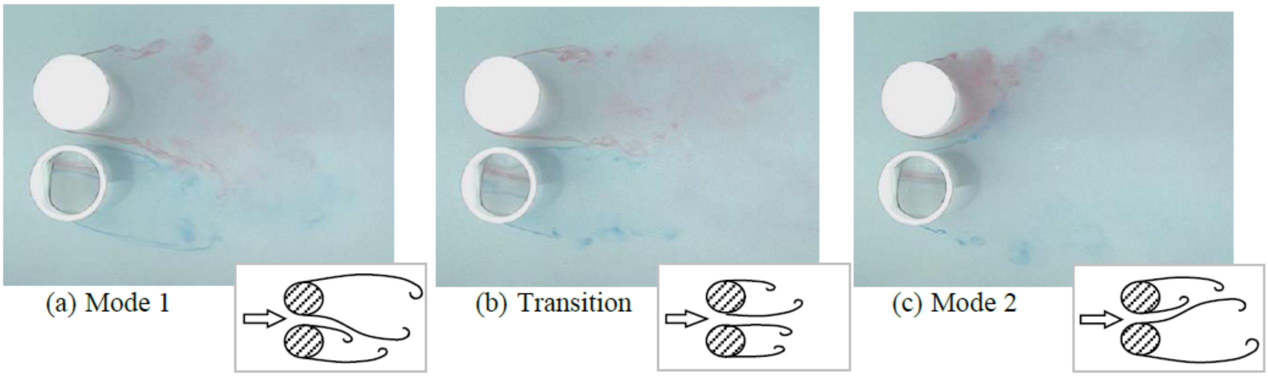

Figure 8: Flow visualization in water channel of two side-by-side circular cylinders with $p/d = 1.26$ in the top plan view. $Re = 7.5 \times 10$.

Analysis of bistable process indicates the presence of chaos, which demands further investigation.

Acknowledgements

S.V. Möller is gratefully indebted to the CNPq - National Council for Scientific and Technological Development, Ministry for Science, Technology and Innovation, Brazil, for the continuing financial support (BPP).

References

[1] Sumner, D., Wong, S. S. T., Price, S. J. and Paidoussis, M. P., 1999, "Fluid Behaviour of Side-by-Side Circular Cylinders in Steady Cross-Flow", Journal of Fluids and Structures, v. 13, pp. 309-338.

[2] Kim, H. J. and Durbin, P. A., 1988, "Investigation of the Flow between a Pair of Circular Cylinders in the Flopping Regime", Journal of Fluid Mechanics, v. 196, pp. 431-448.

[3] Peschard, I. and Le Gal, P., 1996, "Coupled Wake of Cylinders", Physical Review Letters, v. 77, pp. 3122-2125.

[4] Guillaume, D. W. and LaRue, J. C., 1999, "Investigation of the Flopping Regime with Two-, Three- and Four-Cylinder Arrays", Experiments in Fluids, v. 27, pp. 145-156.

[5] Zhou, Y., Zhang, H. J. and YIU, M. W., 2002, "The Turbulent Wake of Two Side-by-Side Circular Cylinders", Journal of Fluid Mechanics, v. 458, pp. 302-332.

[6] Alam, M.M., Moriya, M., Sakamoto, H., 2003, Aerodynamic characteristics of two side-by-side circular cylinders and application of wavelet analysis on the switching phenomenon, Journal of Fluids and Structures v. 18, pp. 325-346.

[7] Alam, M. M., and Zhou, Y., 2007, "Flow Around Two Side-by-Side Closely Spaced Circular Cylinders", Journal of Fluids and Structures, v. 23, pp. 799-805.

[8] Olinto, C.R., Indrusiak, M.L.S., Endres, L.A.M. and Möller, SV, 2009, "Experimental Study of the Characteristics of the Flow in the First Rows of Tube Banks", Nuclear Engineering and Design, v. 239, pp. 2022-2034.

[9] de Paula, A.V and Möller, S.V., 2013, Finite mixture model applied in the analysis of a turbulent bistable flow on two parallel circular cylinders, Nuclear Engineering and Design, nr. 264, pp. 203âĂŞ 213.

[10] Olinto, C. R., Indrusiak, M. L. S., Möller, S. V., 2005, Strouhal Number Fluctuations in a Cylinder Wake, Proceedings of COBEM 2005, 18th International Congress of Mechanical Engineering, available in `http://www.abcm.org.br/pt/wp-content/anais/cobem/2005/index.htm`.

[11] Takens, F., 1981, "Detecting strange attractors in turbulence", Lecture Notes in Mathematics, 898, 366-381.

[12] Abarbanel, H. D. I., Brown, R., Sidorowich, J. J. and Tsimring, L.S., 1993, "The analysis of observed chaotic data in physical systems", Reviews of Modern Physics, 65, 1331-1392.

A Methodology to Create Target Coefficients for RANS Modeling Using Data from DNS, LES, and Experiments

R.L. Thompson and L.E.B. Sampaio

LMTA-PGMEC, Department of Mechanical Engineering, Universidade Federal Fluminense, Niterói-RJ, 24210-240, Brazil

Abstract

Due to its low computational costs, RANS modeling will continue to be the preferred approach, for one or two decades ahead, in the great majority of problems related to turbulent flows that industries need to face in their every-day operation processes. The drawback of following such path is the lack of accuracy that RANS models are known to possess. On the other side of this issue, more accurate approaches such as DNS, LES, and experiments, are natural approaches when the aim is to understand the phenomenon. Here, we discuss a methodology that uses noble data sources in order to find coefficients of Explicit Algebraic Reynolds Stress Models (EARSM) that extend the Boussinesq hypothesis. Besides that, by using this procedure to different levels of approximation, depending on the choice of the basis of kinematic tensors used to describe the Reynolds Stress tensor, we are able to determine the intrinsic tensor error associated to each hypothesis. Two sets of data are examined: the DNS data of the square duct and the LES data of a backward facing step.

1 Introduction

In several industrial applications, Reynolds Averaged Navier-Stokes (RANS) modeling is still a widely employed approach to predict turbulent flows. The main advantage of this practice is the low computational cost of simulations when compared with Direct Numerical Simulations (DNS) and Large Eddy Simulations (LES). On the other hand, in the RANS approach only the mean velocity field is calculated and the physics of turbulence is captured by a closure equation that relates the Reynolds stress tensor with the mean kinematic quantities. In this sense, it is reasonable to expect a low level of accuracy with respect to other methodologies where the instantaneous velocity field is calculated.

In the last four decades, closure schemes for the Reynolds Stress tensor have been proposed in a variety of forms. The Boussinesq hypothesis, coupled with two differential equations, one for the turbulent kinetic energy, k, and other for the dissipation, ϵ, the so-called $k-\epsilon$ model has gained popularity. Another common approach is to consider the solution of a transport equation for the Reynolds Stress tensor, where other closures are needed.

In an intermediate level of closure complexity, there is a class called Non-Linear Eddy Viscosity Models (NLEVM) (see [1, 2]). In this type of approach, the usual Boussinesq assumption, where the anisotropic Reynolds stress tensor is proportional to the rate-of-strain tensor, is extended to other tensor basis, improving the models ability to predict turbulent flows. Hence, besides the turbulent viscosity, other coefficients corresponding to these expanded basis come into play. These coefficients can also be expressed in terms of two known turbulent scales, the turbulent kinetic energy, k, and its dissipation, ϵ. Therefore, this kind of model can also be coupled with the evolution equations for these quantities.

Within this class of models lies the group of Explicit Algebraic Reynolds Stress Models (EARSM) ([3, 4, 5, 6]) which are constructed from an equilibrium assumption for the advection of the anisotropic Reynolds stress tensor as discussed by [7, 8] in the transport equation for the Reynolds Stress tensor. In general, these models use representation theorems relating the anisotropy Reynolds Stress tensor with suitably chosen set of kinematic tensors. A different approach was considered by [9], where the first and second normal stress turbulent coefficients are the parameters to be determined, in an analogy with non-Newtonian fluids.

This intermediate level of approximation have two important challenges that need further investigation. The first is to delimit the range of applicability of the weak equilibrium assumption, so that it can represent real flow conditions. The other is how the large number of coefficients these models possesses can be determined.

The approach presented here intends to contribute with the construction of algebraic stress Reynolds models. We demonstrate that using two mean kinematic quantities, the rate-of-strain and the non-persistence-of-straining tensors, as representative independent tensors, there are at least six levels of approximation of the Reynolds stress anisotropy. We are not only able to determine the coefficients that rise from the models, but also to calculate the *intrinsic error tensor* associated to each model.

Two problems are analysed in the present work, the DNS data of the flow through a square duct and the LES data of the flow in the backward facing step.

2 Extending the Boussinesq Hypothesis

2.1 The Boussinesq Hypothesis

The Reynolds stress tensor, $\mathbf{R}$, defined through

$$\mathbf{R} = -\overline{\mathbf{u}\,\mathbf{u}}, \tag{1}$$

is considered here, $\overline{(.)}$ indicates the time average operation and lower case symbols denote the velocity fluctuations ($\mathbf{u}$) with respect to the average velocity ($\mathbf{U}$). Its deviatoric part known as anisotropy Reynolds tensor $\mathbf{a}$ is defined as

$$\mathbf{a} = \mathbf{R} - \frac{1}{3}\mathrm{tr}(\mathbf{R})\mathbf{1}, \tag{2}$$

where tr(.) is the trace operator and $\mathbf{1}$ is the identity tensor. The usual Boussinesq hypothesis explains tensor $\mathbf{a}$ by a linear relation with the mean-rate-of-strain tensor, $\mathbf{D}$, defined as

$$\mathbf{D} \equiv \frac{1}{2}(\nabla \mathbf{U} + \nabla^T \mathbf{U}), \tag{3}$$

The Boussinesq hypothesis is an analogy based on the Newtonian molecular hypothesis expressed as

$$\mathbf{a} = 2\nu_T \mathbf{D}, \tag{4}$$

where ν_T is the turbulent viscosity.

The question here is: besides the rate-of-strain tensor, which other tensors can come into play in order to help $\mathbf{D}$ to explain ($\mathbf{a}$)? The first idea that comes into mind is that we need to incorporate the vorticity tensor, $\mathbf{W} \equiv \frac{1}{2}(\nabla^T \mathbf{U} - \nabla \mathbf{U})$, somehow, since it is known that turbulent flows are intrinsically rotational. A common approach adopted by some groups that use EARSM was to consider general tensorial representations of $\mathbf{a}$ using $\mathbf{D}$ and $\mathbf{W}$. In the present work we call the attention of the reader for a different option.

2.2 The non-persistence-of-straining tensor

[10] and [11] have independently shown the importance of the so-called *effective vorticity*. Effective vorticity is vorticity as measured by a reference frame attached to the eigenvectors of $\mathbf{D}$. It is defined as

$$\mathbf{W}^* \equiv \mathbf{W} - \mathbf{\Omega^D}. \tag{5}$$

where $\mathbf{\Omega}^D \equiv \dot{\mathbf{e}}_k^D \mathbf{e}_k^D$, and $\mathbf{e}_k^D$ and $\dot{\mathbf{e}}_k^D$ are the unit eigenvectors of $\mathbf{D}$, and its material time derivative, respectively.

Effective vorticity measures the ability of the flow to change the material filaments that are aligned with the the principal directions of the rate-of-strain tensor. Therefore, a filament that is aligned with an eigenvector corresponding to a positive eigenvalue will be severely stretched in the case where effective vorticity vanishes.

However, [12] have shown that the quantity that is responsible for deviating the motion from an extensional one is the non-persistence-of-straining tensor $\mathbf{P}$ defined as

$$\mathbf{P} \equiv \mathbf{D}\mathbf{W}^* - \mathbf{W}^*\mathbf{D}. \tag{6}$$

Besides vanishing at zero effective vorticity, tensor $\mathbf{P}$ also accounts for the fact that rotations in the plane defined by eigenvectors corresponding to similar eigenvalues does not promote the same level of *stretch relieving* as a rotation in the plane defined by eigenvectors corresponding to eigenvalues of significant different magnitudes.

3 Methodology

The proposed methodology is a development of a tensor decomposition proposed by Thompson et al. ([13], [14]). There are two kinds of additive decompositions, of one tensor, $\mathbf{F}$, with respect to a second one, $\mathbf{G}$, i.e. $\mathbf{F} = \mathbf{P}_F^G + \widetilde{\mathbf{P}}_F^G$ that obey the following properties:

1. $\mathbf{P}_F^G$ is a part of $\mathbf{F}$ that is coaxial with $\mathbf{G}$.
2. $\widetilde{\mathbf{P}}_F^G$ is a part of $\mathbf{F}$ that is orthogonal to $\mathbf{G}$.
3. $\mathbf{P}_F^G$ and $\widetilde{\mathbf{P}}_F^G$ are orthogonal.

The first one is referred to *proportional-orthogonal decomposition* and decomposes an original tensor $\mathbf{F}$ with respect to a tensor $\mathbf{G}$ as

$$\mathbf{F} = \frac{\mathrm{tr}\,(\mathbf{F}\cdot\mathbf{G})}{\mathrm{tr}\,(\mathbf{G}\cdot\mathbf{G})}\mathbf{G} + \frac{\mathrm{tr}\,(\mathbf{G}\cdot\mathbf{G})\,\mathbf{F} - \mathrm{tr}\,(\mathbf{F}\cdot\mathbf{G})\,\mathbf{G}}{\mathrm{tr}\,(\mathbf{G}\cdot\mathbf{G})}. \tag{7}$$

The second kind, denominated *in-phase-out-of-phase decomposition*, decomposes a tensor $\mathbf{F}$ with respect to tensor $\mathbf{G}$ as,

$$\mathbf{F} = \mathbf{1}^{\mathbf{GG}} : \mathbf{F} + \left(\mathbf{1}^{\delta\delta} - \mathbf{1}^{\mathbf{GG}}\right) : \mathbf{F}, \tag{8}$$

where the symbol : represents here the double product between two tensors, where $\mathbf{1}^{\delta\delta}$ and $\mathbf{1}^{\mathbf{GG}}$ and fourth order tensors.

3.1 Six Models

We are able to produce six levels of representations of the Reynolds stress, depending on the combinations of the adopted decompositions. Besides that, we use k and ϵ to scale these coefficients. The final form of these models are given by:

$$M_I:\ \mathbf{a} = 2\frac{\kappa^2}{\epsilon}C_\mu\mathbf{D} + \mathbf{E}_I$$

$$M_{II}:\ \mathbf{a} = \kappa C_{\mu 0}\mathbf{I} + 2\frac{\kappa^2}{\epsilon}C_{\mu 1}\mathbf{D} + \frac{\kappa^3}{\epsilon^2}C_{\mu 2}\mathbf{D}^2 + \mathbf{E}_{II}$$

$$M_{III}:\ \mathbf{a} = C_{\mu 0}\kappa\mathbf{I} + 2\frac{\kappa^2}{\epsilon}C_{\mu 1}\mathbf{D} + \frac{\kappa^3}{\epsilon^2}C_{\mu 2}\mathbf{D}^2 + \frac{\kappa^3}{\epsilon^2}C_\beta\mathbf{P} + \mathbf{E}_{III}$$

$$M_{IV}:\ \mathbf{a} = 2\frac{\kappa^2}{\epsilon}C_\mu\mathbf{D} + \frac{\kappa^3}{\epsilon^2}C_\beta\mathbf{P} + \mathbf{E}_{IV}$$

$$M_V:\ \mathbf{a} = \kappa C_{\beta 0}\mathbf{I} + 2\frac{\kappa^2}{\epsilon}C_\mu\mathbf{D} + \frac{\kappa^3}{\epsilon^2}C_{\beta 1}\mathbf{P} + \frac{\kappa^6}{\epsilon^4}C_{\beta 2}\mathbf{P}^2 + \mathbf{E}_V$$

$$M_{VI}:\ \mathbf{a}_{VI} = \kappa C_{\mu\beta 0}\mathbf{I} + 2\frac{\kappa^2}{\epsilon}C_{\mu 1}\mathbf{D} + \frac{\kappa^3}{\epsilon^2}C_{\mu 2}\mathbf{D}^2 +$$

$$+\frac{\kappa^3}{\epsilon^2}C_{\beta 1}\mathbf{P} + C_{\beta 2}\frac{\kappa^6}{\epsilon^4}\mathbf{P}^2 + \mathbf{E}_{VI}$$

where $\mathbf{M}_i$ labels the model, $C_{\mu i}$ and $C_{\beta j}$ are dimensionless scalar coefficients, and $\mathbf{E}_i$ is the intrinsic error tensor associated to the i-approximation.

Model $\mathbf{M}_I$ is obtained from a decomposition of the anisotropic Reynolds stress, $\mathbf{a}$, into a proportional-to-$\mathbf{D}$ part, $2\frac{\kappa^2}{\epsilon}C_\mu\mathbf{D}$, and an orthogonal-to-$\mathbf{D}$ part, the intrinsic error $\mathbf{E}_I$. Hence, if we replace tensor $\mathbf{F}$, in Eq. (Eq. (7)), by $\mathbf{a}$ and tensor $\mathbf{G}$ in the same equation, by $\mathbf{D}$, then $2\frac{\kappa^2}{\epsilon}C_\mu$ would be given by the coefficient of the first term of Eq. (Eq. (7)), i.e.

$$2\frac{\kappa^2}{\epsilon}C_\mu = \frac{\mathrm{tr}\,(\mathbf{a}\cdot\mathbf{D})}{\mathrm{tr}\,(\mathbf{D}\cdot\mathbf{D})}, \tag{9}$$

while $\mathbf{E_I}$ is given by the second term of Eq. (Eq. (7)) with the same replacement. This decomposition leads to the Boussinesq hypothesis and the intrinsic error associated to this assumption, and the coefficient $2\frac{\kappa^2}{\epsilon}C_\mu$ can be seen as a eddy-viscosity. The other models ($\mathbf{M}_{II}$ up to $\mathbf{M}_{VI}$) are of the type NLEVM.

Model $\mathbf{M}_{II}$ originates from a decomposition of $\mathbf{a}$ into a in-phase-with-$\mathbf{D}$ part, which in turn, from the Cayley-Hamilton theorem, can be written as a linear combination of tensors $\mathbf{I}$, $\mathbf{D}$, and $\mathbf{D}^2$, and an out-of-phase-to-$\mathbf{D}$

part, $\mathbf{E}_{II}$. In other words, replacing tensors $\mathbf{F}$ and $\mathbf{G}$ in Eq. (Eq. (8)) by tensors $\mathbf{a}$ and $\mathbf{D}$, respectively, we have that

$$\kappa C_{\mu 0}\mathbf{I} + 2\frac{\kappa^2}{\epsilon} C_{\mu 1}\mathbf{D} + \frac{\kappa^3}{\epsilon^2} C_{\mu 2}\mathbf{D}^2 = \mathbf{1^{DD}} : \mathbf{a}, \qquad (10)$$

and the coefficients of the linear combination are obtained from a Vandermonde system (see [14]). Models M_I and M_{II} exemplify how Eqs. (Eq. (7)) and (Eq. (8)) are employed. The way the other models are built is described below, with the appropriate replacements.

Taking model $\mathbf{M}_{II}$ as starting point, model $\mathbf{M}_{III}$ is built by extracting from $\mathbf{E}_{II}$ the part that is proportional to $\mathbf{P}$, what leads to the intrinsic error $\mathbf{E}_{III}$. The legitimacy of this procedure is based on the fact that $\mathbf{P}$ is orthogonal to $\mathbf{D}$. Model $\mathbf{M}_{IV}$ benefits also from the same fact, if we take model $\mathbf{M}_I$ as starting point. This model is formed by extracting from $\mathbf{E}_I$ the part that is proportional to $\mathbf{P}$, leading to the intrinsic error $\mathbf{E}_{IV}$. In model $\mathbf{M}_V$ we first decompose the Reynolds stress anisotropy into a part that is in-phase-with-$\mathbf{P}$, which can be written as $\beta_0\mathbf{I} + \beta_P\mathbf{P} + \beta_{P2}\mathbf{P}^2$, and after that we extract from the out-of-phase-to-$\mathbf{P}$ part, the proportional-to-$\mathbf{D}$ part. The complement of this procedure is the intrinsic error of model $\mathbf{M}_V$, $\mathbf{E}_V$. The last model shown here, $\mathbf{M}_{VI}$ is obtained taking model $\mathbf{M}_{II}$ as starting point and extracting from $\mathbf{E}_{II}$ the part that is in-phase with $\mathbf{P}$, what leads to the intrinsic error $\mathbf{E}_{VI}$.

3.2 Indexes for Performance Evaluation

We apply indexes of adherence to quantify the ability of the particular model to capture the Reynolds tensor. These indexes, IR_i, where the subscript i, varying from I to VI indicates the model, can be seen as a measure of the theoretical limit intrinsic to each of the models alone:

$$R_i = 1 - \frac{2}{\pi}\cos^{-1}\left(\sqrt{\frac{\mathrm{tr}\left(\mathbf{a} - \mathbf{E}_{\mathrm{i}}\right)^2}{\mathrm{tr}\left(\mathbf{a}^2\right)}}\right). \qquad (11)$$

Indexes R_i are limited, i.e., $R_i \in [0, 1]$, the limiting cases being $R_i = 0$ when the model is out of the Reynolds stress tensor subspace, and $R_i = 1$ when they are coincident.

4 Examples

4.1 DNS - Square Duct

The basic flow statistics of the incompressible turbulent flow through a straight duct of square cross section (Figure (1)) at low Reynolds number are available through a number of independent direct simulations of this bounded flow, see e.g. [15, 16, 17]. There is good qualitative agreement in the statistics extracted from these simulations, thus enabling the study of the duct flow to be undertaken with some confidence. The simulation database that will be used in this paper is that obtained by [17]. Briefly, we describe the main characteristics of the simulation next. For spatial approximation of the Navier-Stokes equations, a mixed Fourier and finite difference approximation scheme was used. The flow variables were expanded into discrete Fourier series along the homogeneous streamwise direction (x), whereas second-order centered difference approximations were used for the inhomogeneous directions (y, z).

The time marching method was based on the second-order Adams-Bashforth scheme for all terms of the equations of motion.

The Reynolds number based on the bulk velocity, $\overline{U}_m$ and on the hydraulic duct diameter is 4800. The frictional Reynolds number in wall units is $Re_\tau = u_\tau h/\nu = 160$, where h is the half height of the SD and ν the kinematic viscosity. The grid has $768(x) \times 127(y) \times 127(z)$ points. The grid resolution in ν/u_τ units is 10.5 in x and between 0.48 and 4.6 in y and z directions, with mesh refinement towards the duct corners. Due to the geometry and flow-statistics symmetry, only the results for the left bottom corner of the duct are presented here.

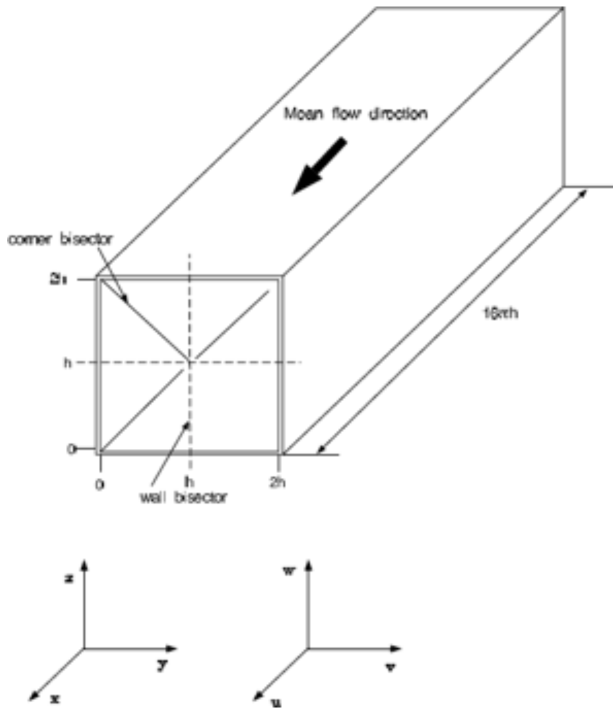

Figure 1: Scheme of the flow through a square duct

The different fields shown next correspond to the lower-left quadrant of cross section area. On the left of Figure (2), we can find the field of coefficient C_μ given by Eq. Eq. (9). There, we can notice the domain symmetry with respect to the diagonal axis and a region where $C_\mu \approx 0.09$, an expected value for channel flows. On the right side of Figure (1) it is shown the performance index through the domain. There we can find that the maximum value of this normalized quantity is a round 0.5, making explicit the poor prediction of the Boussinesq hypothesis. The dimensionless coefficients for models M_{II} and M_{III} are shown in Figure (3); while the ones for model M_V is shown in Figure (4). The dimensionless coefficient associated to the persistence-of-straining tensor of model M_{IV} is similar to $C_{\beta 1}$ and the coefficient corresponding the unit tensor for model M_{VI} is $C_{\mu 0} + C_{\beta 0}$.

The indices of performance for different models are depicted in Figure (5). There we can find a higher level of fidelity with respect to the Reynolds Stress anisotropy tensor as the complexity of the case grows. We can also notice that, adding the non-persistence-of straining model, is more efficient than adding a nonlinear term in $\mathbf{D}$. It is also interesting to notice that Models M_{III}, M_V, and M_{VI} are able to capture the Reynolds Stress tensor almost everywhere with a high level of R even in the lowest regions.

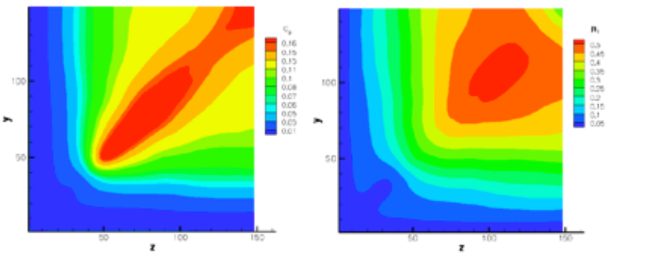

Figure 2: On the left, the field of coefficient C_μ. On the right the performance index R_I

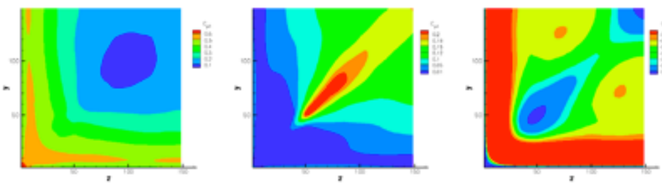

Figure 3: Coefficients $C_{\mu 0}$, $C_{\mu 1}$, and $C_{\mu 2}$ corresponding to models M_{II}, M_{III}, and M_{VI}

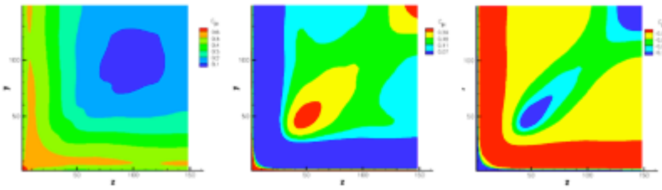

Figure 4: Coefficients $C_{\beta 0}$, $C_{\beta 1}$, and $C_{\beta 2}$ corresponding to model M_V

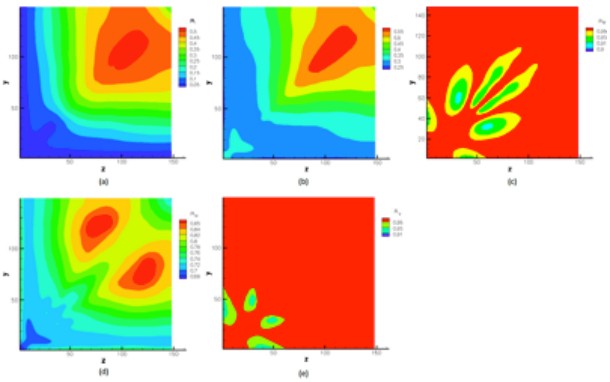

Figure 5: Performance index for the models, from M_I to M_V

4.2 LES - Backward Facing Step

The backward facing step flow, with its discretization and modeling, are treated in a deeper level of detail in the following subsections. This numerical large eddy simulation was done in this work allowing us to compared its results with the proposed RANS models.

4.2.1 Geometry: Backward facing step

The backward facing step is a classical benchmark test case, and has been extensively used in the literature to validate turbulence models. Here we use the same geometry as [18], with a 1.2 expansion ratio ($ER = L_y - h/L_y$, with $L_y = 6h$), shown in Figure (6). The other dimensions are $L_x = 23h$, $L_z = 4h$, and $L_i = 3h$, where h is the step height, L_i is the inlet length, before the step, and L_x, L_y, L_z are the total length, height and span, respectively.

The inlet boundary conditions are: imposed velocity, according to a profile obtained with DNS ([18]) at $x = -3h$ from the step. The step height based Reynolds number was $Re = U_0 h/\nu = 5100$, where U_0 is the maximum velocity.

The outlet is set as an outflow, with fixed pressure (zero) and null Neumann boundary conditions for velocity and turbulence variables. The bottom surfaces are set as walls, while the top, as an impenetrable no-stress plane. The lateral planes are set as periodic.

4.2.2 Discretization

The mass and momentum equations were discretized using the Finite Volume Method (FVM) implemented in OpenFOAM [19]. The field values are stored at the control volume centroids. Whenever fluxes or other face quantities are needed, the centroid values are interpolated to the face centroids, using the most appropriate scheme. Here, a linear interpolation is used for the velocity field, corresponding to the classical central differences scheme of Finite Difference Method (FDM). This avoids extra dissipation which would otherwise affect the turbulence spectrum, and it is the recommended scheme when a physical modeling approach is chosen over an implicit LES. On the other hand, for variables like the subgrid turbulent kinetic energy, which cannot assume negative values and should be bounded, a Total Variation Diminishing (TVD) scheme based on Minmod limiter is employed. This guarantees a bounded behavior when high frequency oscillations are eminent, yet an accurate discretization for smoother modes.

The discretization of these equations generates three sets of linear systems, corresponding to the mass, momentum, and subgrid turbulence equations, which are solved separately, in a segregated approach. During a time step of the transient evolution, the momentum is solved first, then the pressure is found to correct the mass conservation, and lastly the subgrid kinetic energy (k_{SGS}) is found from its own transport equation, which depends on the velocity found in the other two steps. This subgrid kinetic energy field is used in a dynamic framework to find the instantaneous and local subgrid viscosity. Numerical experiments suggested that the subgrid kinetic energy-velocity coupling inside a single time step is far less important than the velocity-pressure coupling. Therefore, an inner loop coupling is performed only for the velocity and pressure fields, using the PISO methodology [20].

An hexahedral mesh was used for the present work. It consists of $300 \times 160 \times 32$ subdivisions in the streamwise (x), vertical (y) and spanwise (z) directions respectively. In the x-direction, 40 subdivisions out of the total (300) were placed before the step, with a small concentration towards the step. Also, in the y-direction a non-uniform distribution of subdivisions was employed, concentrating control volumes close to the wall and in the step level. After simulation was ran and the mean wall shear stress was obtained, it was possible to evaluate the near wall normal spacing in wall units, $\Delta y^+ = \Delta y/\delta$. The wall characteristic length is given by $\delta = \nu/u_* = \nu/\sqrt{\tau_w/\rho}$, where τ_w is the local mean wall shear stress. The resulting near wall mesh spacing in wall units were $\Delta y^+ = 0.56$ in average, and $\Delta y^+ = 7.57$ in the coarse case, indicating that a suitable resolution was obtained to tackle turbulence with LES and that this resolution was not that far from the DNS performed in [18].

4.2.3 LES Model

The Navier-Stokes equation and continuity are implicitly filtered in space, taking advantage of the Finite Volume Methods integral over each control volume. The resulting equation presents an additional term representing the subgrid (filtered) scales and its interaction with the resolved scales, which needs modeling as it cannot be closed. This term is modeled according to the Boussinesq hypothesis, in the framework of a functional model, where the dissipative role it plays in the energy cascade is more important than the exact capturing of the subgrid stress tensor structure.

The subgrid stress tensor, or more precisely, its deviatoric part, is thus assumed tied to the symmetric part of the resolved velocity gradient, by means of a "subgrid" viscosity, which is the very essence of all the modeling involved.

To provide the local value of this viscosity, two characteristics quantities are generally needed. Among the various modeling options, we choose the one equation subgrid model of Horiuti [21], in which the two characteristic values are the subgrid kinetic energy (k_{SGS}), given by its own additional transport equation, and a length scale, given by the cubic root of the control-volume volume. The constant parameters of the model were dynamically adjusted, locally and for each time step, following the Germano methodology [22, 23].

The simulations were run for more then fifty (50) domain flow-through times, allowing enough convergence for the statistics. An equivalently large initial transient period was discarded before reseting all averages being calculated during the simulations.

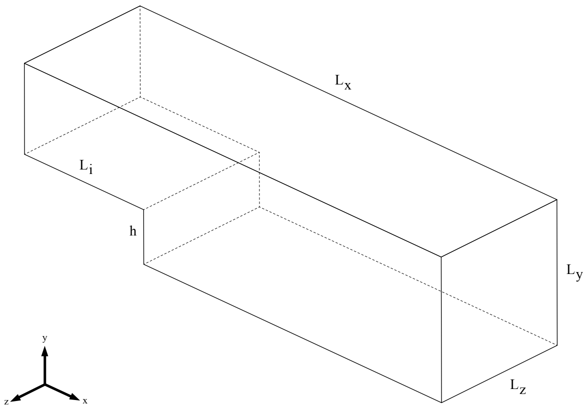

Figure 6: Scheme of the backward facing step geometry

The instantaneous and mean velocities are shown in Figure (7). From the instantaneous velocity field we can easily see that turbulence is confined to the region, after the step, near the wall.

Figure (8) shows the performance index for this complex flow for the six models. The reddish regions are regions where the indices are approximately unit. The blueish part, on the other hand shows less level of predictability. Once more, the Boussinesq hypothesis shows its poor capacity of predicting the Reynolds Stress tensor.

5 Conclusions

The employment of tensorial decompositions with the inclusion of the non-persistence-of-straining tensor seems

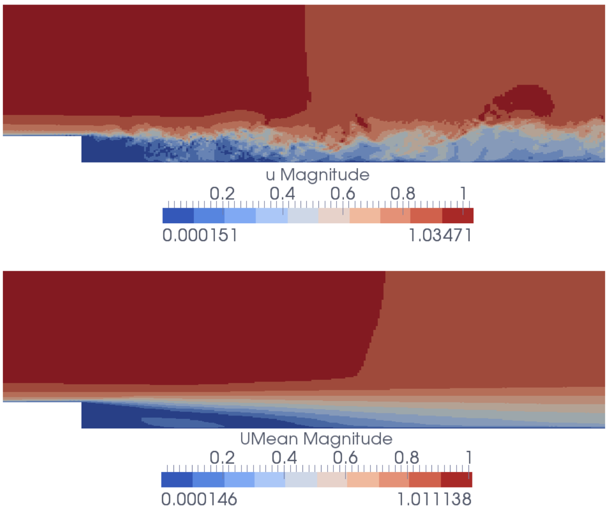

Figure 7: Instantaneous and mean velocity fields

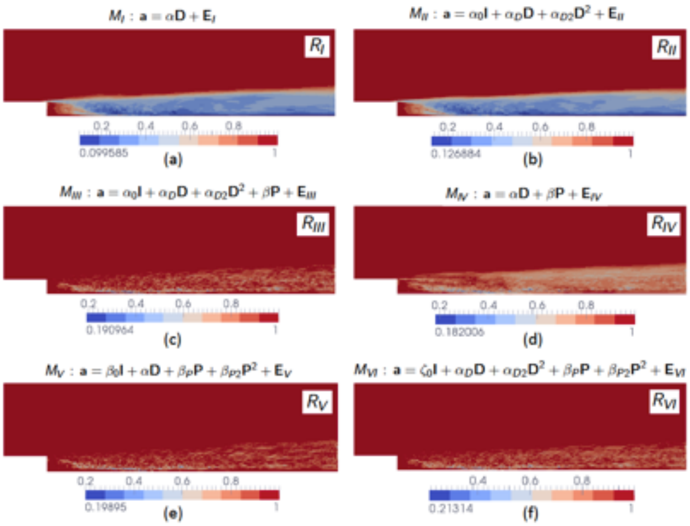

Figure 8: Performance indices for the backward facing step problem

to be a promising path to explore. Since the mean-non-persistence-of-straining tensor, **P**, is orthogonal to the mean-rate-of-strain tensor, **D**, that tensor is able to explore tensorial subspaces not reached by **D**. The known limitations of the Boussinesq hypothesis can be mitigated by this approach. A second stage of the methodology consists on finding wall functions in order to propose expressions for the coefficients involved, so that a true model can be formulated. In this second part of the methodology, we will be able to compare the computational costs associated to the increase of the tensor basis, and formulate a quantitative measure of the costs and benefits of this approach.

References

[1] J. L. Lumley, "Toward a turbulent constitutive relation," *J. Fluid Mech.*, vol. 41, pp. 413–434, 1970.

[2] S. Pope, "A more general effective-viscosity hypothesis," *J. Fluid Mech.*, vol. 72, pp. 331–340, 1975.

[3] T. B. Gatski and C. G. Speziale, "On explicit algebraic stress models for complex turbulent flows," *J. Fluid Mech.*, vol. 254, pp. 59–78, 1993.

[4] S. S. Girimaji, "Fully explicitly and self consistent algebraic Reynolds stress model," *Theoret. Comput. Fluid Dyn.*, vol. 8, pp. 387–402, 1996.

[5] S. Wallin and A. V. Johanson, "An explicit algebraic Reynolds stress model for incompressible and compressible turbulent flows," *J. Fluid Mech*, vol. 403, pp. 89–132, 2000.

[6] S. Wallin and A. V. Johanson, "Modelling streamlines curvature effects in explicit algebraic Reynolds stress turbulence model," *International Journal of Heat and Fluid Flow*, vol. 23, pp. 721–730, 2002.

[7] T. Jongen and T. Gatski, "General explicit algebraic stress relations and best approximation for three-dimensional flows," *Int. J. Engng. Sci.*, vol. 36, pp. 739–763, 1998.

[8] R. L. Thompson and G. Mompean, "An alternative assessment of weak-equilibrium conditions in turbulent closure modeling," *Int. J. Engng. Sci.*, vol. 48, pp. 1633–1640, 2010.

[9] X. Qiu, G. Mompean, F. Schmitt, and R. Thompson, "Modeling turbulent–bounded flow using non-newtonian viscometric functions," *J. Turb.*, vol. 12, pp. 1–18, 2011.

[10] G. Astarita, "Objective and generally applicable criteria for flow classification," *J. Non-Newt. Fluid Mech.*, vol. 6, pp. 69–76, 1979.

[11] M. Tabor and I. Klapper, "Stretching and alignment in chaotic turbulent flows," *Chaos, Soliton, and Fractals*, vol. 4, pp. 1031–1055, 1994.

[12] R. L. Thompson and P. R. Souza Mendes, "Persistence of straining and flow classification," *Int. J. Engng. Sci*, vol. 43, no. 1-2, pp. 79–105, 2005.

[13] R. L. Thompson, "Some perspectives on the dynamic history of a material element," *Int. J. Engng. Sci*, vol. 46, pp. 524–549, 2008.

[14] R. L. Thompson, G. Mompean, and L. Thais, "A methodology to quantify the non-linearity of the Reynolds stress tensor.," *J. Turb.*, vol. 11, pp. 1–27, 2010.

[15] A. Huser and S. Biringen, "Direct numerical simulation of turbulent flow in a square duct," *J. Fluid Mech.*, vol. 257, pp. 65–77, 1993.

[16] S. Gavrilakis, "Numerical simulation of low-Reynolds-number turbulent flow through a straight square duct," *J. Fluid Mech.*, vol. 244, pp. 101–116, 1992.

[17] S. Gavrilakis, "Turbulent velocity structures derived from pod analyses.," *Institut de Machines Hydrauliques et de Mécanique des Fluides, École Polytechnique Fédérale de Lausanne.*, vol. Report T-93-30, pp. C134–C156, 1993.

[18] H. Le, P. Moin, and J. Kim, "Direct numerical simulation of turbulent flow over a backward-facing step," *Journal of Fluid Mechanics*, vol. 330, pp. 349–374, 1997.

[19] "Userguide and programmers guide." www.openfoam.org, 2013.

[20] R. I. Issa, "Solution of the implicitly discretised fluid flow equations by operator-splitting," *Journal of Computational Physics*, vol. 62, pp. 40–65, Jan. 1986.

[21] A. Yoshizawa and K. Horiuti, "A statistically-derived subgrid-scale kinetic energy model for the large-eddy simulation of turbulent flows," *Journal of the Physical Society of Japan*, vol. 54, no. 8, pp. 2834–9, 1985.

[22] M. Germano, U. Piomelli, P. Moin, and W. Cabot, "A dynamic subgrid-scale eddy viscosity model," *Physics of Fluids A: Fluid Dynamics*, vol. 3, p. 1760, 1991.

[23] S. Ghosal, T. Lund, P. Moin, and K. Akselvoll, "A dynamic localization model for large-eddy simulation of turbulent flows," *Journal of Fluid Mechanics*, vol. 286, pp. 229–255, 1995.

ERCOFTAC Workshops and Summer Schools

ERCOFTAC Workshops, Conferences – 2015/16

Title	Location	Date	Coordinators	Organiser
Multiscale-forced Turbulent Flows: Fundamentals and Applications	Sheffield, UK	07-08/09/2015	Vassilicos, J.C. Nicolleau, F.	SIG44, SIG42
14th Workshop on Two – Phase Flow Predictions	Halle, Germany	07-10/09/2015	Sommerfeld, M.	SIG12
Global Flow Instability and Control	Crete, Greece	28/09/2015 – 02/10/2015	Theofilis, V.	SIG33
New Challenges in Internal Wave Dynamics: From Idealized studies to Geophysical Applications	Lyon, France	14-16/10/2015	Venaille, A.	SIG35
Uncertainty Quantification in CFD and Fluid Structure Interaction	Crete, Greece	5-10/06/2016	Sarkar, S. Witteveen, J.	SIG45

ERCOFTAC Summer Schools, Courses – 2015/16

Title	Location	Date	Coordinators	Organiser
School on Numerical Methods for Global Flow Instability and Control	Crete, Greece	22-25/09/2015	Theofilis, V. Hanifi, A.	SIG33
JMBC/ICISS Course on Combustion	Eindhoven, The Netherlands	19-22/01/2016	van Oijen, J.A. de Goey, L.P.H.	SIG28

Ercoftac Industry Events 2015

Dr. Richard E. Seoud

OCTOBER 2015

BPG: CFD for Dispersed Multi-Phase Flows, 1-2 October 2015 Imperial College London, UK
Coordinator: Prof. M. Sommerfeld, Halle-Wittenberg Univ., Germany
The course will provide:

- Best Practice Guidance for E-L, and E-E methods
- CFD for (wall bounded) turbulent dispersed multiphase flows with bubbles, drops or particles
- Problem shooting sessions

Lattice Boltzmann Methods for Industrial Apps, 19-20 Oct. 2015, Aix-Marseille Universite, Marseille, France
Coordinator: Prof. P Sagaut, Aix-Marseille, Univ. France
The course will provide:

- The fundamentals of LBM and Latest Guidances
- State-of-the-Art applications in engineering
- Examples in aerodynamics,acoustics and heat transfer

Best Practice for Eng CFD, 22-23 Oct. 2015 GE, Munich, Germany
Coordinator: Prof. C. Hirsch, Universiteit Brussel, & Pres. Numeca Int'l, Belgium
The course will provide:

- Best Practice Guidance for single phase flows and highlights common pitfalls
- Turbulence modelling that is centred around RANS, LES, to include impact on heat transfer
- CFD analysts with the tools to significantly enhance their use of commercial and open source software

NOVEMBER 2015

Hybrid RANS-LES Methods for Industrial CFD Overview, Guidance and Examples .ANSYS, Munich, Germany, 9-10 November 2015
Coordinator: Prof. S-H. Peng, FOI, Stockholm, Sweden
The course will provide:

- An overview of turbulence modelling
- A firm foundation in the theory and ideas underlying, RANS, LES and Hybrid RANS-LES techniques.
- Recommendation and guidance for the appropriate and effective application of Hybrid RANS-LES. Examples from real-world engineering simulations, using the DES class of models.

Uncertainty Management & Quantification in Industrial Design and Analysis, EDF, Chatou, Paris, France, 30 Nov-1 Dec 2015
Coordinator: Prof. C. Hirsch, Universiteit Brussels, & Numeca Intl
The course will provide:

- General introduction
- A firm foundation in the theory and ideas underlying, latest methods and techniques.
- Application of UM&Q in Aerospace, F1, Marine, Turbomachinary and Nuclear industry

Join us for an unrivalled 21st Century FTAC journey!
`http://www.ercoftac.org/about/ercoftac_membership/`

ERCOFTAC Special Interest Groups

1. **Large Eddy Simulation**
Salvetti, M.V.
University of Pisa, Italy.
Tel: +39 050 221 7262
Fax: +39 050 221 7244
`mv.salvetti@ing.unipi.it`

4. **Turbulence in Compressible Flows**
Dussauge, Jean-Paul
IUSTI, Marseille
`jean-paul.dussauge@polytech.univmrs.fr`

5. **Environmental Fluid Mechanics**
Armenio, V.
Universit di Trieste, Italy.
Tel: +39 040 558 3472
Fax: +39 040 572 082
`armenio@dica.units.it`

10. **Transition Modelling**
Dick, E.,
University of Ghent, Belgium.
Tel: +32 926 433 01
Fax: +32 926 435 86
`erik.dick@ugent.be`

12. **Dispersed Turbulent Two Phase Flows**
Sommerfeld, M.
Martin-Luther University, Germany.
Tel: +49 346 146 2879
Fax: +49 346 146 2878
`martin.sommerfeld@iw.uni-halle.de`

14. **Stably Stratified and Rotating Flows**
Redondo, J.M.
UPC, Spain.
Tel: +34 934 017 984
Fax: +34 934 016 090
`redondo@fa.upc.edu`

15. **Turbulence Modelling**
Jakirlic, S.
Darmstadt University of Technology, Germany.
Tel: +49 615 116 3554
Fax: +49 615 116 4754
`s.jakirlic@sla.tu-darmstadt.de`

20. **Drag Reduction and Flow Control**
Choi, K-S.
University of Nottingham, England.
Tel: +44 115 951 3792
Fax: +44 115 951 3800
`kwing-so.choi@nottingham.ac.uk`

24. **Variable Density Turbulent Flows**
Anselmet, F.
IMST, France.
Tel: +33 491 505 439
Fax: +33 491 081 637
`anselmet@irphe.univ-mrs.fr`

28. **Reactive Flows**
Roekaerts, D.
Delft University of Technology, The Netherlands.
Tel: +31 152 782 470
`D.J.E.M.Roekaerts@tudelft.nl`

32. **Particle Image Velocimetry**
Stanislas, M.
Ecole Centrale de Lille, France.
Tel: +33 320 337 170
Fax: +33 320 337 169
`Michel.Stanislas@ec-lille.fr`

33. **Transition Mechanisms, Prediction and Control**
Hanifi, A.
FOI, Sweden.
Tel: +46 855 503 197
Fax: +46 855 503 397
`ardeshir.hanifi@foi.se`

34. **Design Optimisation**
Giannakoglou, K.
NTUA, Greece.
Tel: +30 210 772 1636
Fax: +30 210 772 3789
`kgianna@central.ntua.gr`

35. **Multipoint Turbulence Structure and Modelling**
Cambon, C.
ECL Ecully, France.
Tel: +33 472 186 161
Fax: +33 478 647 145
`claude.cambon@ec-lyon.fr`

36. **Swirling Flows**
Braza, M.
IMFT, France.
Tel: +33 534 322 839
Fax: +33 534 322 992
`braza@imft.fr`

37. **Bio-Fluid Mechanics**
Poelma, C.
Delft University of Technology, Holland.
Tel: +31 152 782 620
Fax: +31 152 782 947
`c.poelma@tudelft.nl`

38. **Micro-thermofluidics**
Borhani, N.
EPFL, Switzerland.
Tel: +41 216 933 503
Fax: +41 216 935 960
`navid.borhani@epfl.ch`

39. **Aeroacoustics**
Bailly, C.
Ecole Centrale de Lyon, France.
Tel: +33 472 186 014
Fax: +33 472 189 143
`christophe.bailly@ec-lyon.fr`

40. **Smoothed Particle Hydrodynamics**
Le Touze, D.
Ecole Centrale de Nantes, France
Tel: +33 240 371 512
Fax: +33 240 372 523
`David.LeTouze@ec-nantes.fr`

41. **Fluid Structure Interaction**
Longatte, E.
EDF, France.
Tel: +33 130 878 087
Fax: +33 130 877 727
`elisabeth.longatte@edf.fr`

42. **Synthetic Models in Turbulence**
Nicolleau, F.
University of Sheffield, England.
Tel: +44 114 222 7867
Fax: +44 114 222 7890
`f.nicolleau@sheffield.ac.uk`

43. **Fibre Suspension Flows**
Lundell, F.
The Royal Institute of Technology, Sweden.
Tel: +46 87 906 875
`fredrik@mech.kth.se`

44. **Fundamentals and Applications of Fractal Turbulence**
Fortune, V.
Université Pierre et Marie Curie, France.
Tel: +33 549 454 044
Fax: +33 549 453 663
`veronique.fortune@lea.univ-poitiers.fr`

45. **Uncertainty Quantification in Industrial Analysis and Design**
Lucor, D.
d'Alembert Institute, France.
Tel: +33 (0) 144 275 472
`didier.lucor@upmc.fr`

ERCOFTAC Pilot Centres

Alpe - Danube - Adria
Steiner, H.
Inst. Strömungslehre and
Wärmeübertragung
TU Graz, Austria
`kristof@ara.bme.hu`

France West
Danaila, L.
CORIA, University of Rouen,
Avenue de l'Université BP12,
76801 Saint Etienne du Rouvray
France.
Tel: +33 232 953 702
`luminita.danaila@coria.fr`

Netherlands
Van Heijst, G.J.
J.M. Burgerscentrum,
National Research School for Fluid
Mechanics, Mekelweg 2,
NL-2628 CD Delft, Netherlands.
Tel: +31 15 278 1176
Fax: +31 15 278 2979
`g.j.f.vanheijst@tudelft.nl`

Belgium
Geuzaine, P.
Cenaero,
CFD Multi-physics Group,
Rue des Fréres Wright 29,
B-6041 Gosselies,
Belgium.
Tel: +32 71 919 334
`philippe.geuzaine@cenaero.be`

Germany North
Gauger, N.R.
Chair for Scientific Computing
TU Kaiserslautern
Paul-Ehrlich-Strasse 34
67663 Kaiserslautern, Germany
Tel: +49 631 205 5635
Fax: +49 631 205 3056
`nicolas.gauger@scicomp.uni-kl.de`

Nordic
Wallin, S.
Swedish Defence Research Agency FOI,
Information and Aeronautical Systems,
S-16490 Stockholm,
Sweden.
Tel: +46 8 5550 3184
Fax: +46 8 5550 3062
`stefan.wallin@foi.se`

Brasil
Rodriguez, O.
Department of Mechanical Engineering,
Sao Carlos School of Mechanical
Engineering,
Universidade de Sao Paulo,
Brasil.
`oscarmhr@sc.usp.br`

Germany South
Becker, S.
Universität Erlangen, IPAT
Cauerstr. 4
91058 Erlangen
Germany
Tel: +49 9131 85 29451
Fax: +49 9131 85 29449
`sb@ipat.uni-erlangen.de`

Poland
Rokicki, J.
Warsaw University of Technology,
Inst. of Aero. & App. Mechanics,
ul. Nowowiejska 24,
PL-00665 Warsaw, Poland.
Tel: +48 22 234 7444
Fax: +48 22 622 0901
`jack@meil.pw.edu.pl`

Czech Republic
Bodnar, T.
Institute of Thermomechanics AS CR,
5 Dolejskova,
CZ-18200 Praha 8,
Czech Republic.
Tel: +420 224 357 548
Fax: +420 224 920 677
`bodnar@marian.fsik.cvut.cz`

Greece
M. Founti.
National Tech. University Of Athens,
School of Mechanical Engineering,
Lab. of Steam Boilers and
Thermal Plants,
Heroon Polytechniou 9,
15780 Zografou, Athens, Greece
Tel: +30 210 772 3605
Fax: +30 210 772 3663
`mfou@central.ntua.gr`

France - Henri Bénard
Godeferd, F.S.
Ecole Centrale de Lyon.
Fluid Mechanics and Acoustics Lab.,
F-69134 Ecully Cedex,
France.
Tel: +33 4 72 18 6155
Fax: +33 4 78 64 7145
`fabien.godeferd@ec-lyon.fr`

Spain
Onate, E.
Universitat Politenica de Catalunya,
Theofilis, V.
Universidad Politcnica de Madrid, Spain
Spain.
`onate@cimne.upc.edu`
`vassilis@aero.upm.es`

Switzerland
Jenny, P.
ETH Zürich,
Institute of Fluid Dynamics,
Sonneggstrasse 3,
8092 Zürich, Switzerland.
Tel: +41 44 632 6987
`jenny@ifd.mavt.ethz.ch`

Portugal
da Silva, C. B.
Instituto Superior Técnico,
University of Lisbon
Av. Rovisco Pais, 1049-001 Lisboa
Portugal
`carlos.silva@ist.utl.pt`

France South
Braza, M.
IMF Toulouse,
CNRS UMR - 5502,
Allée du Prof. Camille Soula 1,
F-31400 Toulouse Cedex, France.
Tel: +33 534 322 839
Fax: +33 534 322 992
`Braza@imft.fr`

Italy
Rispoli, F.
Tel: +39 064 458 5233
`franco.rispoli@uniroma1.it`
Borello, D
Tel: +39 064 458 5263
`domenico.borello@uniroma1.it`
Sapienza University of Rome,
Via Eudossiana, 18
00184 Roma, Italy

United Kingdom
Standingford, D.
Zenotech Ltd.
University Gate East, Park Row,
Bristol, BS1 5UB
England.
Tel: +44 117 302 8251
Fax: +44 117 302 8007
`david.standingford@zenotech.com`

Best Practice Guidelines for Computational Fluid Dynamics of Dispersed Multi-Phase Flows

Editors

Martin Sommerfeld, Berend van Wachem
&
René Oliemans

The simultaneous presence of several different phases in external or internal flows such as gas, liquid and solid is found in daily life, environment and numerous industrial processes. These types of flows are termed multiphase flows, which may exist in different forms depending on the phase distribution. Examples are gas-liquid transportation, crude oil recovery, circulating fluidized beds, sediment transport in rivers, pollutant transport in the atmosphere, cloud formation, fuel injection in engines, bubble column reactors and spray driers for food processing, to name only a few. As a result of the interaction between the different phases such flows are rather complicated and very difficult to describe theoretically. For the design and optimisation of such multiphase systems a detailed understanding of the interfacial transport phenomena is essential. For single-phase flows Computational Fluid Dynamics (CFD) has already a long history and it is nowadays standard in the development of air-planes and cars using different commercially available CFD-tools.

Due to the complex physics involved in multiphase flow the application of CFD in this area is rather young. These guidelines give a survey of the different methods being used for the numerical calculation of turbulent dispersed multiphase flows. The Best Practice Guideline (BPG) on Computational Dispersed Multiphase Flows is a follow-up of the previous ERCOFTAC BPG for Industrial CFD and should be used in combination with it. The potential users are researchers and engineers involved in projects requiring CFD of (wall-bounded) turbulent dispersed multiphase flows with bubbles, drops or particles.

Table of Contents

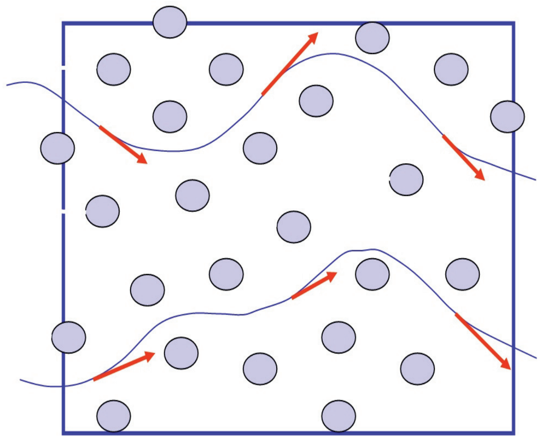

Copies of the Best Practice Guidelines can be acquired electronically from the ERCOFTAC website:

www.ercoftac.org

Or from:

ERCOFTAC (CADO)
PO Box 53877
London, SE27 7BR
United Kingdom

Tel: +44 203 602 8984
Email: magdalena.jakubczak@ercoftac.org

The price per copy (not including postage) is:

ERCOFTAC members	
First copy	*Free*
Subsequent copies	75 Euros
Students	75 Euros
Non-ERCOFTAC academics	140 Euros
Non-ERCOFTAC industrial	230 Euros
EU/Non EU postage fee	10/17 Euros